Base-Modified Post-Tensioned Rocking Walls for Tailored Seismic Response and Damage Reduction

Chi-Pu Lin

A dissertation
submitted in partial fulfillment of the
requirements for the degree of

Doctor of Philosophy

University of Washington

2022

Reading Committee:

Richard Wiebe, Chair

Jeffrey W. Berman, Chair

Paolo M. Calvi

Program Authorized to Offer Degree:
Department of Civil and Environmental Engineering

University of Washington

Abstract

Base-Modified Post-Tensioned Rocking Walls for Tailored Seismic Response and Damage Reduction

Chi-Pu Lin

Co-Chairs of the Supervisory Committee:
Richard Wiebe
Civil and Environmental Engineering

Jeffrey W. Berman
Civil and Environmental Engineering

Recent studies on the socio-economic impact of earthquakes have led to the development of several novel lateral force-resisting systems. These systems aim to improve the seismic performance and resilience of structures by reducing the residual drift and protecting the main structural components. The post-tensioned rocking wall is one of the novel systems that has shown promising results by limiting bending and shear stress on the wall via post-tensioned bars/strands and rocking. However, despite the many benefits of this system — such as redirecting the seismic energy into energy dissipation devices, and re-centering after seismic events — there remain challenges. This work introduces the concept of base-modified rocking walls (both curved and tapered base), a modification over traditional rectangular profile walls, and analytically/numerically investigates the potential benefits of this simple geometric modification.

In this work, three levels of analysis are used to characterize the base-modified wall behavior. The three levels gradually increase in system fidelity to shift from qualitative to quantitative prediction, but also necessarily from closed-form analysis to numerical simulation. At the first level, Lagrange's equations are employed in formulating the analytical equations to study the static and dynamic behavior of a simplified curved-base rocking wall

in concert with a gravity frame. The parameter sensitivities and nonlinear dynamic behaviors are identified using the analytical equations. Furthermore, the advantages of the curved-base rocking walls are explored. Alongside the analytical model, a finite element model of the rocking walls was developed to validate the analytical model and to later extend the study to more generalized rocking walls.

The second level was the extension of the analytical model to capture the behavior of flexible rocking walls. The objective was to characterize the interaction of rocking and wall deformation and by using the framework of nonlinear normal modes, an extension of linear normal modes. The study used a two degrees-of-freedom model consisting of one degree-of-freedom for the base rotation angle and a second degree-of-freedom for the wall deformation. The analytical model was able to capture the amplitude-frequency behavior of different modes, characterize the transition between fixed-base vibration and rocking, and show co-existing steady-state solutions.

Lastly, a finite element model of flexible tapered-base rocking wall systems was develop to more accurately explore the potential benefits of the geometric base modification using ground motions. Moreover, the model broadens the scope by generalizing elements that were previously simplified/omitted. To evaluate the seismic performance of the the modified wall, case studies of a two-story and ten-story wall were done. The studies showed the modified rocking walls resulted in lower base damage than the equivalent rectangular rocking wall without causing issues in (and sometimes even reducing) other demands, e.g., base shear, interstory drift, or floor acceleration.

TABLE OF CONTENTS

Page

LIST OF FIGURES

LIST OF TABLES

ACKNOWLEDGMENTS

I would like to express my utmost gratitude to my advisor, Professor Richard Wiebe, and my co-advisor, Professor Jeffrey Berman. Their advice, guidance, and support during my time at the University of Washington have made it possible for me to complete my Ph.D. work. They have been inspirational, encouraging, thoughtful, and patient from the first day until the last. It has been a pleasure working with them and to have had them as my advisors.

I would like to thank Sarah Wichman especially for her help with the project on rocking walls. Her numerical and experimental work on rocking walls has been incredibly helpful. I would also like to thank my friends and colleagues throughout my time at the university for teaching me and learning alongside me. Just to name a few, I would like to thank Leikune Aragaw, Clare Terpstra, Andrew Yang, Han-Gyu, and Kamal Ahmed.

This researched was partly funded by the Paul B. Liao Fellowship. The experiences I have had and the knowledge I have learned at the university would not have been possible without the amazing generosity of Dr. and Mrs. Liao. Again, thank you again for your contributions.

DEDICATION

To my wife, *Meng Wang*

who inspires me and gives me immeasurable love, support, and passion for life.

To my parents, *Huei-Mei* and *Jung-Ting*

who raised me and provided me lifetimes worth of love and support.

To my brother and sisters, *Tim*, *Diana*, and *Susana*

who have always been there for me.

Chapter 1
INTRODUCTION

1.1 Motivation

1.1.1 Overview of lateral systems

Lateral Force-Resisting Systems (LFRSs) are vital to structures in seismically active regions. There are numerous types of LFRSs, with some of the most prominent types being braced frames, moment-resisting frames, and shear walls. Lateral force-resisting systems can reduce interstory and roof drift by being laterally stiff, however, being very stiff can increase bending and shear stress demand on the LFRS itself. As traditional LFRSs are simply to resist lateral force, they are not designed to self-center, and therefore would lead to residual drift after seismic events. Additionally, very stiff LFRSs may lead to rapid story accelerations that could be critical to non-structural elements.

More recent advanced LFRSs are developed to address these issues such that (1) stress demand on the LFRS are limited, (2) the structure can self-center, and (3) the static and dynamic behavior can be tailored such that the acceleration demands are controlled. An example is seismic isolation system, which can limit earthquake damage to both structural and non-structural elements by decoupling the superstructure from the ground and thus reducing both interstory drift and force demand of the superstructure. Classical examples of a seismic isolation system are rubber bearing and friction pendulum bearing isolators. They are generally costly and thus not a viable solution in all applications.

Similar to friction pendulum bearing isolators, rocking isolators, such as free-standing columns/walls, act as an inverted pendulum structure. Housner first studied this phenomenon after he observed tall and slender structures able to rock remained upright in contrast to severe damages in more stable-appearing structures. Many research on rocking

isolators have been done since then. On the other hand, Post-Tensioned (PT) rocking walls act as both an LFRS and a seismic isolator. The former is achieved by the initial lateral stiffness before the base of the wall uplifts (i.e., decompresses), the latter is achieved after the base uplifts, at which point the lateral stiffness decreases, akin to friction pendulum isolators when the static friction is overcome. Although the post-decompression stiffness is reduced, the post-tensioning elements (e.g., steel bars or strands) result in a positive post-decompression lateral stiffness and increase the lateral force needed to reach decompression. Free-standing (i.e., non-PT) walls, on the contrary, exhibit negative stiffness after the base uplifts.

Figure 1.1 shows an archetypal PT rocking wall configuration composed of: a free-standing wall, e.g., a Cross-Laminated Timber (CLT) panel; post-tensioned steel strands/bars; an energy dissipation system, in this case, U-Shaped Flexural Plates (UFPs); and wall-to-diaphragm connections to transfer the inertial forces from the gravity system to the rocking wall. In addition to contributing to the post-decompression lateral stiffness, the post-tensioning elements re-centers the wall after the seismic event and the energy dissipation device dampens the system through inelastic deformation [Baird et al., 2014]. The components resolve to a cyclic 'flag-shaped' hysteresis as shown schematically in Fig. 1.2. Lateral force-resisting systems with flag-shaped hysteresis can improve a building's resilience due to the re-centering and energy dissipating properties. Moreover, the uplift (i.e., rocking) mechanism acts as a fuse to limit the internal shear force and bending moment demands on the wall. Ultimately, the objective is that the primary structure remains undamaged and re-centered after an earthquake, and that the energy dissipation devices be easily and quickly replaced after moderate to extreme seismic events, vastly increasing the seismic resilience compared to conventional design performance objectives.

1.1.2 Impetus for base-modified rocking walls

Post-tensioned rocking walls have shown promising results, as will be shown later, but have also shown some remaining challenges: (i) base damage due to stress concentration from

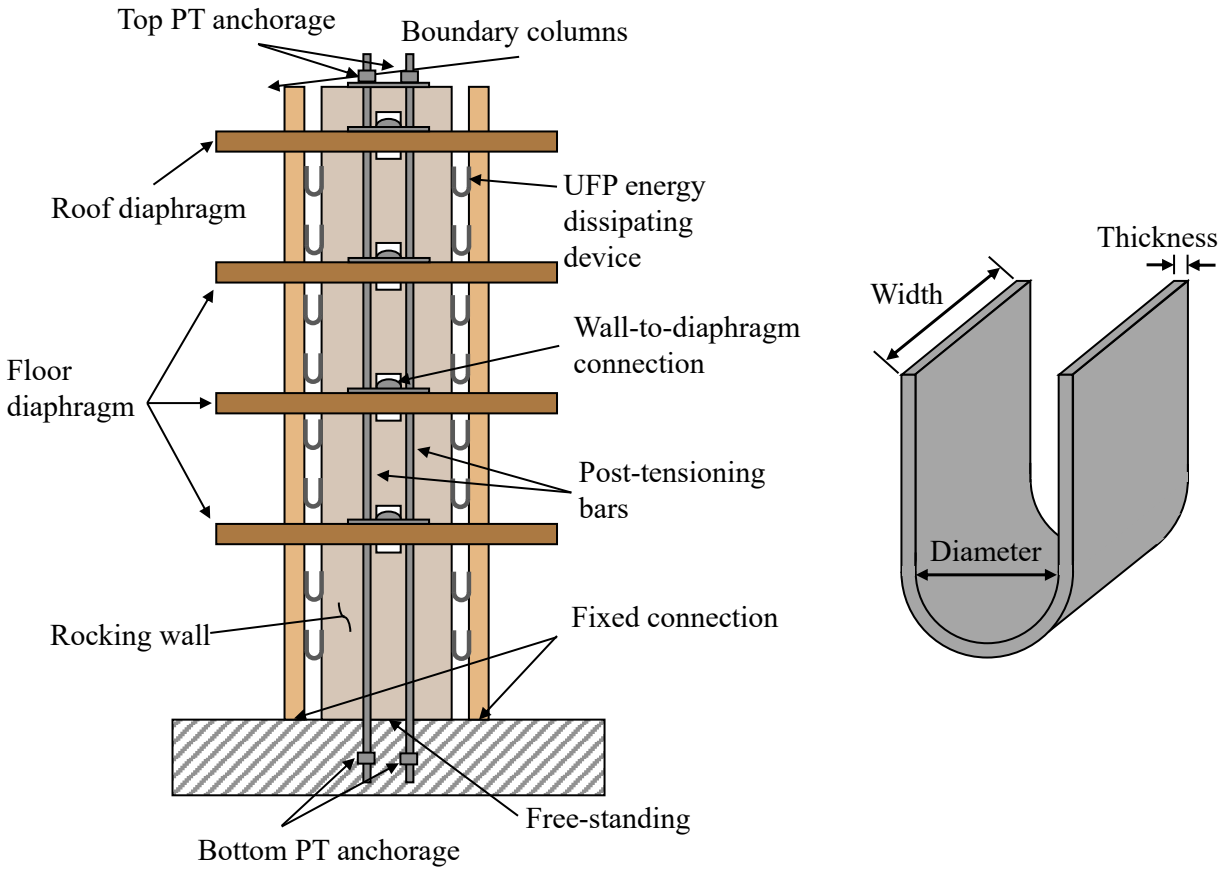

Figure 1.1: Diagram of PT rocking wall (left), UFP (right).

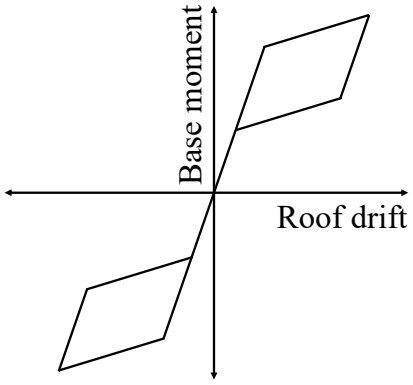

Figure 1.2: Cyclic flag-shaped hysteresis.

rocking [Henry et al., 2012]; and (ii) yielding/fracturing the PT bars which may lead to collapse, large deformations, and/or residual deformation. Modifying the geometry of the base (curved or tapered) — see Fig. 1.3 — could address these challenges, and also improve the seismic performance and resilience of rocking structures as follows:

1. The stress concentration on the corner of the wall is reduced, and therefore base damage can be controlled. In the case of a tapered base, the damage would be distributed between the interior and exterior corners.
2. The geometry of the base also allows the wall to drift further before the post-tensioning elements start to yield due to the decrease in height as the wall transitions from the interior to exterior corners.
3. The modified base gives engineers more parameters to tune the static and unforced dynamics behavior, usually shown with pushover and amplitude-frequency plots. The behavior can be tailored to achieve seismic isolation and control drift at different seismic hazard levels.
4. The base-ground impact force is reduced by the decrease of the effective width of the base (i.e., flat surface region of the base), see Fig. 1.3. Impact can be prevented if the base is entirely curved, although this comes with a loss in stiffness and restoring force.
5. The geometry allows further confinement for the material at the interior corner, which may be especially important for reinforced concrete.

1.2 Organization

The overarching goal of this dissertation is to evaluate the potential benefits (and challenges) of BMRWs for earthquake engineering, and to further explore the fundamental behavior of PT rocking walls. Three objectives were set to achieve this goal. The following three chapters are organized to address these objectives in the same order. Finally, a conclusion is given in the final chapter.

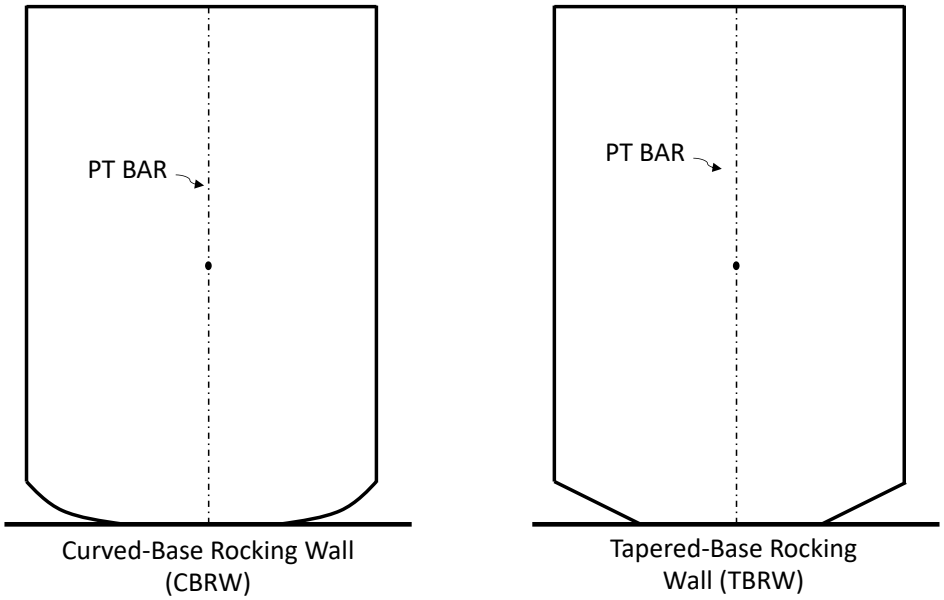

Figure 1.3: Base-modified rocking walls.

1.2.1 Objective 1: Isolate the effects of the base modification on a PT rocking wall

The first objective is to understand the effects of the modified base on the static and dynamic response (see items 2 and 3 in Section 1.1.2). To achieve this objective, the study looked at a rigid PT curved-base rocking wall with a gravity frame that delivers the inertial forces. A semi-analytical model is developed using the Lagrangian equation and solved numerically to simulate the static and dynamic response.

1.2.2 Objective 2: Explore the interaction of the rocking and wall deformations

The second objective looks at flexible rectangular rocking walls and the unforced dynamic response. The dynamics of fixed-base flexible walls and rocking rigid blocks are well understood, yet there is a knowledge gap in the transition between fixed-base vibration and rocking, and their couplings effects. Essentially, the objective hopes to provide the flexible rocking wall equivalent of natural frequency, which, in addition to the static pushover, is a standard design parameter for all seismic design. To isolate the effects of the lateral stiffness

of the wall on the transition, the study consisted of a *rectangular* PT wall and a rigid base assumption. The semi-analytical model is developed using a Lagrangian approach specific to systems of lumped masses [Wiebe and Harvey, 2019] and solved numerically. Furthermore, the unforced dynamic response is explored using the Nonlinear Normal Mode (NNM) framework. The NNM tool is typically utilized by mechanical and aerospace engineers, thus this objective also hopes to give an example of NNM to the field of structural engineering in hope of wider adoption (as was the objective in [Kerschen et al., 2009]).

1.2.3 Objective 3: Evaluate the base damage reduction and seismic performance of tapered-base rocking walls

The third objective is to evaluate the BMRWs' ability to decrease base damage and their overall seismic performance (see items 1 to 3 in Section 1.1.2) using two case studies: a two-story and a ten-story PT rocking wall. This objective combines objectives 1: modified base, and 2: flexible wall. A finite element model is used to fully expand the scope of the previous two objectives (i.e., includes base damage models, UFPs, and dynamic response under ground motions). Due to the complexity of the model and simulations, the third objective opted for tapered-base walls instead of curved-base walls. Revisiting this objective via a comprehensive parametric study of curved-base rocking walls is a good opportunity for a follow up future study.

1.3 Background

The literature review is separated into three subsections, aligning with the previous three objectives. The first subsection is on free-standing rigid blocks, which largely aligns with the first objective. Studies on free-standing rigid blocks provided insight into the fundamental behavior of the rocking mechanics and led to further understanding into their seismic isolation capabilities. The second subsection is on flexible rocking bodies and NNMs, which, as the name suggests, is the nonlinear equivalence of linear normal modes that are typically solved through eigen-analysis and (unlike NNMs) have one constant natural frequency for each

normal mode. As rocking is highly nonlinear, NNMs provide an appropriate framework to study the resonant frequencies of rocking systems and can lead to further understanding to the dynamic response. The third subsection is on PT rocking systems which focuses more on the overall system response as it relates to earthquake engineering.

1.3.1 Review of free-standing rigid rocking structures

Housner observed that tall slender structures which were allowed to rock remained upright after the 1960 Chilean earthquake, as opposed to ones that were fully fixed to the ground [Housner, 1963]. In this seminal work, he introduced an approach to find the kinetic energy dissipated from base-ground impact using the conservation of angular momentum for a single-joint rocking (rigid) block and applied the equation of motion to develop the Simple Rocking Model (SRM). The equation of motion and the reduction in kinetic energy during impact, r, is respectively given in Eqs. (1.1) and (1.2), where I_o, θ, W, R, α, and m are the moment of inertia about the center of rotation, rotation angle, weight, radial distance from the center of rotation to the center of gravity, the angle between R and the vertical (at rest), and mass, respectively (see Fig. 1.4).

$$I_o \frac{d^2\theta}{dt^2} = -WR\sin(\alpha - \theta) \tag{1.1}$$

$$r = \left(\frac{\dot{\theta}_2}{\dot{\theta}_1}\right)^2 = \left[1 - \frac{mR^2}{I_o}(1 - \cos 2\alpha)\right]^2 \tag{1.2}$$

The right hand side of Eq. (1.1) is the negative of the restoring force when rotated through angle θ.

The SRM has since been used and extended by many researchers in the 20th century as shown in the following. Yim et al. looked at rocking response of rigid blocks subject to ground motions by solving the nonlinear equations of motions numerically and found that the response is sensitive to details of the ground motion, the size, and the slenderness ratio of the block [Yim et al., 1980]. They concluded that probabilistic estimates of the ground motion intensity may be obtained from its effects on rocking rigid blocks, such as

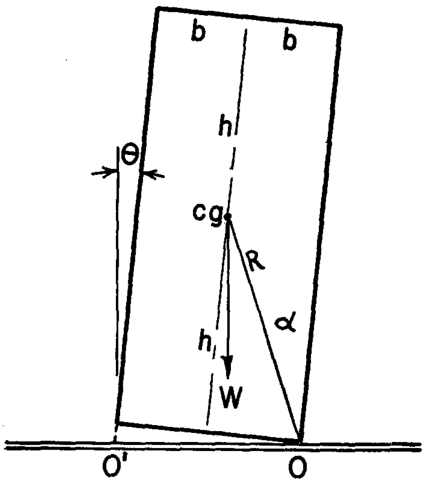

Figure 1.4: A rocking block [Housner, 1963].

monuments and tombstones. Similarly, rigid rocking blocks on a rigid foundation subjected to horizontal and vertical ground motions were studied by Ishiyama by numerically solving the equations of motion [Ishiyama, 1982]. Ishiyama found that the coefficient of friction must be greater than the breadth-height-ratio for rocking to occur, and, to evaluate overturning, both the horizontal acceleration and the velocity of the floor must be taken into account. Spanos and Koh looked at rigid blocks rocking due to harmonic [Spanos and Koh, 1984] and random shaking [Spanos and Koh, 1986]. Two approximate methods were developed by Koh et al. to predict the rocking amplitude and maximum tilt-angle of a rigid block on a flexible foundation under horizontal motion [Koh et al., 1986]. Results show reasonable agreement between the predictions and numerical integration. A study on rigid rocking blocks subjected to sinusoidal base motion was done by Tso and Wong, and observed that the steady state response solutions (harmonic and sub-harmonic) can be either out-of-phase and in-phase with respect to the sinusoidal excitation [Tso and Wong, 1989a]. They also conducted tests and found that the two common types of steady state response are harmonic and 1/3 sub-harmonic response and that the theoretical predictions of the amplitudes was in good agreement with the experimental results [Wong and Tso, 1989]. Base isolation

properties of 3D rocking and uplift of a rigid cylinder have been shown using Lagrangian formulation to develop the equation of motion [Koh and Hsiung, 1991].

Furthermore, work on rigid rocking blocks has continued in the 21st century as shown in the following. Makris and Zhang conducted a study on the behavior and effect of restrainers on the stability of rocking rigid bodies under certain ground excitations, and found restrainers to be more efficient at preventing small slender block overturn at low frequency pulses [Makris and Zhang, 2001]. Taniguchi investigated the seismic response of rigid block on rigid foundations subjected to horizontal and vertical ground motions and found the response is sensitive to the coefficient of friction and slenderness, and the wave properties and intensity of ground motions [Taniguchi, 2002]. Moreover, long period earthquakes tend to lead to overturning. The response of a rigid rocking structure to 20 recorded accelerograms was studied by Sorrentino et al. to understand the appropriate parameters when assessing overturn and seismic risk [Sorrentino et al., 2006]. They found peak ground velocity to be more effective than peak ground acceleration at evaluating the effects of amplitude and frequency on rigid bodies. DeJong and Dimitrakopoulos proposed a methodology to derive the equivalence between single rocking blocks and other rocking mechanisms (e.g., multiple rocking blocks) by local linearization of the equations of motion [DeJong and Dimitrakopoulos, 2014]. A few of these works on rocking blocks have provided insight into the response through closed-form equations, but they are limited to free vibration and pulse loading due to the complex nonlinear behavior of rocking systems.

Numerical studies have shown rocking systems are extremely sensitive to system parameters and initial conditions [Aslam et al., 1980; Hogan, 1989; Plaut et al., 1996; Ageno and Sinopoli, 2005; Lenci and Rega, 2006], although typically for harmonic loading scenarios. Due to the sensitivity to initial conditions, it is important to accurately predict rocking initiation (i.e., when the rocking starts) in order to better simulate the dynamic response. However, it is unlikely to affect the statistical results, for example, using a set of ground motions, the median of the maximum observed base shear under each ground motion is unlikely to significantly change.

Especially relevant to the first objective, Bachmann et al. [Bachmann et al., 2016] looked at rigid columns with curved bases of constant curvature, however, without post-tensioning, and showed the curved wedges added to the flat base improved its overturning stability without significantly increasing the base moment, i.e., using the wedges, the columns were less likely to topple over without having to reduce the probability of rocking. They derived the equations of motion and validated them with free-vibration tests, which showed the response of the block is extremely sensitive to impact damping r.

1.3.2 Nonlinear normal modes

The second objective aims to provide a better understanding of the fundamental behavior of flexible PT rocking structures, primarily the interaction between vibration of the wall and rocking action, and the transition from fix-base vibration to rocking. There have been several studies on the dynamics of flexible rocking blocks. Acikgoz and DeJong have conducted several analytical and experimental studies on *flexible* rocking structures and found accurate impact damping is important for predicting the dynamic response [Acikgoz and DeJong, 2016]. Furthermore, they proposed a new modal equation and found the vibration frequencies, shapes, and excitation mechanism changes once rocking initiates [Acikgoz and DeJong, 2017]. Studies on flexible rocking structures have also been conducted in [Thiers-Moggia and Málaga-Chuquitaype, 2020; Manzo and Vassiliou, 2020] by using rocking oscillator models (single-degree-of-freedom linear oscillators commonly used in structural dynamics but with base uplift). Static loading response of elastic and inelastic rocking bodies were investigated in [Avgenakis and Psycharis, 2017] and [Avgenakis and Psycharis, 2020], respectively. In addition, the flexible rocking phenomenon has also been studied using a finite element model that consists of a nonlinear elastic rotation spring, a viscous damper, and a Euler-Bernoulli beam-column, see [Vassiliou et al., 2014].

Again, the second objective is approached under the concept of NNMs. Recent decades have seen extensive exploration of NNMs [Kerschen et al., 2009], particularly in the study of mechanical vibrations. Nonlinear normal modes, as much as possible, extend the concepts

of linear modal analysis to nonlinear systems. Initial research on NNMs looked at nonlinear oscillations for which all degrees-of-freedom reach their maximum, minimum, and zero values simultaneously (i.e., synchronous motion), which is an immediate extension of linear normal modes. This definition has since been extended by Kerschen et al. [Kerschen et al., 2009] to 'a non-necessarily synchronous periodic motion of the underlying conservative system' (i.e., the NNMs are comparable to undamped natural frequencies) in order to account for the cases where some coordinates vibrate at higher (usually integer multiple) frequencies than others. The fact that some coordinates vibrate at higher frequencies is an implicitly nonlinear phenomenon that results from interactions (energy transfer) between different modes, which does not occur in linear systems. In other words, a system forced at or near its first NNM frequency, may transfer energy to other NNMs.

Nonlinear normal modes was first investigated in the 1960s by Rosenberg [Rosenberg, 1960, 1962, 1966] by examining systems with n masses interconnected by nonlinear springs with n-degrees-of-freedom and showed finding the normal modes is reduced to a geometrical maximum-minimum problem. It was later studied by Rand [Rand, 1971a,b, 1974] and Manevitch and Mikhlin [Manevich and Mikhlin, 1972] in the 1970s. Rand presented a method for finding NNMs in certain holonomic, scleronomous, conservative nonlinear two-degree-of-freedom systems that does not explicitly involve the differential equations of motion [Rand, 1974]. Manevich and Mikhlin examined periodic solution of nonlinear systems that are similar to normal vibrations with rectilinear trajectories [Manevich and Mikhlin, 1972].

A great effort on NNMs was later done by Vakakis et al. and Shaw and Pierre. Vakakis et al. studied free oscillations of two-degree-of-freedom nonlinear undamped systems, specifically on bifurcations of normal modes [Caughey et al., 1990], and free oscillations of a nonlinear discrete oscillator using the NNMs framework and solved using the Mikhlin-Manevich asymptotic method with derivations of analytical expressions [Vakakis, 1992], and NNMs of one-dimensional, conservative, continious systems using conservation of energy to derive the partial differential equations and asymptotically solved them with the perturbation methodology [King and Vakakis, 1994]. Shaw and Pierre developed a method for weakly nonlinear

systems that provides the nonlinear coordinate transformation which relates the original systems coordinates to the modal coordinates [Shaw and Pierre, 1993]. The transformation can be used obtain the overall motion from the nonlinear modal dynamics with approximate nonlinear version of superposition. They also developed a methodology for normal nodes of motion for nonlinear systems and discussed the general theory for application of vibrations of continuous media; examples were presented to illustrate the approach, such as a simply supported beam on a nonlinear elastic foundation [Shaw and Pierre, 1994].

More recently, Hill, et al. investigated the dynamic behavior of a nonlinear system and how it can lead to numerous NNM branches with two distinct classes: phase-locked and phase-unlocked [Hill et al., 2017]. It was found that energy transfer in phase-locked NNMs are done via fundamental components of the modes whereas energy transfer in phase-unlocked NNMs can only be done via harmonics. Also, using physics-integrated deep learning to develop a new data-driven framework, Li and Yang obtained the nonlinear modal identification by integrating a unique dynamic-coder using physics-based constraints. The identification results were consistent with theoretically derived or numerically computed results from closed-form equations [Li and Yang, 2021].

Comprehensive review articles on the advancement of NNMs and their typical applications over the past several decades can be found in [Vakakis, 1997; Pierre et al., 2006]. More recently, a review of the theoretical developments and the application of NNMs are provided in [Mikhlin and Avramov, 2011] and [Avramov and Mikhlin, 2013], respectively. Additional information on NNMs (e.g., internally resonant NNMs, mode bifurcations and stability, analytical and numerical techniques, reduced-order modeling, and localization phenomena) can be found in [Kerschen et al., 2009].

1.3.3 Review of post-tensioned rocking systems

Though there is a rich history of research on the fundamental dynamics of rocking blocks, within earthquake engineering applications, the focus has instead been placed on PT rocking systems in concert with energy dissipation devices to reduced the likelihood of toppling,

increase lateral resistance, and reduce residual lateral displacement. The combination of rocking, post-tensioning elements, and energy dissipation devices results in a 'flag-shaped' hysteresis curve [Christopoulos et al., 2002a,c; Restrepo and Rahman, 2007; Ganey, 2015; Akbas et al., 2017] that provides re-centering (i.e., self-centering) and limits peak drifts. Studies on PT rocking structures coupled with energy dissipation devices have been conducted and demonstrated robust seismic performance.

Post-tensioned rocking connections in precast concrete buildings first started in the 1990's under the Precast Seismic Structural Systems (PRESSS) program [Priestley, 1991; Kurama et al., 1999], which included a test of a large-scale five-story structure, and now have design and detailing requirements in ACI 318-14. The study was the first to use unbonded PT steel to increase the lateral load and displacement capacities, reduced the demands in the precast members, and provided self-centering capabilities. The following are experimental studies that came after the PRESSS program on rocking concrete systems. Holden et al. tested half-scale precast concrete walls with PT carbon fiber tendons and steel fiber reinforced concrete under quasi-static reversed cyclic lateral loading, which were able to achieve drift levels surpassing 3% [Holden et al., 2003]. Half-scale PT rocking precast walls with longitudinal mild steel reinforcement as energy dissipators were conducted in [Restrepo and Rahman, 2007] which showed the 'flag-shape' hysteretic response with an equivalent viscous damping ratio of 14%. Experimental tests to investigate the dynamic response of PT precast concrete walls were conducted [Twigden et al., 2012]. The coefficient of restitution was obtained from free vibration decay and was in good agreement with calculations with Housner's formulation. Post-tensioned precast concrete walls were experimentally and analytically investigated by Perez et al. [Perez et al., 2003]. The test results showed the walls can undergo significant nonlinear lateral displacement without significant damage while still able to self-center. Note that there was no energy dissipation device and thus the cyclic lateral load behavior was mostly nonlinear elastic. More recently, an experimental and numerical study on a precast PT concrete wall with yielding and friction energy dissipation and observed that both the energy dissipation components worked as designed, with a significant enhancement in energy

dissipation when combined [Li et al., 2020].

In addition to experimental investigations, analytical and numerical work on PT concrete systems has been done in the following: Kurama et al. analytically investigated the seismic behavior and design of unbonded PT precast concrete walls and showed the walls can undergo large nonlinear lateral displacement with minimal damage; the walls also undergo larger displacement but smaller residual displacement during an earthquake compared to cast-in-place walls [Kurama et al., 1999]. Nonlinear dynamic time history analyses of a precast wall system that used mild steel reinforcement for energy dissipation, in addition to PT steel, saw considerably less lateral displacement under ground motions, especially for shorter period vibration [Kurama, 2002]. Wiebe and Christopoulos examined the use of multiple rocking joints to reduce higher mode effects in base-rocking systems [Wiebe and Christopoulos, 2009] showed, under ground motions, the bending moment envelope of the wall is considerably reduced by using multiple rocking sections. An analytical study on overturning of viscously damped rocking structures under pulse-type excitation was done in [Dimitrakopoulos and DeJong, 2012] which showed bilateral and unilateral linear viscous dampers provide similar resistance to overturning, while nonlinear damping did not provided much less resistance. Hassanli et al. developed an analytical procedure based on geometric compatibility conditions to predict the lateral force behavior of unbonded PT concrete walls [Hassanli et al., 2016].

Rocking with PT elements has also been investigated in steel structures. Lin et al. conducted an experimental study of a 0.6-scale 2-bay 4-story PT rocking connection steel moment-resisting frame under maximum considered earthquake ground motions [Lin et al., 2013]. The results showed the frame did not collapse under the maximum considered earthquake ground motions. In addition to PT rocking steel connections, PT rocking steel-braced frames with energy dissipation devices were investigated in [Eatherton et al., 2014a]. They compared this system with other conventional and self-centering systems, formulated equations to predict the load-deformation response, looked at desired sequence of limit states, and developed general design methods for controlling the limit states.

Research on PT rocking systems has largely relied on finite element modeling, however,

the equations of motion for rocking frames have been formulated using the Lagrange equation [Dimitrakopoulos and Giouvanidis, 2015]. Furthermore, studies have shown the contact stiffness between the rocking structure and the contact surface has an effect on the overall static and dynamic behavior of the system [Alexander et al., 2011; Bachmann et al., 2017; Kibriya et al., 2018; Kashani et al., 2018].

When combining dissipators with rocking systems, the design of the post-tensioning requires the restoring force to overcome the residual forces from the dissipators to provide complete re-centering. While not the only energy dissipation option, UFPs are suitable for several scenarios. They can be connected on coupled rocking walls as was done in a recent two-story test, see [Pei et al., 2019]. Alternatively, as shown in Fig. 1.1, they can be placed between a rocking wall and adjacent columns. The mechanics of UFPs are also well-known. Kelly et al. derived the plastic force [Kelly et al., 1972] shown in Eq. (1.3). Using strain energy methods, the equation for the initial stiffness of the UFP was derived by Baird et al. [Baird et al., 2014], see Eq. (1.4). In these expressions $f_{y,u}$, b_u, t_u, D_u, and E_u are the yield stress, width, plate thickness, diameter, and modulus of elasticity of the UFP.

$$F_{p,u} = \frac{f_{y,u} b_u {t_u}^2}{2D_u} \tag{1.3}$$

$$k_{o,u} = \frac{16 E_u b_u}{27\pi} \left(\frac{t_u}{D_u} \right)^3 \tag{1.4}$$

Although the base modifications and rocking mechanics that this dissertation focuses on is material agnostic (i.e., applicable to steel, concrete, and timber), the studies in Chapter 3 and 4 use timber, and namely, data from NHERI Tall Wood project. The NHERI Tall Wood project is a collaborative effort that recently conducted a large-scale shake table test of a timber structure with CLT walls to develop and validate a resilience-based seismic design methodology for tall wood buildings [Pei et al., 2019]. Several numerical studies followed: Wichman et al. predicted the response of the two-story shake table test with a numerical model by including a flexible foundation to simulate the foundation beam used in

the experiment [Wichman et al., 2022]. Note that the same numerical model methodology is employed in the studies in this dissertation. In addition, Pei et al. [Pei et al., 2020] and Hasani et al. [Hasani et al., In press] also used numerical models to predict the response of the two-story tests. The former used a simplified method that was able to reasonably capture the global response. The latter focused on structure acceleration response for nonstructural elements.

Other studies on timber rocking walls using CLT and Laminated Veneer Lumber (LVL) have been conducted. Sarti et al. investigated the experimental behavior of large-scale PT timber walls with a focus on connection detailing and optimization of anchorage, attachment of the dissipation devices, and shear keys [Sarti et al., 2016]. Results showed that the PT timber wall system provided a high level of dissipation while showing minimal damage to the wall elements, as well as minimal residual displacements. A study on the lateral load response of PT CLT walls where two types of analytical models were used to predict the reaction was conducted by Akbas et al. [Akbas et al., 2017]. A comparison of both analytical and numerical models showed both provided accurate estimates of the lateral load response undergoing cyclic loading. Moroder et al. tested PT timber core walls and observed that the wall panels can be assumed to be rigidly connected together under serviceability level state loads, and PT force prevented the panels from sliding against the foundation [Moroder et al., 2018]. Wilson et al. developed and assessed a high-order model and a reduced-order model for PT CLT rocking walls and found, after a study consisting of 20 wall configurations of varying lengths and initial PT forces, the reduced-order model to be more computationally efficient [Wilson et al., 2019].

The cyclic response of PT CLT wall was explored and structural limit states were defined by Akbas et al. [Akbas et al., 2017] and Ganey et al. [Ganey, 2015]. They observed the flag shape hysteresis, mentioned before, and proposed the limit states design to occur in the following order: (1) decompression; (2) UFP yielding; (3) base yielding; (4) base splitting; (5) base crushing; and (6) PT yielding. Limit states (3) to (5) are based on the wall material, specifically the compression stress-strain relationship (including damage).

After yielding, the CLT stress-strain relationship can be approximated with a zero strain-hardening until it splits, at which the strength degrades down and then crushes. Barbosa et al. tested CLT under compression and found that crushing occurs when strength degrades down to approximately 25 percent of the yield stress [Barbosa et al., 2018]. Local splitting or crushing at the base leads to global strength degradation. Ganey performed pushover tests on PT CLT walls and observed damage in the CLT panels led to loss of PT force [Ganey, 2015]. Concrete structures are also at risk of base damage. Henry et al. experimentally and analytically investigated base damage, i.e., toe crushing, on PT concrete walls and found a strain of 0.005 is recommended for defining the nominal flexural strength of PT concrete walls [Henry et al., 2012].

Chapter 2

ANALYTICAL STUDY OF RIGID CURVED-BASE ROCKING WALLS

Note: Part of this chapter is a reproduction of [Lin et al., 2019]

The main goal of this chapter is to understand the effects of a curved base on the static and dynamic behavior using equations derived via the Lagrange equation. The purpose of the curved base modification explored in this chapter is to further tailor the pushover response and increase the drift at which the post-tensioning element yields. To investigate the effects of the curved base, a rigid wall was employed to isolate the effects. As such, an investigation into the base damage reduction from the base modification is shown later in Chapter 4.

This chapter first reintroduces the concept of curved-base rocking walls, details the assumptions used in the analytical model, and shows the derivations of the kinematic equations. Then it discusses the formulation of the equations of motion, development of the finite element model, and comparison of the static/dynamic response of the two models. Finally, a curved-base rocking wall is compared against a rectangular wall to explore the increase in post-tensioning element yield drift capacity, and the tailorability of the pushover curve; the amplitude-frequency relationship of a curved-base rocking wall is also discussed.

2.1 Chapter introduction

2.1.1 Motivation

Research in the past several decades on earthquakes and their associated socio-economic impacts [Todd et al., 1994; Villaverde, 1997; Filiatrault et al., 2001; Ferner et al., 2014; Welch, 2016] has motivated efforts toward the development of lateral resistance systems to

reduce structural and non-structural damage, and to improve resilience (i.e. the ability to return to service quickly and with minimal repair after an extreme event). This work has resulted in many innovative technical solutions that achieve high performance, such as base isolation, floor isolation, buckling restrained braces, special detailing for ductility, among many others.

Another example, and the focus of this work, is offered by Post-Tensioned (PT) rocking walls as illustrated in Fig. 2.1, which have gained significant attention in the past three decades. These systems achieve high performance by: (1) using rocking to increase the flexibility of the structure and reduce damage due to inelastic deformation; (2) using PT steel bars/cables to provide lateral resistance and self-centering forces that return the structure to its original undeformed configuration after unloading; and (3) applying easily replaceable energy dissipation devices — e.g. U-shaped Flexural Plate (UFP) elements [Kelly et al., 1972; Baird et al., 2014; Ganey, 2015] or tension-compression yield (TCY) elements [Kurama, 2002; Kramer et al., 2016] — to help absorb the energy from the earthquake via material yielding.

The work herein is directed at further improving the performance of rocking wall systems by exploring the use of curved-base walls to reduce damage at the rocking interface and increase the drift at which PT yielding occurs. Curved bases are most immediately applicable in the context of timber construction (with possible extensions to concrete walls and PT connections in steel and concrete frames). Rocking timber, together with tall timber, have recently become a topic of great interest. For example, the collaborative NHERI Tall Wood project recently conducted a large-scale shake table test of a timber structure with rocking Cross-Laminated Timber (CLT) walls as part of a multi-phase project with the goal to develop and validate a resilience-based seismic design methodology for tall wood buildings [Pei et al., 2019], see Fig. 2.1(a). For a more in-depth literature review on free-standing rigid rocking blocks and PT walls, see Sections 1.3.1 and 1.3.3, respectively.

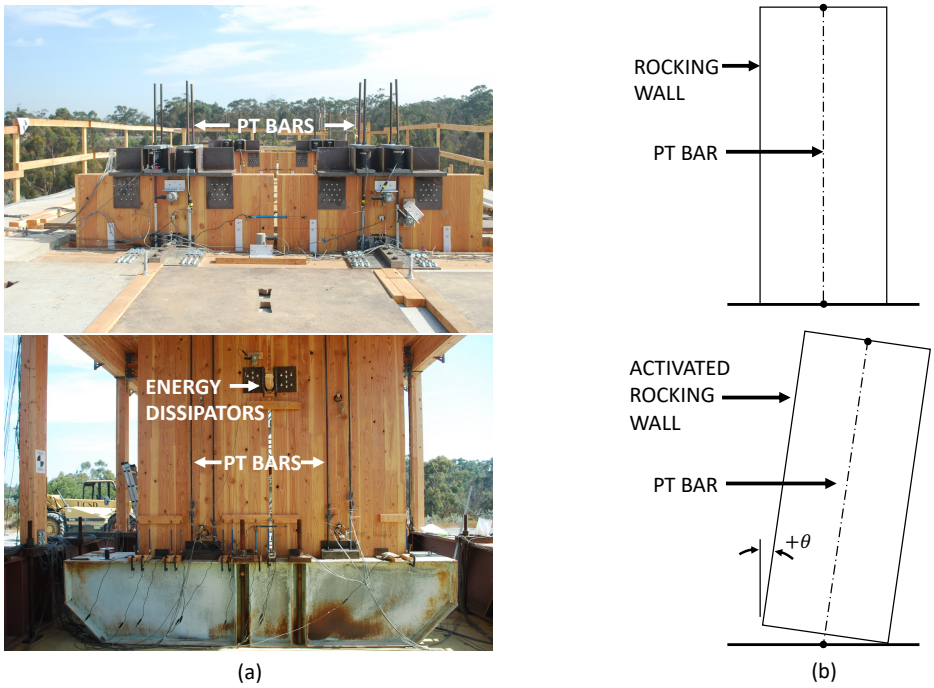

Figure 2.1: Post-tensioned rocking wall: (a) A real structure with eccentric PT bars [Wichman, 2018]; (b) alternative schematic with concentric PT bar.

2.1.2 Impetus for curved-base rocking walls

Despite the many advantages of PT rocking walls, they have a few key drawbacks: (1) damage due to stress concentration when rocking on the corners, and/or due to base-ground impact; and (2) yielding and/or fracture of the PT bars that may lead to col- lapse, large deformations, and/or residual deformation. This chapter reintroduces the concept of a Curved-Base Rocking Wall (CBRW) — see Fig. 2.2 — which may mitigate these issues, and improve control over seismic performance and resilience of rocking wall structures. The following section introduces the CBRW, after that the kinematics are discussed, followed by the formulation of the governing equations, and a discussion of several preliminary observations regarding their static and dynamic behavior.

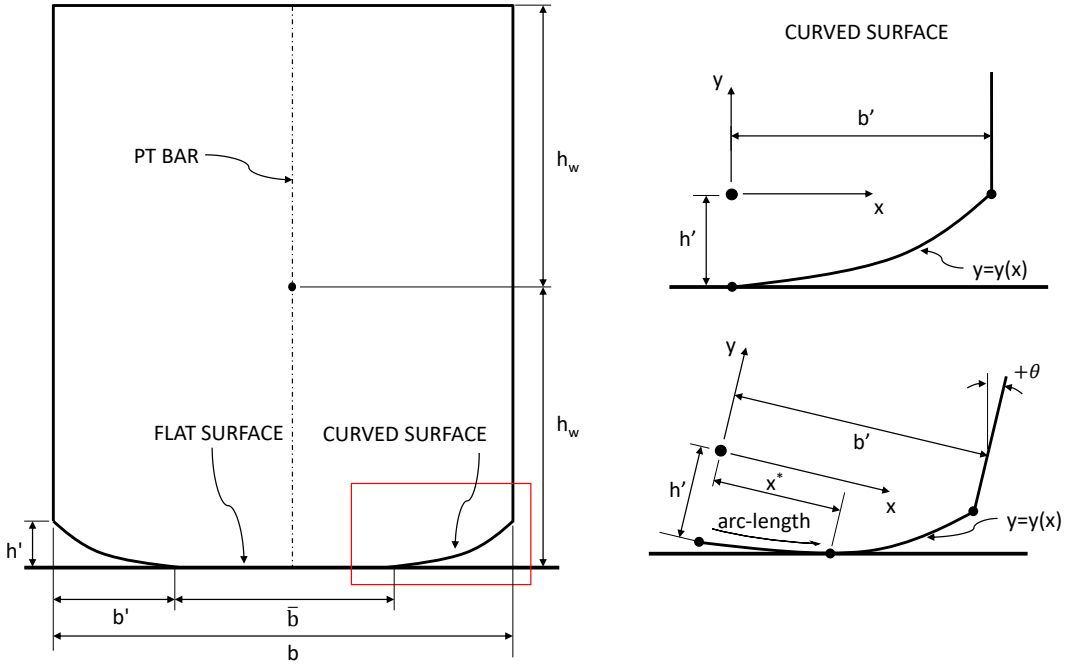

Figure 2.2: Curved-base rocking wall.

2.1.3 Curved-base rocking wall modeling assumptions

The focus of this chapter is to characterize the fundamental mechanics of the CBRW as idealized in Fig. 2.3. In order to study the inherent properties specific to the CBRW, energy dissipation devices were omitted here. It is envisioned that the CBRW will ultimately be used in concert with one of many existing dissipation mechanisms. The rocking walls and gravity frame columns and beams (diaphragm) were also idealized as rigid elements to make the study of the rocking system material independent. The contact of the wall and the ground when rocking is assumed to be a line out-of-plane (i.e. a point when modeled in 2D), instead of a surface. Modeling contact surfaces and deformable walls is shown in Chapter 4. It is assumed that no sliding or jumping occurs. This assumption may lead to errors in freestanding blocks (especially wide blocks), however, it is anticipated that the PT force will assist in ensuring these conditions are satisfied. Additionally, sliding restraint may be a desirable design objective. The mass of the wall and floors were lumped at the centroid of

the wall and the beams of the gravity frame, respectively (see Fig. 2.3). This was selected to facilitate the comparison with a lumped mass FE model that will be discussed later. The centroid of the wall was calculated with the assumption that the mass "cut out" to fabricate the curved base is negligible (i.e. the centroid is located at the mid-width and half-height of the wall). This assumption is valid for practical applications of the CBRW. The PT bars were assumed to remain elastic (in practice, the rocking system is designed such that the PT bars will remain elastic in extreme events). The strain of the PT bars were checked in all models throughout the simulation in this chapter to be below the yield strain of typical PT bars of approximately 0.0032. The finite element model, discussed later, is extended in Chapter 4 to included inelastic behavior of the PT bar by allowing the truss element to yield and adding a post-yield stiffness to the element. The analytical formulation, discussed later, does assume the PT bars remain elastic but the model can be used to predict when the PT bars yield. Modeling post-yield behavior of the PT bar is outside the scope of this chapter because elastic PT response is taken to be a reasonable performance objective.

2.1.4 Kinematics

The formulation used herein requires the kinematic relationships between the various locations of the wall (e.g. center of mass, location of PT attachment), and a generalized coordinate. The wall rotation angle — i.e. tilt angle (θ) — is used as the generalized coordinate herein. This single coordinate is sufficient to uniquely describe the restoring force or moment in the system.

The base is partitioned into the curved and flat surfaces (see Fig. 2.2). As a result, there are three different rocking stages:

1. Rocking as a rectangular wall with an effective width ($\bar{b} = b - 2b'$).
2. Rolling on the curved surface.
3. Rocking about the outer corner.

Any number of functions might be suitable for the curved portion of the base, e.g. poly-

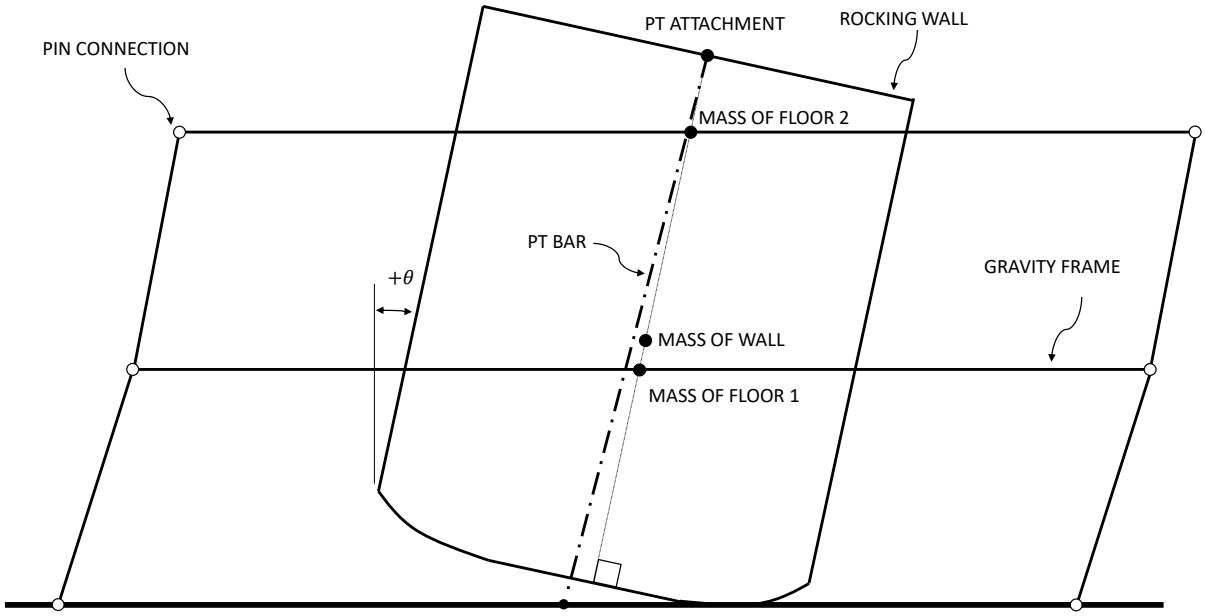

Figure 2.3: Rocking wall and gravity frame system.

nomial, sinusoidal, etc., however, an exponential function was utilized herein. This was done because it is integrable (which will be needed later) and it allows for somewhat independent control of the height, width, and sharpness of the curved section through three parameters h', b', and α, respectively. The curve is given by:

$$y = \beta(e^{\alpha x} - 1) - h' \tag{2.1}$$

where β is a dependent variable given by Eq. (2.2), and x and y are local coordinates (see Fig. 2.2).

$$\beta = \frac{h'}{e^{\alpha b'} - 1} \tag{2.2}$$

The coupling between the three parameters in Eq. (2.2) means that the sharpness of the curve does depend on all three parameters, however, for a given height and width, the α parameter can be used to tailor the sharpness.

For the case of the exponential function used herein for the curved base, θ for stage 2 rocking can be written as a function of x and evaluated at x^*, where x^* is the x-coordinate of the contact point for a given θ (see Fig. 2.2).

$$\tan(\theta) = \left.\frac{dy}{dx}\right|_{x=x^*} = \beta\alpha e^{\alpha x^*} \tag{2.3}$$

Initial values of θ for stage 2 and stage 3 (θ_{1-2} and θ_{2-3}, respectively) can thus be obtained (where $x^* = b'$ for stage 3). For the case of the exponential function used herein, this results in:

$$\theta_{1-2} = \arctan\left(\left.\frac{dy}{dx}\right|_{x=0}\right) = \arctan(\beta\alpha) \tag{2.4a}$$

$$\theta_{2-3} = \arctan\left(\left.\frac{dy}{dx}\right|_{x=b'}\right) = \arctan\left(\beta\alpha e^{\alpha b'}\right) \tag{2.4b}$$

In addition to θ_{1-2} and θ_{2-3}, the horizontal translation during stage 2 can be calculated as the arc length of Eq. (2.1):

$$\text{arc length}(x^*) = \int_0^{x^*} \sqrt{\left[\frac{dy}{dx}\right]_{x=s}^2 + 1}\; ds \tag{2.5}$$

The displaced horizontal and vertical positions of the PT attachment point on the wall, u_{PT} and v_{PT}, are calculated from the following equations depending on the rocking stage — given from Eqs. (2.4a) and (2.4b).

For stage 1:

$$u_{PT} = \bar{b}/2 + R_{PT}\sin(\theta - \phi_{PT}) \tag{2.6a}$$

$$v_{PT} = R_{PT}\cos(\theta - \phi_{PT}) \tag{2.6b}$$

$$R_{PT} = \sqrt{(\bar{b}/2)^2 + (2h_w)^2} \tag{2.6c}$$

$$\phi_{PT} = \arctan\left(\frac{\bar{b}/2}{2h_w}\right) \tag{2.6d}$$

For stage 2 (Fig. 2.4):

$$u_{PT} = R_{PT}\sin(\theta - \phi_{PT}) + \bar{b}/2 + \text{arc length}(x) - x(\theta)\cos(\theta) - y(\theta)\sin(\theta) \tag{2.7a}$$

$$v_{PT} = R_{PT}\cos(\theta - \phi_{PT}) + x(\theta)\sin(\theta) - y(\theta)\cos(\theta) \tag{2.7b}$$

$$R_{PT} = \sqrt{(\bar{b}/2)^2 + (2h_w - h')^2} \tag{2.7c}$$

$$\phi_{PT} = \arctan\left(\frac{\bar{b}/2}{2h_w - h'}\right) \tag{2.7d}$$

For stage 3:

$$u_{PT} = \bar{b}/2 + \text{arc length}(b') - b'\cos(\theta) + R_{PT}\sin(\theta - \phi_{PT}) \tag{2.8a}$$

$$v_{PT} = b'\sin(\theta) + R_{PT}\cos(\theta - \phi_{PT}) \tag{2.8b}$$

where h_w is the half-height of the wall. Similarly, the displaced positions of the centroid of the wall, u_w and v_w, are calculated by substituting $2h_w$ with h_w in Eqs. (2.6c), (2.6d), (2.7c) and (2.7d).

The kinematic equations provided in this section are sufficient to calculate the displacement of any point on the wall as a function of θ, and are necessary to solve the governing equation for the CBRW discussed later.

Kinematics of the gravity frame

Rocking wall systems are typically used in combination with a separate gravity load-resisting system that delivers the seismic inertial lateral force through special diaphragm connections [Priestley, 1991; Pampanin et al., 2001; Wichman, 2018; Pei et al., 2019], with one example in Fig. 2.5. The connections between the lateral and gravity systems are assumed to have several constraints: (i) the node that connects the gravity frame to the wall is permitted to move freely (frictionless) along the wall's center line, see Fig. 2.5, (as a result, the force exerted by the gravity frame on the wall is normal to the center line), (ii) beams (or diaphragms)

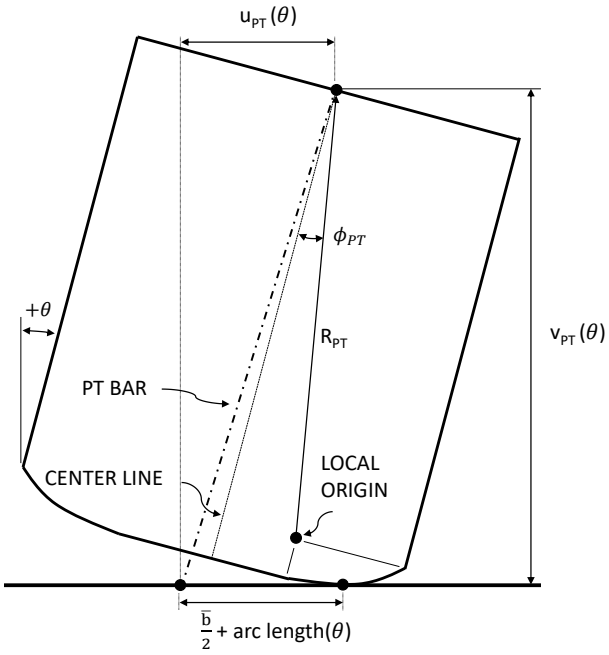

Figure 2.4: PT bar displaced position under stage 2 rocking.

from the gravity frame remain horizontal, and (iii) the beam-column and column-ground connections for the gravity frame carry insignificant moments and are thus modeled as pin connections. As a consequence, the lateral system must carry second-order geometric non-linearity gravity moments (defined herein as P-Delta).

For the assumed gravity frame to wall connections, the following kinematic relations between θ and the displaced position of the floors, u_i and v_i, were derived for a two-story frame (see Fig. 2.6), where i denotes the floor number.

For floor 1:

$$\tan(\theta) = \frac{\overline{u}_1 - u_1}{\overline{v}_1 - v_1} \tag{2.9a}$$

$$v_1 = \sqrt{h_1^2 - u_1^2} \tag{2.9b}$$

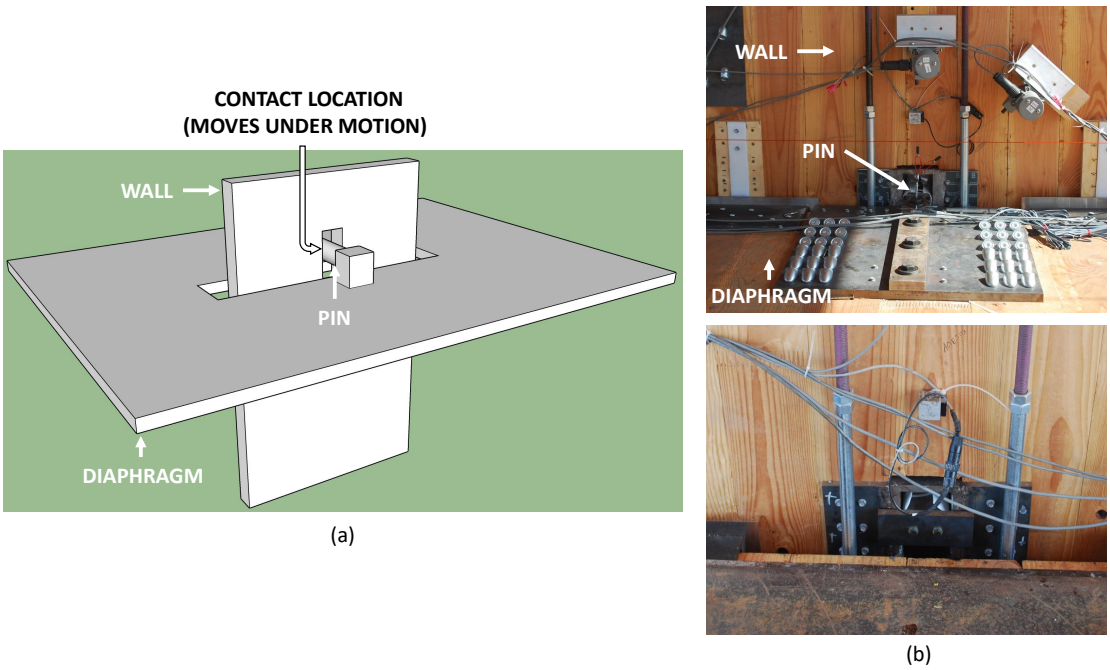

Figure 2.5: Vertical slot and pin connection: (a) Diagram; (b) photo from shake table test [Wichman, 2018].

For floor 2:

$$\tan(\theta) = \frac{\overline{u}_2 - u_2}{\overline{v}_2 - v_2} \tag{2.10a}$$

$$v_2 = v_1 + \sqrt{h_2^2 - (u_2 - u_1)^2} \tag{2.10b}$$

where $\overline{u}_i$ and $\overline{v}_i$ are the horizontal and vertical displaced position of the prior connection points (i.e. the contact location when the structure is plumb) and are known via Eqs. (2.7a), (2.7b), and (2.8), see Fig. 2.6.

These exact equations are cumbersome, hence u_i and v_i are solved numerically and their partial derivatives are approximated, as will be discussed later.

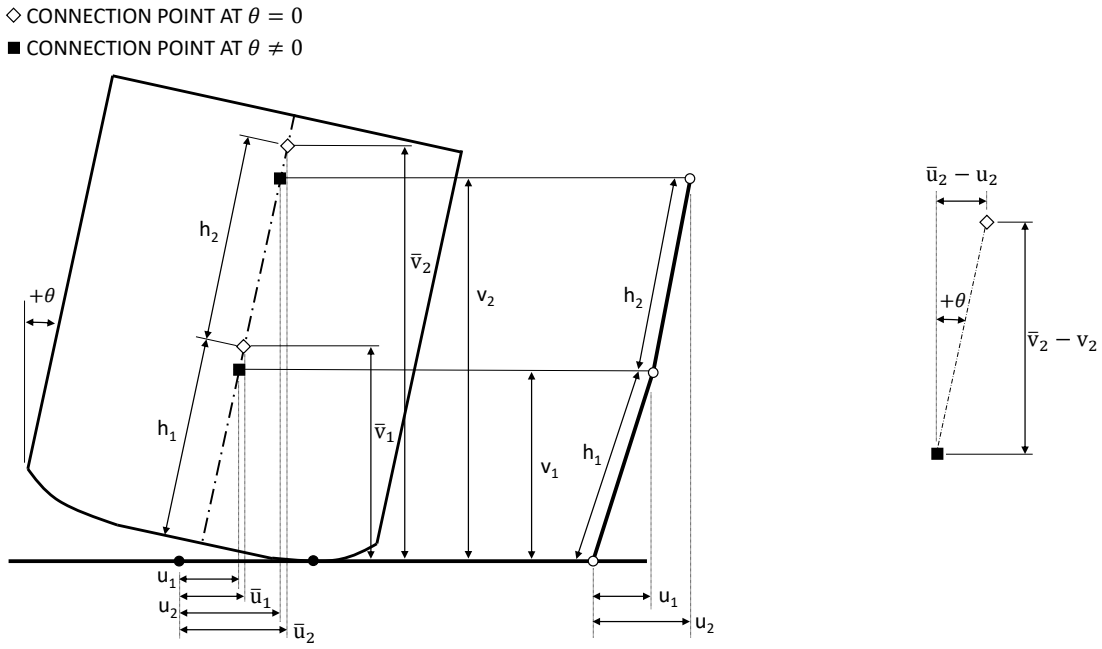

Figure 2.6: Displaced position of the gravity frame.

2.2 Formulation of governing equations

2.2.1 Lagrangian formulation

This study focuses on an analytical approach that allows: for a fundamental understanding of the behavior of rocking walls; insight into key parameters that drive response; enables an efficient parametric study; and can be used to validate the FE models. The analytical formulation of the governing equation (i.e. equation of motion) is derived using the Lagrange equation,

$$\frac{d}{dt}\left(\frac{\partial T}{\partial \dot{\theta}}\right) - \frac{\partial T}{\partial \theta} + \frac{\partial V}{\partial \theta} = 0 \tag{2.11}$$

where T and V are the kinetic and potential energy, respectively, and the time derivative is represented by a dot above the variable. The gradient of the potential energy represents the only term that remains in the static case, and is termed $M_{restoring}$. With the kinetic energy

terms denoted as $M_{inertial}$, Eq. (2.11) can be rewritten as,

$$M_{inertial} + M_{restoring} = 0 \tag{2.12}$$

Note that the external bending moment comes from ground motion contribution of $M_{inertial}$. The two terms in Eq. (2.12) are further expanded and discussed in the following subsections.

Potential energy

The potential energy, V, is given in the following:

$$V = \frac{1}{2}k\Delta^2 + g\left(m_w v_w + \sum_{i=1}^{n} m_i v_i\right) \tag{2.13a}$$

$$\Delta = \sqrt{u_{PT}^2 + v_{PT}^2} - L_o \tag{2.13b}$$

$$n = \text{number of floors} \tag{2.13c}$$

where k, Δ, L_o, and g are the PT stiffness, PT elongation (measured from the zero stress state), initial unstressed PT bar length, and acceleration due to gravity, respectively. The mass of the wall and floors are denoted as m_w and m_i, respectively. Taking the partial derivative of V with respect to θ gives,

$$M_{restoring} = \frac{\partial V}{\partial \theta} = k\Delta\frac{\partial \Delta}{\partial \theta} + g\left(m_w\frac{\partial v_w}{\partial \theta} + \sum_{i=1}^{n} m_i\frac{\partial v_i}{\partial \theta}\right) \tag{2.14}$$

Note that the contribution of the floor masses to the gradient of the potential energy produces a P-Delta effect.

Kinetic energy

The $M_{inertial}$ term is solved by expanding and differentiating T from Eq. (2.11), where T, ignoring the mass of the PT, is given as:

$$T = \frac{1}{2} m_w (\dot{u}_w^2 + \dot{v}_w^2) + \frac{1}{2} \sum_{i=1}^{n} m_i (\dot{u}_i^2 + \dot{v}_i^2) \tag{2.15}$$

where $\dot{u}$ and $\dot{v}$ are the horizontal and vertical velocity of the wall and floor masses. Further, this approach only holds for lumped masses. For heavy walls (significant distributed mass) a consistent mass approach (or discretization of the wall) would likely produce better results. Differentiating Eq. (2.15) gives

$$\frac{\partial T}{\partial \dot{\theta}} = m_w \left(\dot{u}_w \frac{\partial \dot{u}_w}{\partial \dot{\theta}_w} + \dot{v}_w \frac{\partial \dot{v}_w}{\partial \dot{\theta}_w} \right) + \sum_{i=1}^{n} m_i \left(\dot{u}_i \frac{\partial \dot{u}_i}{\partial \dot{\theta}_i} + \dot{v}_i \frac{\partial \dot{v}_i}{\partial \dot{\theta}_i} \right) \tag{2.16a}$$

$$= m_w \left(\dot{u}_w \frac{\partial u_w}{\partial \theta_w} + \dot{v}_w \frac{\partial v_w}{\partial \theta_w} \right) + \sum_{i=1}^{n} m_i \left(\dot{u}_i \frac{\partial u_i}{\partial \theta_i} + \dot{v}_i \frac{\partial v_i}{\partial \theta_i} \right) \tag{2.16b}$$

where the equivalence of Eqs. (2.16a) and (2.16b) is based on Greenwood [Greenwood, 1997]. It follows that

$$\begin{aligned} \frac{d}{dt}\left(\frac{\partial T}{\partial \dot{\theta}} \right) = m_w \left(\ddot{u}_w \frac{\partial u_w}{\partial \theta} + \dot{u}_w \frac{\partial \dot{u}_w}{\partial \theta} + \ddot{v}_w \frac{\partial v_w}{\partial \theta} + \dot{v}_w \frac{\partial \dot{v}_w}{\partial \theta} \right) \\ + \sum_{i=1}^{n} m_i \left(\ddot{u}_i \frac{\partial u_i}{\partial \theta} + \dot{u}_i \frac{\partial \dot{u}_i}{\partial \theta} + \ddot{v}_i \frac{\partial v_i}{\partial \theta} + \dot{v}_i \frac{\partial \dot{v}_i}{\partial \theta} \right) \end{aligned} \tag{2.17a}$$

$$\frac{\partial T}{\partial \theta} = m_w \left(\dot{u}_w \frac{\partial \dot{u}_w}{\partial \theta} + \dot{v}_w \frac{\partial \dot{v}_w}{\partial \theta} \right) + \sum_{i=1}^{n} m_i \left(\dot{u}_i \frac{\partial \dot{u}_i}{\partial \theta} + \dot{v}_i \frac{\partial \dot{v}_i}{\partial \theta} \right) \tag{2.17b}$$

After some manipulation and combining Eqs. (2.17a) and (2.17b):

$$\frac{d}{dt}\left(\frac{\partial T}{\partial \dot{\theta}}\right) - \frac{\partial T}{\partial \theta} = m_w\left[\left(\frac{\partial u_w}{\partial \theta}\ddot{\theta} + \frac{\partial^2 u_w}{\partial \theta^2}\dot{\theta}^2\right)\frac{\partial u_w}{\partial \theta} + \left(\frac{\partial v_w}{\partial \theta}\ddot{\theta} + \frac{\partial^2 v_w}{\partial \theta^2}\dot{\theta}^2\right)\frac{\partial v_w}{\partial \theta}\right] + \sum_{i=1}^{n} m_i\left[\left(\frac{\partial u_i}{\partial \theta}\ddot{\theta} + \frac{\partial^2 u_i}{\partial \theta^2}\dot{\theta}^2\right)\frac{\partial u_i}{\partial \theta} + \left(\frac{\partial v_i}{\partial \theta}\ddot{\theta} + \frac{\partial^2 v_i}{\partial \theta^2}\dot{\theta}^2\right)\frac{\partial v_i}{\partial \theta}\right] \tag{2.18}$$

By separating u into the relative and ground motion terms ($u \rightarrow u + u_g$), the contribution from the ground motion can be separated (same can be done with v if necessary):

$$M_{inertial} = \frac{d}{dt}\left(\frac{\partial T}{\partial \dot{\theta}}\right) - \frac{\partial T}{\partial \theta} = I_{dyn}(\theta)\ddot{\theta} + G(\theta)\dot{\theta}^2 + M_g(t,\theta) = 0 \tag{2.19}$$

where,

$$I_{dyn}(\theta) = m_w\left[\left(\frac{\partial u_w}{\partial \theta}\right)^2 + \left(\frac{\partial v_w}{\partial \theta}\right)^2\right] + \sum_{i=1}^{n} m_i\left[\left(\frac{\partial u_i}{\partial \theta}\right)^2 + \left(\frac{\partial v_i}{\partial \theta}\right)^2\right] \tag{2.20a}$$

$$G(\theta) = m_w\left[\left(\frac{\partial^2 u_w}{\partial \theta^2}\right)\frac{\partial u_w}{\partial \theta} + \left(\frac{\partial^2 v_w}{\partial \theta^2}\right)\frac{\partial v_w}{\partial \theta}\right] + \sum_{i=1}^{n} m_i\left[\left(\frac{\partial^2 u_i}{\partial \theta^2}\right)\frac{\partial u_i}{\partial \theta} + \left(\frac{\partial^2 v_i}{\partial \theta^2}\right)\frac{\partial v_i}{\partial \theta}\right] \tag{2.20b}$$

$$M_g(t,\theta) = \left(m_w\frac{\partial u_w}{\partial \theta}\right)\ddot{u}_g + \sum_{i=1}^{n}\left(m_i\frac{\partial u_i}{\partial \theta}\right)\ddot{u}_g \tag{2.20c}$$

and M_g is the bending moment 'forcing' induced by the ground motion about the base. G is referred to herein as the gyroscopic term, as it captures the translation-roll coupling, and only appears in the solution for a curved-base wall. Bachmann et al. provided the equation of motion for a curved-base rocking column with constant curvature which also included $G(\theta)\dot{\theta}^2$ [Bachmann et al., 2016].

If a rectangular wall is considered (without the gravity frame), the rigid body translation is removed and all that remains is rigid body rotation. In that case, Eq. (2.20) yields the commonly seen equation of motion where $I_{dyn} = mR^2$ and $G = 0$.

2.2.2 Approximate formulation

The equations formulated in previous sections are exact and can be solved for rectangular and curved-base rocking walls. However, when incorporating the gravity frame system through the diaphragm-wall connection, the kinematic equations relating gravity frame displaced position with respect to θ become cumbersome because the diaphragm-wall contact points are not fixed on the wall. Approximate numerical solutions for the potential energy and kinetic energy are discussed separately in the next subsections and employed in pushover and dynamic analyses using programs written in MATLAB [MATLAB, 2017] in later sections.

Potential energy

The potential energy term of the gravity frame produces a P-Delta effect but the partial derivative terms for the gravity frame cannot be solved easily. However, a direct equilibrium approach offers a simpler alternative route to obtaining P-Delta. For this approach, Eq. (2.14) can be modified into the following:

$$M_{restoring} = k\Delta\frac{\partial\Delta}{\partial\theta} + m_w g\frac{\partial v_w}{\partial\theta} + M_{PDelta} \tag{2.21}$$

where,

$$M_{PDelta} = (F_{f1}v_1 + F_{f2}v_2)\cos(\theta) + [F_{f1}(u_1 - \overline{u}) + F_{f2}(u_2 - \overline{u})]\sin(\theta) \tag{2.22a}$$

$$F_{f2} = \frac{m_2 g(u_2 - u_1)}{\cos(\theta)(v_2 - v_1) + \sin(\theta)(u_2 - u_1)} \tag{2.22b}$$

$$F_{f1} = \frac{m_2 g u_2 + m_1 g u_1 - F_{f2}\cos(\theta)v_2 - F_{f2}\sin(\theta)u_2}{\cos(\theta)v_1 + \sin(\theta)u_1} \tag{2.22c}$$

These equations are based on Fig. 2.7, which shows the gravity frame forces used to derive Eqs. (2.22a), (2.22b), and (2.22c). These equations use the floor position, which can be solved from Eqs. (2.9) and (2.10), either closed-form (cumbersome) or numerically.

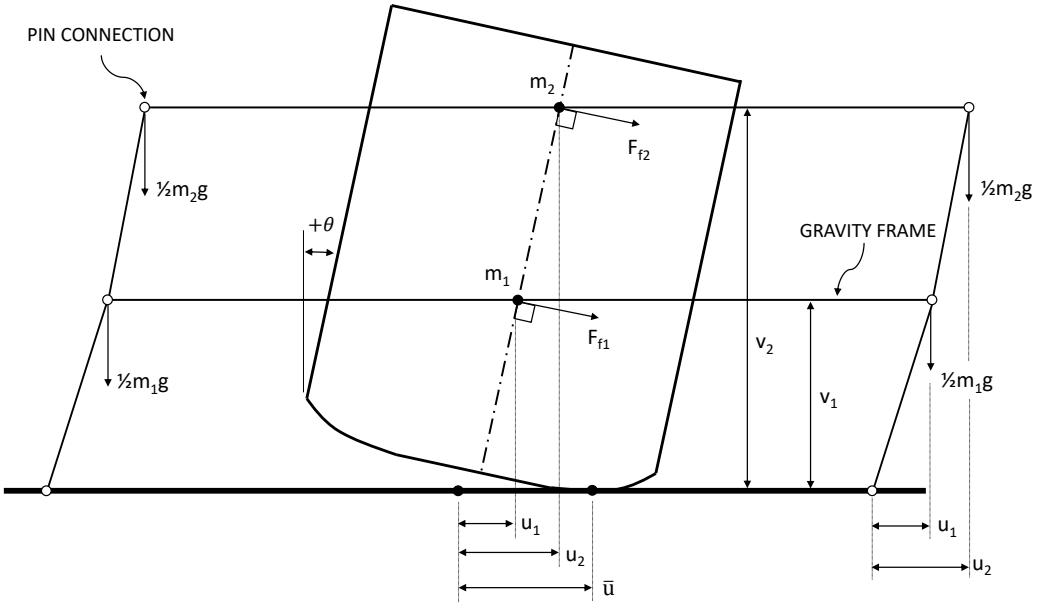

Figure 2.7: P-Delta forces.

Kinetic energy

The kinetic energy is more difficult requiring higher derivatives of the floor positions, and because no simple equilibrium alternative can be used. Two different methods were used to solve the kinetic energy term and are discussed in this section. The first is using finite difference method on the numerical solutions of Eqs. (2.9) and (2.10) to obtain the partial derivatives for the gravity frame terms in Eq. (2.20). This method is particularly complex when solving for different wall geometries and is implemented only as a way to check the second approximate method for the kinetic term (discussed next) and the FE model.

The second method is by using the equation of motion of a rectangular wall (see Appendix A) for a CBRW and ignoring the gyroscopic term in Eq. (2.19). The effect from the gyroscopic

term is further explored in Appendix B. Equation (2.18), thus simplifies to Eq. (2.23)

$$M_{inertial} = \frac{d}{dt}\left(\frac{\partial T}{\partial \dot{\theta}}\right) - \frac{\partial T}{\partial \theta} = I_{inst}\ddot{\theta} + M_{g,inst} \tag{2.23}$$

where I_{inst} is the instantaneous moment of inertia of the wall and gravity frame system and $M_{g,inst}$ is the external moment caused by the ground motions. Figure 2.8 illustrates the inertial forces of the floor masses on the CBRW used to derive the equations to calculate I_{inst} and $M_{g,inst}$. Therefore,

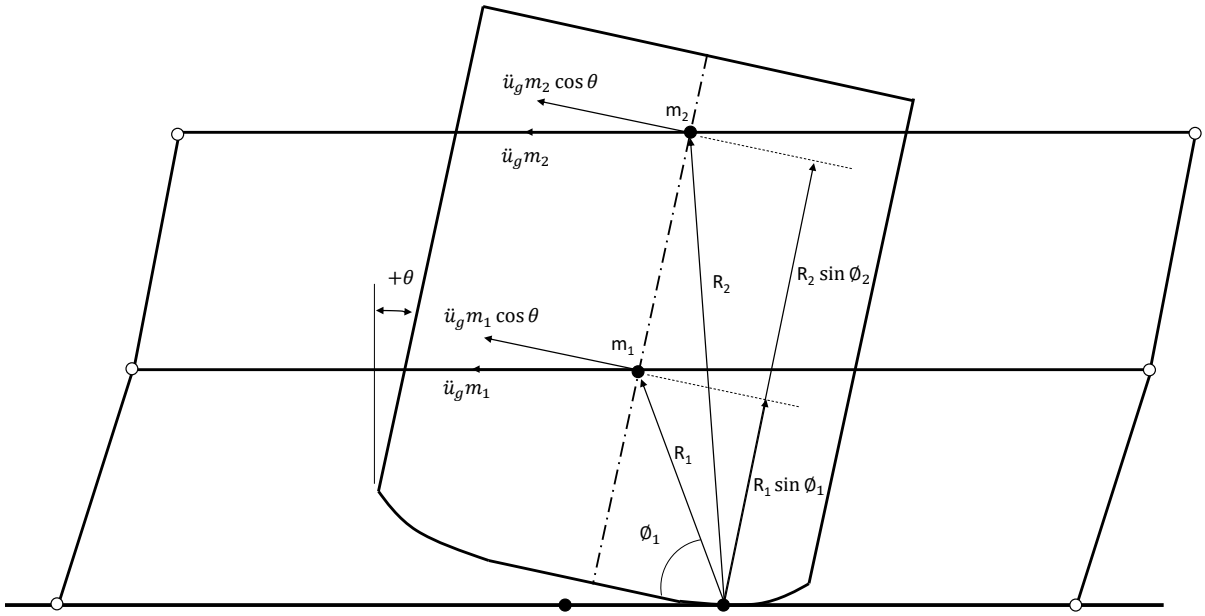

Figure 2.8: Instantaneous inertial forces of floor mass.

$$I_{inst} = I_w + \sum_{i=1}^{n} m_i R_i^2 \cos(\theta)\sin(\phi_i) \tag{2.24a}$$

$$M_{g,inst} = \ddot{u}_g\left(m_w v_w + \sum_{i=1}^{n} m_i R_i \cos(\theta)\sin(\phi_i)\right) \tag{2.24b}$$

where R_i and ϕ_i — as shown in Fig. 2.8 — are the radial distance from the center of rotation

to the lumped masses and the angle between R_i and the base of the wall, respectively.

Again, note that the instantaneous inertia incorrectly assumes the wall is rotating about the point of contact without additional related translation due to the curved base. The gyroscopic terms capture the translation-rotation coupling.

Nonlinear time-history analyses were performed using Eqs. (2.21) and (2.23) solved using Newmark's method. Analyses using Eqs. (2.21) and (2.19) (solved using Classical Runge-Kutta method) were also performed to check the FE model and the approximate method for the kinetic term that neglected G.

2.2.3 Energy dissipation from impact

The derivation of the aforementioned governing equations neglected damping, though rocking systems manifest damping from a variety of sources: energy dissipation devices, friction and yielding of structural and non-structural components, and base-ground impact damping. For this study, only impact damping was considered in order to better isolate the effects of CBRWs. As mentioned previously, Housner showed how impact damping of a rocking rigid body can be calculated simply using the geometry of the wall, independent from material properties [Housner, 1963]. This is possible if only considering one rocking joint, assuming no sliding or bouncing, and only for rigid walls, and assuming all impact stress occurs at the rocking point. Note that Chapter 3 extends this solution to flexible rocking bodies. The reduction in kinetic energy during impact (r) for the wall only is thus given in Eq. (2.25). Note that some original notations were changed to prevent confusion with notations used in this chapter.

$$r = \left(\frac{\dot{\theta}_2}{\dot{\theta}_1}\right)^2 = \left(\frac{I_w - 2m_w R_w \bar{b}\sin(\phi_w)}{I_w}\right)^2 = \left\{1 - \frac{m_w R_w^2}{I_w}[1 - cos(2\phi_w)]\right\}^2 \quad (2.25)$$

where ϕ_w and R_w are calculated with Eqs. (2.6c) and (2.6d) using h_w instead of $2h_w$.

Modifications to Eq. (2.25) were necessary to couple the gravity frame with the wall. Keeping with the same approach as Housner, the angular momentum of the wall and gravity frame system before and after impact was conserved to get the reduction in kinetic energy. This is best done about the 'after impact' rocking point. Figure 2.9 illustrates the velocities of the wall and floor masses right before and after impact. Equation (2.25) can thus be modified to Eq. (2.26) in order to account for the mass in the gravity fame:

$$r = \left(\frac{\dot{\theta}_2}{\dot{\theta}_1}\right)^2 = \left[\frac{I_{dyn} - 2m_w R_w \bar{b}\sin(\phi_w)}{I_{dyn}}\right]^2 \tag{2.26}$$

Equation (2.25) shows that the mass does not affect r — i.e. does not affect impact damping when only the wall is considered, as I_w is proportional to m_w. However, Eq. (2.26) indicates that for a rocking wall and gravity frame system, the impact damping decreases as the mass of the floors increases relative to the mass of the wall (i.e. I_{dyn} grows). This could affect design considerations if impact damping is to be considered in the design calculations. Impact damping in the results shown later was included into the nonlinear time-history analysis by multiplying $\dot{\theta}$ by the square root of r after each impact. Crucially, a massless (assumed) PT cable does not impart an impulse during rocking as it is displacement controlled. Thus, the PT does not change the coefficient of restitution (although indirectly it may change the typical velocity during rocking events). This was also used by Dimitrakopoulos and DeJong [Dimitrakopoulos and DeJong, 2012].

2.3 Comparison with finite element model

In practice, FE analysis of CBRWs will be necessary to address walls with shear and bending deformation, distributed rocking surface with damage models, and energy dissipation devices. In this section, a method for simulating the behavior of CBRWs is described and compared with the analytical formulations. Both pushover (elastic) and nonlinear time-history analyses with FE models in OpenSees [McKenna, 1997] are described here.

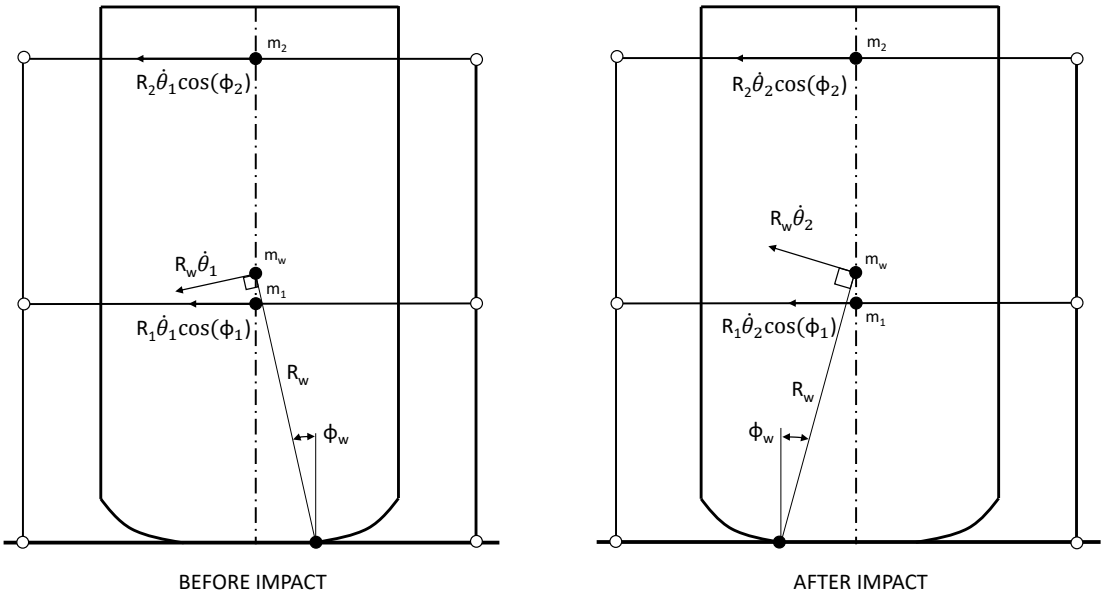

Figure 2.9: Velocities before and after impact.

2.3.1 Finite element model

The design of the post-tensioning, wall, and gravity system was roughly based on the structure used in a CLT rocking wall shake table test specimen shown in Fig. 2.1 [Wichman, 2018; Pei et al., 2019]. The following modifications were made to the original design: (1) curving the base, (2) modeling only one panel of one of the coupled rocking walls and a corresponding one-quarter of the gravity system mass, (3) removing the UFPs, (4) relocating the PT bars to a single concentric location, and (5) idealizing the wall, beams, and columns as rigid elements. The schematic of the simplified specimen but as a CBRW is shown in Fig. 2.10 and the values for key parameters are given in Table 2.1. Note that the values of the parameters for the curved base provided in the next two sections were not optimized in any way. Instead, they were chosen to show the differences between the pushover backbone of a CBRW and a rectangular wall (static analysis comparison) and to induce more stage 2 rocking (dynamic analysis comparison). The concentrated lateral force for the pushover

analyses was applied at the PT attachment point at the top of the wall. A preliminary study of performance benefits is in the following section.

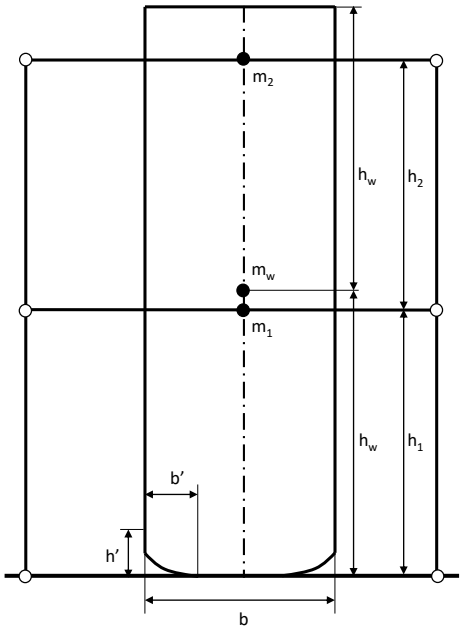

Figure 2.10: Curved-base rocking wall and gravity frame system.

The wall, beams, and columns of the gravity frame were modeled in OpenSees with very stiff beam-column elements. In order to prevent sliding, stiff shear springs were connected from the base of the wall to the ground via truss elements. The diaphragms (i.e. floors) were connected to the wall by vertical beam-column elements with a large bending stiffness and low axial stiffness to model the vertical slot and pin connection mentioned previously. The curved base was modeled with rigid zero-length compression-only springs with gap parameters (*elastic perfectly plastic gap* in OpenSees) distributed with the Legende-Gauss-Lobatto integration scheme. The values used for the gap parameter was zero for the flat surface and varied, using Eq. (2.1), along the curved surface so as to create the desired shape of the curve with a finite number of springs. As mentioned before, the contact between the wall and the ground when rocking is modeled as a single contact point. Figure 2.11 shows

h_w (in)	144
h_1 (in)	146
h_2 (in)	120
b (in)	60
m_w (kip/in/s^2)	0.0055
m_1 (kip/in/s^2)	0.0594
m_2 (kip/in/s^2)	0.0612
Total PT area (in^2)	1.7668
Total initial PT force (kip)	48
E_{PT} (ksi)	29000

Table 2.1: Rocking wall design.

a diagram of the finite element model, the zero-length compression-only springs, and the force-deformation plot of the compression-only spring. Note, only a schematic is shown and actually a total of 300 compression-only springs were used to model the curved part of the base and 301 compression-only springs were used to model the flat part of the base.

2.3.2 Pushover analysis

Figure 2.12 includes the design values for the curved base parameters used in this section and shows the pushover results of the CBRW and the rectangular wall. The pushover results show $M_{restoring}$ normalized by their respective decompression moment, M_{dec}, versus drift. M_{dec} is defined herein as the moment required for the wall to uplift (125.38 kip-ft and 25.08 kip-ft for the rectangular wall and CBRW, respectively). Note that the CBRW uses the same parameters in Table 2.1 with additional curved base parameters seen in Fig. 2.12. The pushover analyses show that the potential energy terms and the kinematic equations match with the FE model. Although unobservable in Fig. 2.12, there are discontinuities during stage 2 in the FE analysis due to the finite number of compression-only springs in the base. It becomes smoother as the number of springs increases. The M_{dec} of the CBRW is lower than the rectangular rocking wall (as expected because of the reduction in $\bar{b}$), which can be offset by using a larger PT area and initial PT force, as will be discussed later. The

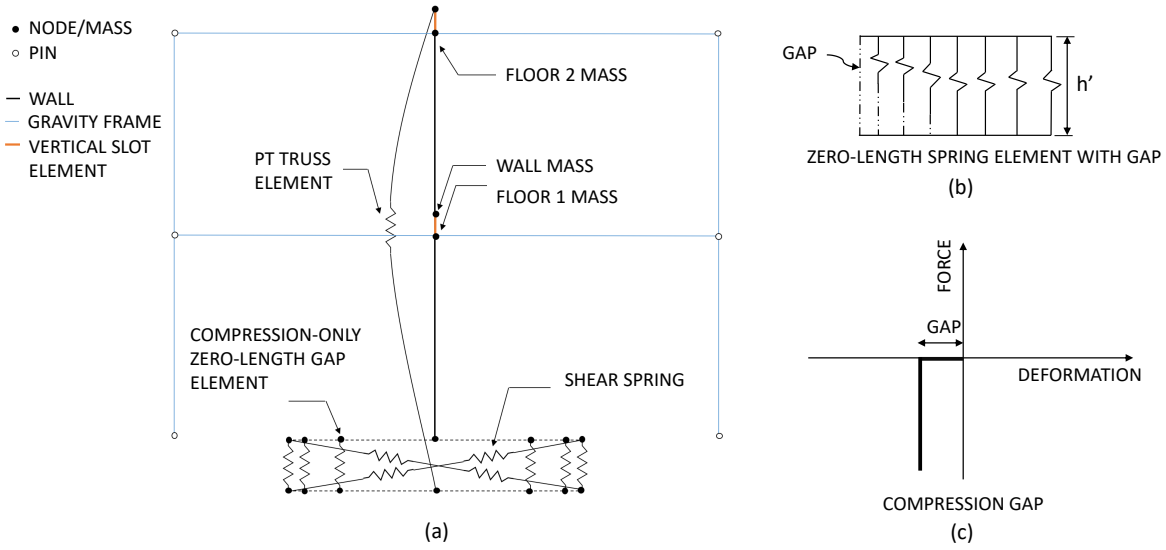

Figure 2.11: Finite element model: (a) Model; (b) zero-length spring element; and (c) force-displacement relationship of zero-length spring element.

M_{dec} is largely determined by the initial PT force and the width of the base. The initial PT force required depends on expected lateral loads (e.g. wind loads) the wall needs to resist without rocking. The initial PT force is limited by the compressive strength of the wall and the allowed drift at which the PT bar starts to yield. A higher PT force would lead to wall compression failure and PT bar yielding at lower drifts. However, lateral load demands and compressive strength of the wall are outside the scope of this chapter but are included in Chapter 4. Figure 2.12 shows the drift is zero until the joint opens, which is the case when the structure and contact surface is assumed to be rigid. However, in experimental results, drift linearly increases with lateral force until the joint opens. After the joint opens, the drift increases linearly with a reduced stiffness. This is caused by the flexibility in the structure (e.g. rocking wall) and the flexibility in the contact surface, as will be shown in Chapters 3 and 4.

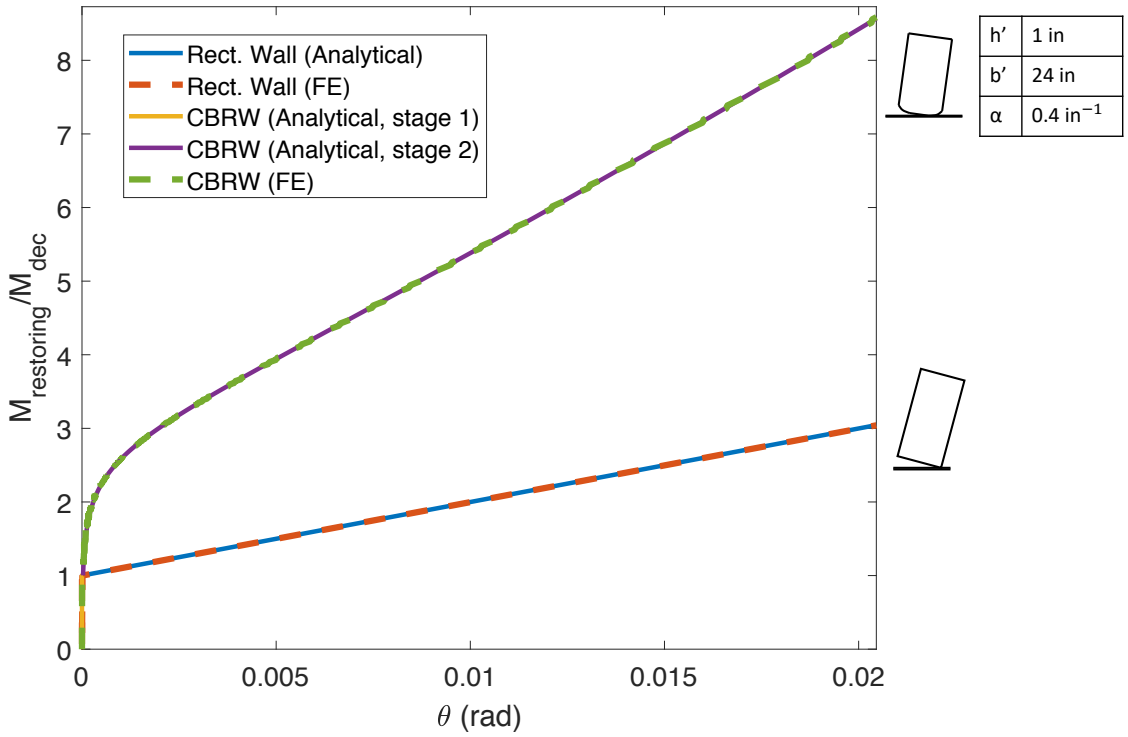

Figure 2.12: Comparison of pushover response of the analytical equations and the finite element model.

2.3.3 Nonlinear time-history analysis

Figure 2.13 includes the values for the curved base parameters used in this section. Impact damping was neglected here in order to isolate the effects of the governing equations derived in the previous section. Undamped free vibration simulations were performed; the analysis, in effect, captured the resonant frequency of the CBRW. Note the resonant frequency is amplitude dependent, as will be discussed later. Figure 2.13 shows a plot of θ versus time from the analytical equations (with approximate $M_{inertial}$) and the FE model. It is clear that all equations and the FE model agree. This signifies that approximating the governing equation of a CBRW by neglecting the translational kinetic energy gives acceptable results, for the parameters and amplitudes considered here.

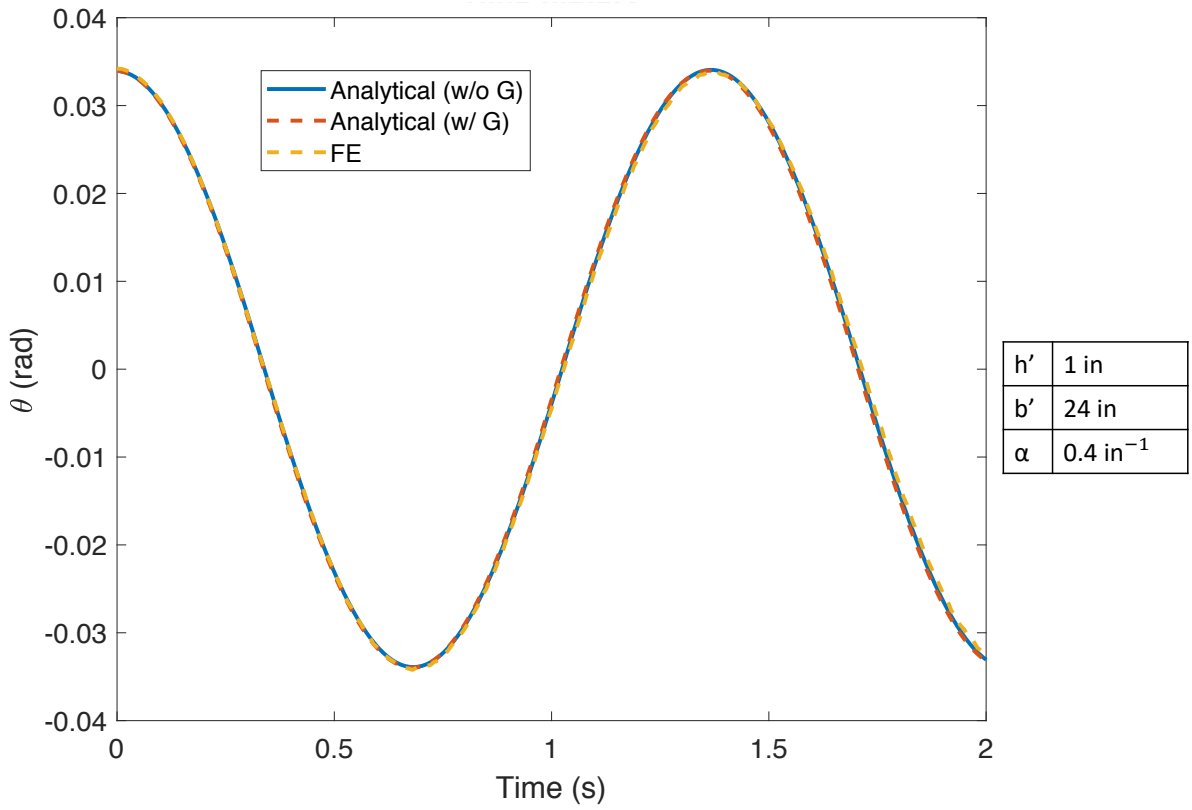

Figure 2.13: Response-history.

2.4 Performance comparison between curved-base rocking wall and rectangular wall

Traditional rectangular rocking walls, as mentioned before, have some disadvantages that may detract from their benefits. One of the most critical issues is the potential for the PT to yield or rupture. The former decreases re-centering capacity (one of the main purposes of rocking walls) and the latter could lead to collapse. A simple solution would be to use CBRWs to increase the drift at PT yield, defined herein as $\delta_y = u_{y,PT}/2h_w$, where $u_{y,PT}$ is the horizontal displacement of the PT attachment point when the PT bar starts to yield. The yield criterion of the PT bar is assumed herein as a function of the yield strain of the chosen PT bar material (PT bars often are made from steel with approximate yield strain

of 0.0032). Strain in the PT bar can be calculated from PT elongation given in Eq. 2.13b. This section compares δ_y and the nonlinear dynamic response of CBRWs to rectangular walls. Furthermore, this section also discusses rectangular walls with varying widths, with CBRWs fitting within the rectangular wall envelope. This approach was used to show the improvements offered by CBRWs within a given wall envelope. A larger parametric study and optimization is beyond the scope of this chapter. The design is again given in Table 2.1, while modifications to the design and the parameters for the curved base are provided in their respective subsections.

2.4.1 Drift at PT yield

Pushover analyses were performed using Eq. (2.21). δ_y was calculated using the kinematic equations and strain-displacement equations.

Several curved base configurations were used to investigate the interactions between the curved base parameters (specifically b'), post-tensioning, and δ_y. In addition, rectangular walls with same CBRW widths, i.e. $b = \overline{b}$ of the CBRWs, were also included for comparison. Tables 2.2 and 2.3 include the design values used for the different rectangular and CBRWs. The design values were chosen to show how the CBRWs could increase δ_y while maintaining the same M_{dec} as the baseline rectangular wall (i.e. original design with parameters given in Table 2.1) denoted herein with the subscript o. For example, A_{PTo} is the total PT area from the baseline wall from Table 2.1. The PT force was increased by increasing the PT area.

Figure 2.14 shows the pushover response up to the onset of PT bar yielding. $M_{restoring}$ was again normalized by M_{dec} (125.38 kip-ft) and were the same for all the walls due to the design process mentioned before. Capacity in Fig. 2.14 refers to the normalized restoring moment at the onset of PT bar yielding, M_y, and θ at the onset of PT bar yielding. The results in Fig. 2.14 are tabulated in Table 2.4 where δ_{yo} and M_{yo} are the drift and restoring moment of the benchmark rectangular wall at the onset of PT bar yielding. Figure 2.14 shows an increase in δ_y for the CBRWs — seen clearer in Table 2.4 — while maintaining the backbone curve of the baseline rectangular wall. This is without a rigorous optimization routine, and

Design	A_{PT}/A_{PTo}	$\overline{b}$ (in)	b' (in)	h' (in)	α (in^{-1})	θ_{1-2} (rad)	θ_{2-3} (rad)
CBRW 1	1.10	55	2.50	0.30	2.50	1.45E-3	0.64
CBRW 2	1.15	52	4.00	1.75	2.50	1.99E-4	1.35
CBRW 3	1.20	50.4	4.80	2.00	1.80	6.37E-4	1.30
CBRW 4	1.25	48.4	5.80	2.00	1.50	5.00E-4	1.25
CBRW 5	1.50	40.64	9.68	5.00	0.90	7.41E-4	1.35
CBRW 6	2.00	30.72	14.64	10.00	0.59	1.05E-4	1.40
CBRW 7	2.50	24.70	17.65	12.00	0.47	1.41E-3	1.40

Table 2.2: Curved-base rocking wall design for comparing drift at PT yield.

Design	A_{PT}/A_{PTo}	b (in)
Baseline	1.0	60
Rect. Wall 1	1.10	55
Rect. Wall 2	1.15	52
Rect. Wall 3	1.20	50.4
Rect. Wall 4	1.25	48.4
Rect. Wall 5	1.50	40.64
Rect. Wall 6	2.00	30.72
Rect. Wall 7	2.50	24.70

Table 2.3: Rectangular wall design for comparing drift at PT yield.

Design	A_{PT}/A_{PTo}	δ_y/δ_{yo}	Post-decomp. stiffness	M_y/M_{yo}
CBRW 1	1.10	1.06	1.00	1.05
CBRW 2	1.15	1.09	1.01	1.07
CBRW 3	1.20	1.13	1.00	1.09
CBRW 4	1.25	1.15	1.02	1.11
CBRW 5	1.50	1.29	1.01	1.21
CBRW 6	2.00	1.53	1.03	1.40
CBRW 7	2.50	1.75	1.06	1.58
Rect. Wall 1	1.10	1.09	0.92	1.00
Rect. Wall 2	1.15	1.15	0.85	0.99
Rect. Wall 3	1.20	1.19	0.84	1.00
Rect. Wall 4	1.25	1.24	0.80	1.00
Rect. Wall 5	1.50	1.48	0.67	0.99
Rect. Wall 6	2.00	1.95	0.49	0.98
Rect. Wall 7	2.50	2.43	0.39	0.96

Table 2.4: Pushover comparison results.

is shown to demonstrate the potential for improvement over the baseline rectangular wall. Conversely, the yield strength of the analogous rectangular walls remained unchanged and the post-decompression stiffness decreased. Note that the pushover analysis in Fig. 2.14 never reached stage 3 rocking as the rectangular baseline wall did not exhibit a softening stage. A quick look into the behavior of stage 3 rocking is provided in the next subsection, however, an in-depth analysis of stage 3 rocking is beyond the scope of this chapter and is left for future study. In addition Fig. 2.14(e) shows an almost linear relationship between A_{PT}/A_{PTo} and δ_y/δ_{yo} if the M_{dec} and post-decompression stiffness are to remain constant; i.e., more PT area is needed to match the stiffness and M_{dec} as the base is curved more to increase the drift at PT yield. The relationship between A_{PT}/A_{PTo} and δ_y/δ_{yo} is a highly complex implicit relationship but is nearly linear despite the nonlinearities in CBRWs. M_{dec}/M_{deco} for rectangular walls remain constant (and equal to 1), see Table 2.4, because the decompression moments were designed to remain the same (i.e. $b * A_{pt}$ is constant, which is the main driving factor of M_y for rectangular walls).

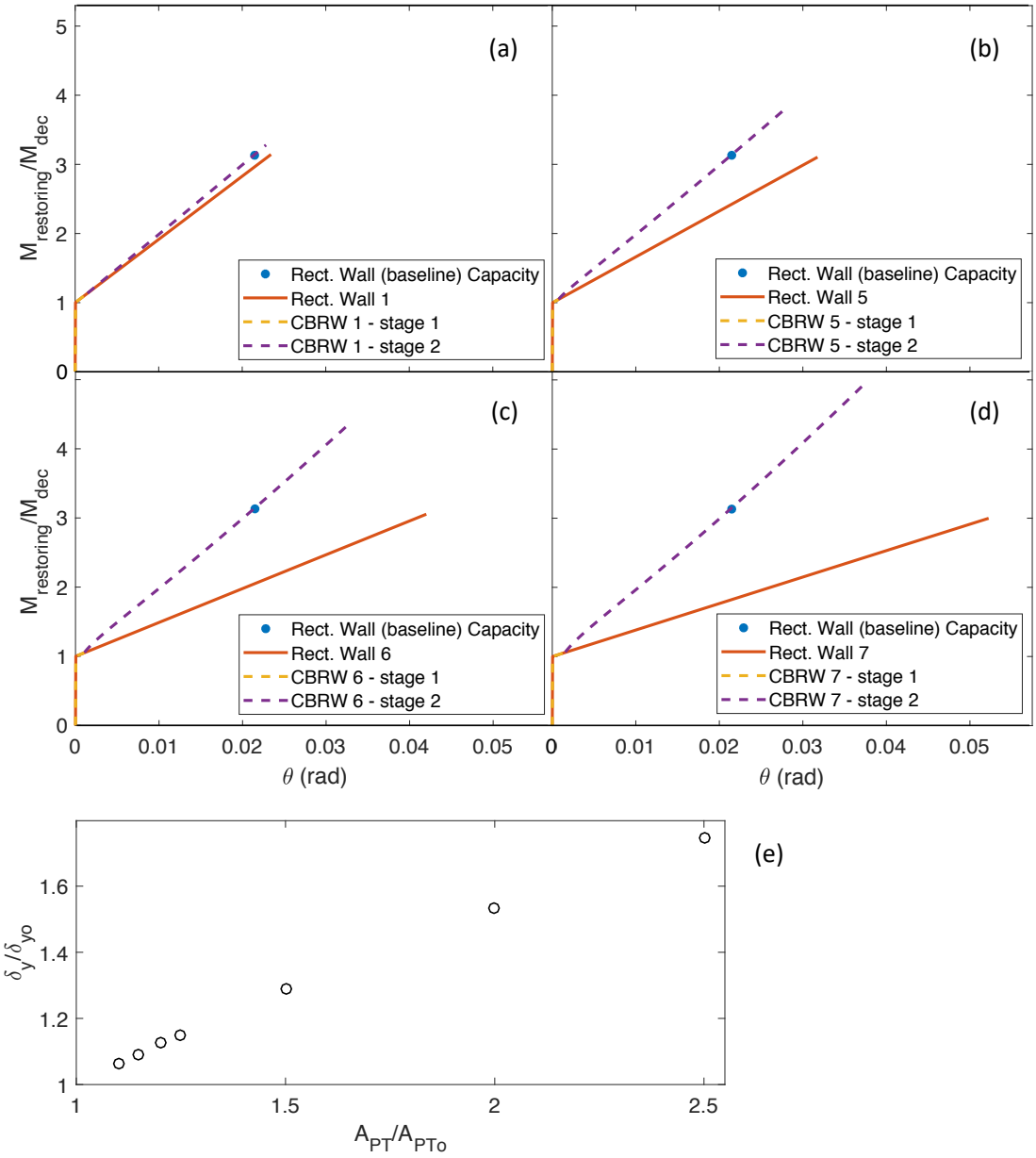

Figure 2.14: Pushover comparison: (a) Design 1; (b) design 5; (c) design 6; (d) design 7; and (e) relationship between and PT bar area and drift at PT bar yield for curved-base rocking walls.

2.4.2 Tailoring curved-base rocking walls

Figure 2.15 illustrates how the CBRW fits in between a narrow and wide wall — on the left is a schematic of the two rectangular walls and two CBRWs (the CBRWs have varying α, b = width of wide rectangular wall, and $\bar{b}$ = width of narrow rectangular wall), on the right shows their respective pushover response. The $M_{restoring}$ reduction from line 1 and line 3 is caused by the horizontal translation and height decrease when transitioning from stage 1 to stage 3 rocking. Here, the post-tensioning remained constant for all four wall geometries. Figure 2.15 illustrates qualitatively how the CBRW can be tailored to behave as both a wide and narrow rectangular wall because of the multiple-rocking stage response. An advantage of CBRWs is the multiple stiffness from the different rocking stages (see Wall 2 in Fig. 2.15). The pushover response can be tailored to different performance objectives. For example: (i) The decompression moment could be designed to exceed the expected wind loads to prevent rocking under wind loads; (ii) the design basis earthquake (10 percent probability of exceedance in 50 years) demands could fall within stage 1 rocking to take advantage of softening to prevent component failure and increase energy dissipation (via energy dissipation device); and (iii) the maximum considered earthquake (2 percent of exceedance in 50 years) could fall within stage 2 rocking where there is hardening to limit drift to prevent structural/non-structural failure. Although not visible in Fig. 2.15, the tailorability of the pushover response also suggests the possibility of tuning multiple natural periods of the rocking system for devices such as tuned mass dampers.

Similarly, Fig. 2.16 illustrates how varying α affects the pushover response (left), plotted up to the onset of PT bar yielding, and also shows a diagram of how the curved surface changes with increasing α (right). The different CBRWs are matched with their respective pushover response using the same color and line styles. There are several things to note in Fig. 2.16: (1) increasing α shifts θ_{1-2} to the left, (2) sensitivity of stage 2 stiffness decreases with increasing α, (3) stage 2 stiffness for a larger α can match stage 3 stiffness of smaller α, and (4) by choosing α properly, the drift at PT yield and yield strength can be improved.

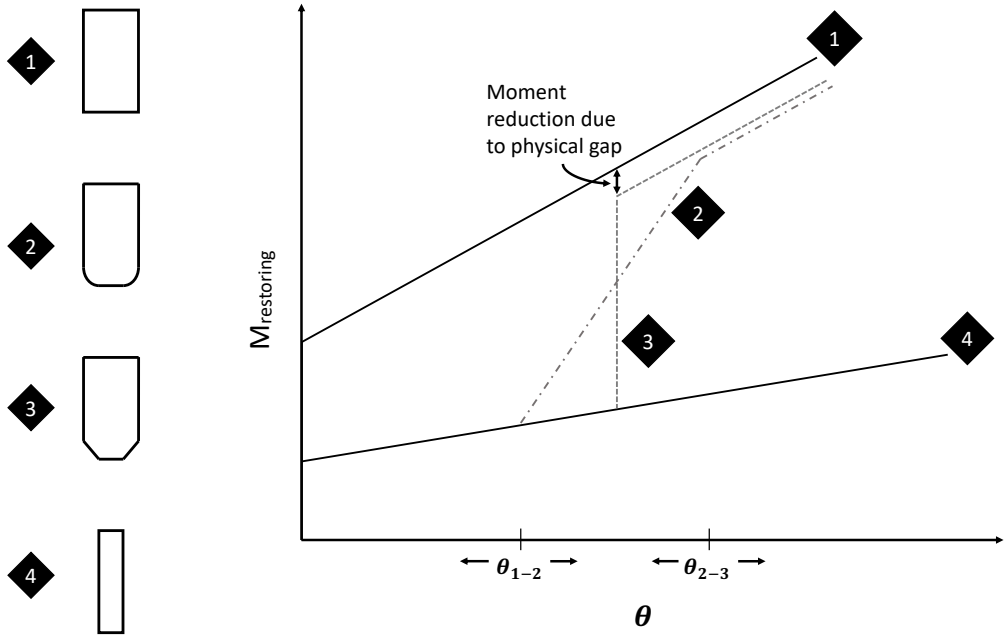

Figure 2.15: Comparison of curved-base rocking walls and rectangular walls with varying widths. The gap is caused by the changes in the vertical displacement of the PT attachment point.

Curved-base rocking walls have been shown to be tailorable, hence may achieve multiple performance objectives.

2.4.3 Amplitude-frequency response

Using the design from CBRW 1, the undamped-unforced closed-form amplitude dependent resonance frequency and the amplitude-frequency response under harmonic excitation are discussed in this section. The resonance periods, T, are obtained using Eq. (2.27d) that is derived from the approximate governing equation with I_{inst} from Eq. (2.24a). The following

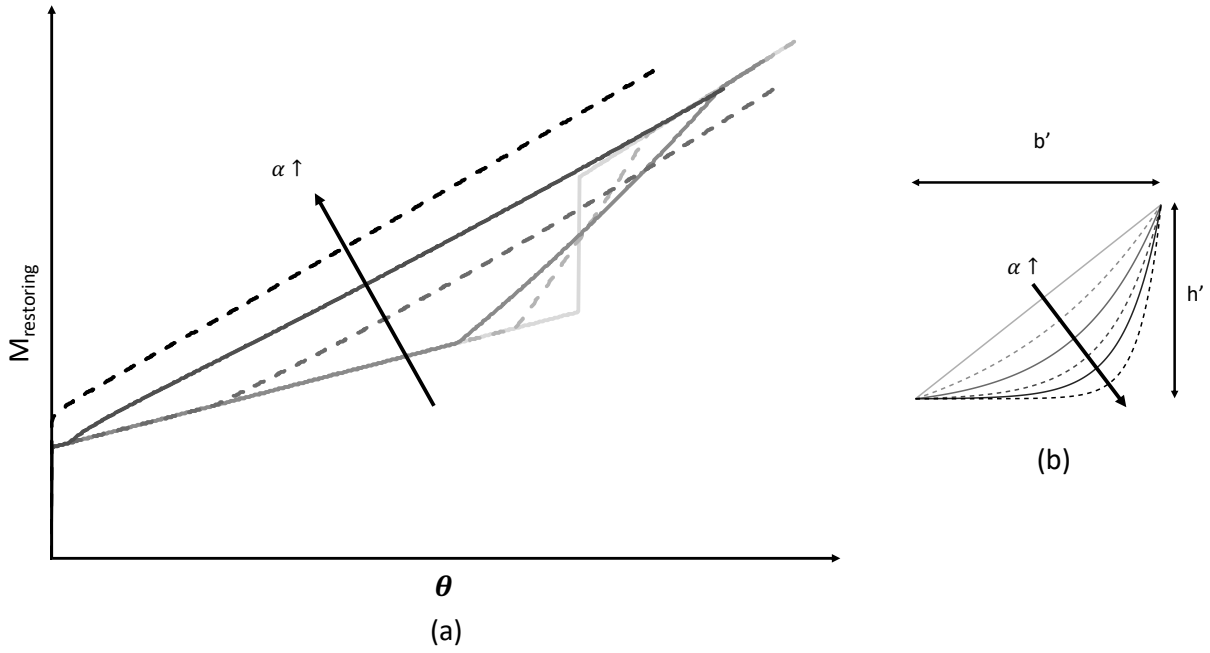

Figure 2.16: (a) Pushover trend with varying α, (b) curved base geometry with varying α.

shows the derivation of Eq. (2.27d).

$$I_{inst}\ddot{\theta} + M_{restoring} = 0, \qquad \ddot{\theta} = \frac{d\theta}{dt}\frac{d\dot{\theta}}{d\theta} \tag{2.27a}$$

$$\int_{\dot{\theta}(\theta_{max})}^{\dot{\theta}(\theta)} \frac{ds}{dt}\, d\dot{s} = \int_{\theta_{max}}^{\theta} -\frac{M_{restoring}}{I_{inst}}\, ds \tag{2.27b}$$

$$\frac{1}{2}\left(\frac{d\theta}{dt}\right)^2 = \int_{\theta_{max}}^{\theta} -\frac{M_{restoring}}{I_{inst}}\, ds = \hat{G}(\theta) \tag{2.27c}$$

$$\frac{T}{4} = \int_{\theta_{max}}^{0} \frac{1}{\omega(\theta)}\, d\theta, \qquad \omega(\theta) = \frac{d\theta}{dt} = \sqrt{2\hat{G}(\theta)} \tag{2.27d}$$

The forced amplitude-frequency curve was obtained by running nonlinear time-history analyses using Eq. (2.23) and simulating $\ddot{u}_g$ as a harmonic excitation with varying forcing frequencies and amplitudes. An assumed coefficient of restitution ($r = 0.90$) was used for this demonstration. Equation (2.26) gives $r = 0.998$ which would be the case in a perfect

system without any additional damping, however, imperfections and friction would likely decrease the coefficient of restitution to a lower value. The value of 0.9 is consistent with work in [Dimitrakopoulos and DeJong, 2012]. Many of the large amplitude responses were aperiodic and hence the peak-to-peak response amplitude is difficult to define. Thus, the response amplitudes were obtained by calculating the root-mean square of the steady-state response of θ.

Figure 2.17 shows the results a suite of (response) amplitude-frequency curves for various forcing amplitudes. Also superposed on the data is the undamped-unforced closed-form resonance frequency results (thick black curve) also plotted with root-mean square amplitude. Similar to classical results observed in hardening and softening Duffing Oscillators, the peak response amplitude follows the same trend as the resonance frequency. As the forcing level increases, the peak shifts left. Unlike the classical case, the rocking system diverges to an infinite resonance frequency as the response amplitude shrinks to zero (i.e., the linearized resonant frequency is infinite), as was also shown by Housner for free-standing blocks [Housner, 1963]. Note the divergence does not occur in a flexible wall and the resonance period approaches the resonant period of a fixed-base cantilever wall, as will be shown in Chapter 3. The resonance frequency exhibits significant sensitivity for low response amplitudes, while being less sensitive to amplitude changes for response amplitudes above approximately 0.05 radians. Practical drift limits for structural and non-structural systems would correspond to approximately 0.05 radians (5 percent drift), thus it is possible the sensitivity could be exploited to avoid resonance under seismic events. Figure 2.17 shows amplitudes above 0.05 radians to show dynamical behavior and trends that maybe of interest to devices that are not limited in drift such as tuned mass dampers.

Note that given the appearance of a softening resonance curve, the right (upper) branch is disconnected from the left (lower) branch. A full analysis, including of potentially unstable response would be needed to complete the full amplitude-frequency curve. Note that this is done in the study in Chapter 3.

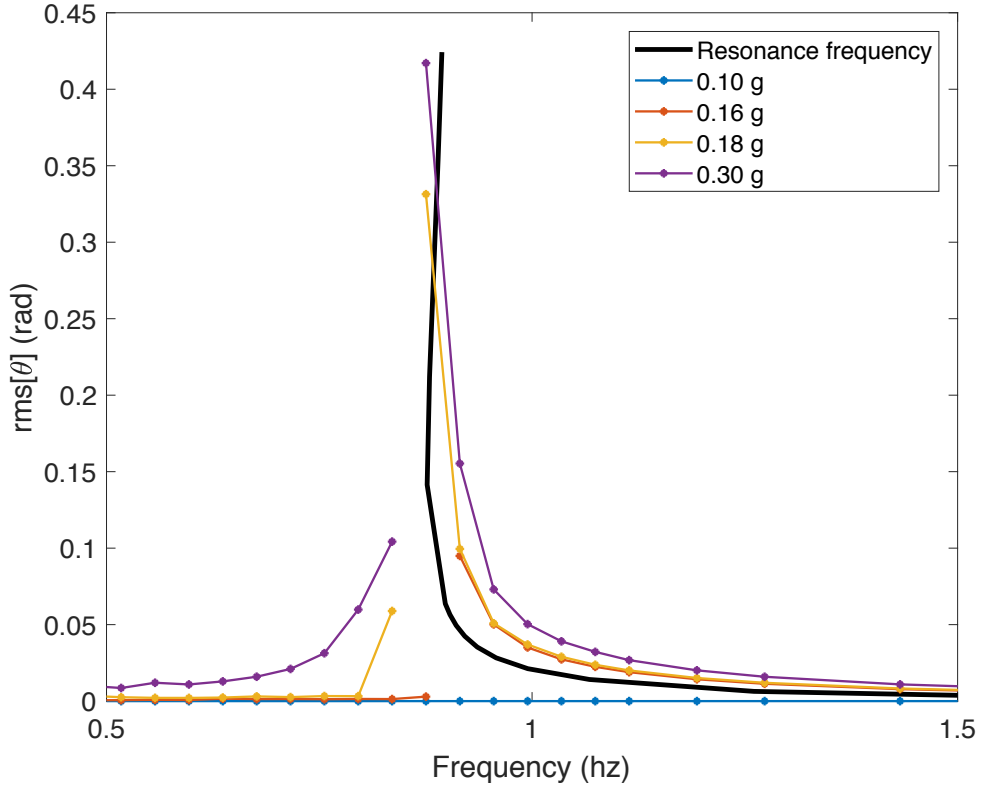

Figure 2.17: Resonance frequency and forced amplitude-frequency response; θ is the steady state response.

2.5 Chapter conclusions

Post-tensioned rocking wall systems — having self-centering capabilities, gap-opening mechanisms limiting primary structure damage, and energy dissipating devices — are very attractive lateral resisting systems that have been shown to be resilient to seismic events. On the other hand, toe crushing and yielding/rupturing of the post-tensioning remain a concern for both concrete and timber walls. The concept of CBRWs was introduced as their geometry can reduce stress concentration, provide confinement to mitigate toe crushing, add more design parameters to tailor the static and dynamics behavior, and increase the drift at which PT yielding/rupturing occurs. The curved base modification is an additional design tool that can be used to achieve other performance goals. The analytical methodology

introduced in this chapter could also be used to represent CBRWs and to assess post-toe crushing strength/stiffness degradation in rectangular rocking walls. The equations formulated provide a way to explore each term of the equation of motion. It was shown that for CBRWs, a gyroscopic term capturing rotation-translation coupling is present in the equation of motion that is otherwise absent in rectangular walls. The gyroscopic term was found to be negligible for the parameters chosen in this study (see Appendix B). Furthermore, the analytical equations served as a way to validate the FE model with curved base. For the diaphragm and wall connection (pin and vertical slot), it was shown that the displacement position of the gravity frame is fairly complex for both rectangular and CBRWs.

Pushover analyses were performed using analytical equation showing that CBRWs can improve the drift at PT yield, which extends to drift at PT rupture. It was shown that CBRWs exhibit three stages of rocking, allowing the pushover response to be highly customizable compared to the rectangle rocking wall. The tailorability of the CBRW system allows for varying stiffness; for example, there could be no rocking under wind loads, rock under stage 1 for service-level and design basis earthquake and rock under stage 2 for maximum considered earthquake. Base-ground impact damage is another issue that would be exacerbated with heavy walls and rocking walls used in floor isolation systems. The reduction in kinetic energy equation [Housner, 1963] was modified to include the gravity system. It was shown that a CBRW with decreasing $\overline{b}$ would reduce impact effects; $\overline{b} = 0$ would cancel out impact damping/damage altogether.

Another application of CBRWs, instead of rounding off the corner, is to widen a narrow rectangular wall and then modify the base to obtain a curved base. Note that this approach is explored in Chapter 4. By doing so, the linear elastic stiffness (prior to rocking, i.e. cantilever wall) and M_{dec} increase and can contribute to resisting wind loading — wind loads are designed for such that M_{dec} exceeds expected wind loads allowing the rocking wall to essentially behave as a cantilever wall. Increasing b' would decrease the decompression moment and the linear elastic stiffness.

Pushover backbone curves and amplitude-frequency response curves were shown but more

work is need to understand how CBRWs could be best used in a structure. Further work is needed to quantify the improvements on stress concentration at the toe and to implement a design procedure that would ensure it is within acceptable limits. Stress concentration could also be an issue at the PT attachment point that can lead to damage to the wall and loss in PT force from PT bar relaxation, which may be addressed by using a stiff steel assembly to distribute the concentrated PT loads over a large area [Ganey et al., 2017].

Other limit states — e.g. failure of frame-to-wall connection, failure of non-structural elements — are also equally as important and needs to be investigated in order to fully develop rocking walls as a viable lateral force resisting system.

A study to understand the effects of BMRWs (specifically with a tapered base) on story drift and acceleration on a system with energy dissipation components under various ground motions will be shown later in Chapter 4. However, work needs to be done to understand CBRWs (and associated horizontal translation from stage 2 rocking) effects on dissipation devices such as TCY and UFP. If the curved base parameters are designed such that the horizontal translation are small, then energy dissipation devices that are often used in concert with rectangular walls can also be applied for CBRWs.

This study was qualitative in nature, as the rigid wall and gravity frame assumption limits the quantitative accuracy of the analysis. Work discussed in Chapters 3 and 4 focuses on generalizing the model with deformable elements and contact properties that can capture material nonlinearity (especially important when investigating base damage from excessive compression).

Though an increase in stiffness and strength could be achieved by simply using more PT or a wider wall, the benefit of CBRWs is the additional tools to achieve performance objectives under different seismic levels. The manufacturing process of CBRWs is beyond the scope of this chapter but is very important and needs to be addressed in later studies.

Chapter 3

NONLINEAR DYNAMICS OF FLEXIBLE POST-TENSIONED ROCKING WALLS

Note: Part of this chapter is a reproduction of [Lin et al., Forthcoming 2022]

The previous chapter looked at the effects of a curved base on a rigid wall using analytical equations formulated with the Lagrange equation. This chapter explores the interaction of rocking and wall deformation, specifically: (1) the transition from fixed-base vibration to predominately rocking, and (2) the nonlinear normal modes and the amplitude-frequency curves.

This chapter first discusses the flexible rocking wall model and its assumptions. Then the derivations of the equations of motion are shown followed by discussions on the impact model (i.e., the post-impact velocities), rocking initiation/cessation, and structural damping. Thereafter, the analytical model is validated against two benchmark cases: (1) a finite element model, and (2) test data from [Acikgoz and DeJong, 2016]. Finally, a brief explanation of nonlinear normal modes is given followed by the unforced/forced dynamic results, which show the nonlinear normal modes and transition from fixed-base vibration to rocking.

3.1 Chapter introduction

3.1.1 Motivation

Extensive studies have been done on Post-Tensioned (PT) rocking systems which aim to improve seismic resilience by increasing the damage-free deformation of the primary load path, and isolating damage to supplemental energy dissipation devices. For buildings, rocking systems usually consist of: (1) a rocking structure, which may be a wall or a frame and

is designed to remain elastic, (2) post-tensioning elements, (3) energy dissipation devices which are to be easily replaceable and leverage the large local deformations to dissipate energy, and (4) diaphragm-to-wall connections. A diagram of a rocking wall system is shown in Fig. 3.1. The studies on PT rocking systems have been generally based on finite element (FE) modeling and experiments to capture system level and component behavior, as rocking systems are fairly complex due to: (1) base-foundation stress concentrations and damage; (2) rocking wall flexibility; (3) inelastic energy dissipation due to impact; (4) the geometrically nonlinear and non-smooth behavior of rocking systems; and (5) the energy dissipation devices and connections mentioned above. Computational models are essential for providing quantitative predictions of the behavior of the rocking system and component behaviors, however analytical expressions for natural frequencies are a vital tool for providing qualitative insight. Analytical work modelling PT rocking systems are generally done by idealizing the structures as rigid, and as a result, are limited in understanding of the interaction between the wall vibration and rocking. There have also been recent analytical studies on flexible rocking structures, although without post-tensioning, for seismic isolation purposes. This study seeks to fill this gap and bring further insight to the general rocking phenomenon, in particular, the interaction of rocking and wall deformation, and the transition between fixed-base vibration and rocking using the nonlinear normal mode (NNM) framework, discussed later. For an in-depth literature review on free-standing rigid rocking blocks, PT rocking systems, and NNMs, see Section 1.3.

3.1.2 Contents

The following section discusses the analytical model used in this study to simulate rocking and wall deformation/vibration. Thereafter, discussions on two benchmark cases, which compare a numerical model and experimental data against that of this chapter, are given. The two benchmark cases/models are: (i) an FE model of a conceptual structure modeled using OpenSees [McKenna, 1997], and (ii) experimental data from the literature on free-standing rocking system from [Acikgoz and DeJong, 2016]. Lastly, the results from forced

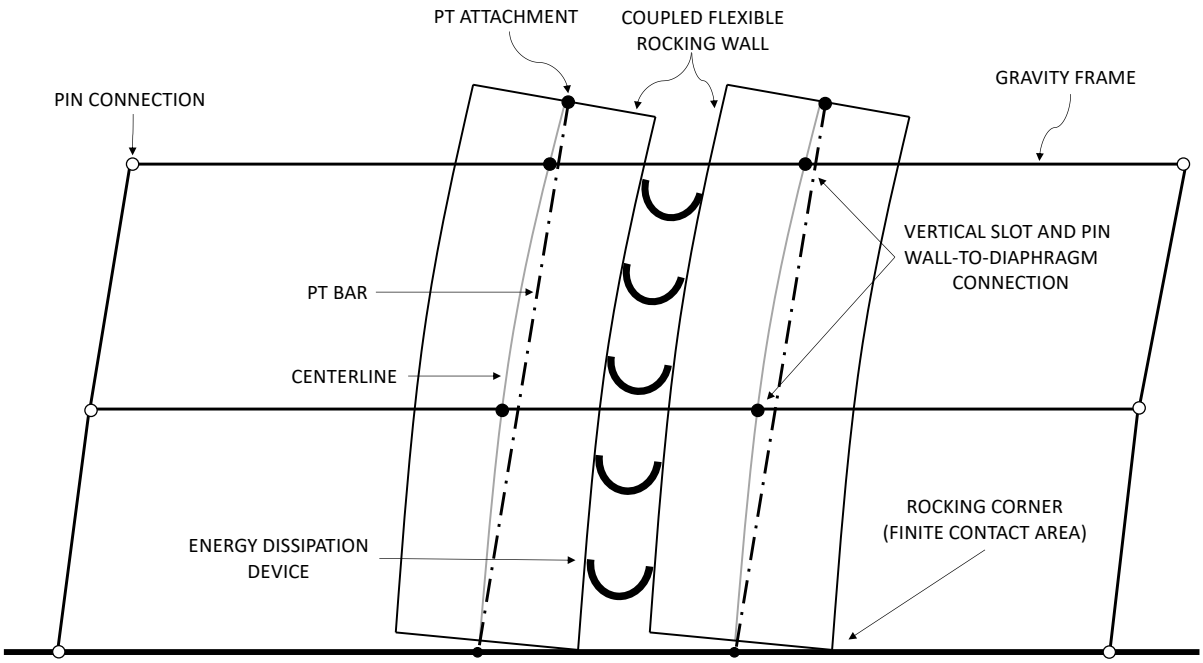

Figure 3.1: Diagram of the rocking wall and gravity system.

and unforced vibration and findings pertinent to earthquake/wind engineering are shown.

3.2 Simplified analytical model for flexible rocking structures

The analytical model used herein approximates real-world rocking walls that generally include shear and bending deformable walls, potential crushing at the rocking interface, localized energy dissipation devices, localized masses (e.g., building floors) and distributed masses (the wall itself), etc. The approximations/simplifications that are used allows for qualitative characterization of the fundamental interaction between the rocking and (usually dominant) first-mode (i.e., mode-1) wall deformation, and serves as a starting point toward the investigation of higher mode effects. The analytical model of the flexible rocking body is also an extension of the analytical model of the rigid rocking body used in Chapter 2. The following subsections will discuss the model assumptions/parameters, kinematics and derivation of the equations of motion, impact model, and rocking initiation/cessation criteria.

3.2.1 Assumptions and analytical model parameters

To investigate the fundamental interaction between the rocking action and wall deformation, a simplified model is composed of the following:

1. Perfectly elastic post-tensioning steel elements.
2. Rigid base and foundation.
3. Inelastic impact assumption, i.e., no sliding or bouncing at impact.
4. Lumped masses that approximates the inertia.
5. Single shear spring between the lumped masses that models the wall flexibility.

Note that the single shear spring approximation (idealization 5) is the primary departure from classical rocking blocks that is explored herein, and more complex wall vs. gravity frame inertial coupling is outside the scope of this work.

The analytical model, parameters, and coordinate system are shown in Fig. 3.2, where h, h_1, and h_2 are the height of the wall, and heights to m_1 and m_2, respectively; b is the base width; k_p is the axial stiffness of the post-tensioning element; k_x is the lateral stiffness of the wall; and $\ddot{u}_g$ is the horizontal ground motion acceleration. The dots above the variable denotes differentiation with respect to time t. The generalized coordinates θ and x are the rigid body rotation (i.e., gap opening angle) and elastic lateral displacement of the wall, respectively. The lateral stiffness of the wall is idealized as $k_x = 3EI/h^3$, where E and I are the modulus of elasticity of the wall and the moment of inertia of the section, respectively. There are additional ways to calibrate the lateral stiffness of the wall (e.g., using second-order beam theory), however, the study is qualitative and as such calibration of the lateral stiffness is beyond the scope of this chapter. Note that the axial stiffness of the wall is ideally rigid. Base deformation/damage is explored later in Chapter 4.

3.2.2 Free dynamics

The equations of motion under free dynamics — i.e., the motion between impacts — are derived using the kinematic relationships between the generalized coordinates (θ and x) and

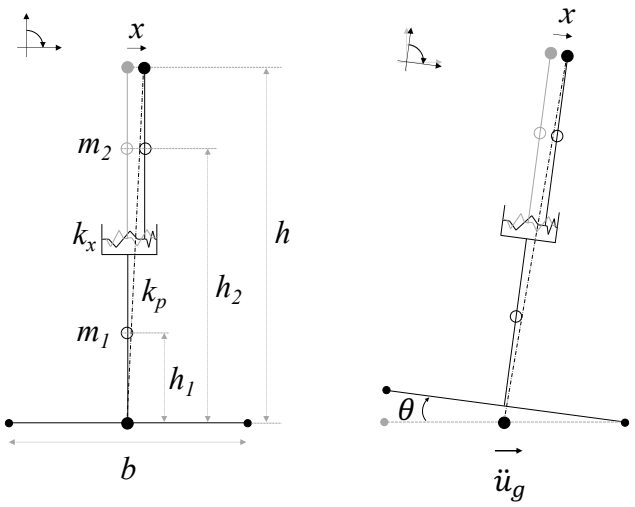

Figure 3.2: Diagrams of the model of a flexible PT rocking wall showing the rigid body rotation θ, wall deformation x, lateral spring, lumped masses, and post-tensioning element.

the positions of the lumped masses and elongation of the springs; given in the following equations:

$$u_p = x\cos\theta + h\sin\theta \pm b/2(1-\cos\theta) \tag{3.1}$$

$$v_p = -x\sin\theta + h\cos\theta \pm b/2\sin\theta \tag{3.2}$$

$$u_1 = \pm b/2(1-\cos\theta) + h_1\sin\theta \tag{3.3}$$

$$v_1 = \pm b/2\sin\theta + h_1\cos\theta \tag{3.4}$$

$$u_2 = x\cos\theta \pm b/2(1-\cos\theta) + h_2\sin\theta \tag{3.5}$$

$$v_2 = -x\sin\theta \pm b/2\sin\theta + h_2\cos\theta \tag{3.6}$$

where u_p and v_p are the horizontal and vertical positions of the end of the post-tensioning element with respect to the left (or right) rocking corner (note, that these are coordinates, not displacements). Similarly, the subscripts 1 and 2 denote the positions of the lumped masses m_1 and m_2. The upper sign (in the plus-minus or minus-plus sign) is used when rocking

about the right corner (positive θ), and similarly, the lower sign is used when rocking about the left corner (negative θ). Note, the rotational inertia is ignored, i.e., this is a lumped mass model.

The equations of motion are derived using a Lagrangian approach specific to systems of lumped masses. The equation of motion using the Lagrangian approach can be commonly represented as:

$$\frac{d}{dt}\left(\frac{\partial T}{\partial \dot{q}_i}\right) - \frac{\partial T}{\partial q_i} + \frac{\partial \Pi}{\partial q_i} = 0 \tag{3.7}$$

where T, q_i, and Π symbolizes the kinetic energy, the generalized coordinates, and potential energy, respectively. And,

$$\Pi = \frac{1}{2}k_p\Delta_p^2 + \frac{1}{2}k_x x^2 + \sum_{n=1}^{N} m_n v_n g \tag{3.8}$$

$$\Delta_p = \sqrt{u_p^2 + v_p^2} - L_o \tag{3.9}$$

where g, Δ_p, L_o, and N are the acceleration due to gravity, post-tensioning element elongation, initial unstressed post-tensioning element length, and the number of lumped masses, respectively. Note that the equations of motion are for conservative systems. The Lagrangian approach specific to systems of lumped masses simplifies the kinetic energy as seen in the following equivalent equations, and therefore are included explicitly [Wiebe and Harvey, 2019]:

$$(\mathbf{M}^u + \mathbf{M}^v + \mathbf{M}^\theta) \cdot \ddot{\mathbf{q}} + \dot{\mathbf{q}} \cdot (\mathbf{G}^u + \mathbf{G}^v + \mathbf{G}^\theta) \cdot \dot{\mathbf{q}} + (\mathbf{F}_{\mathrm{g}}^u)\ddot{u}_{\mathrm{g}} + \nabla\Pi = 0 \tag{3.10}$$

where $\mathbf{M}$, $\mathbf{G}$, and $\mathbf{F}_{\mathrm{g}}^u$ are matrices, third-order tensors, and vectors, respectively; the superscript u, v, and θ indicate the horizontal, vertical, and rotation degrees-of-freedom. Equation (3.10) is solved numerically using the classic Runge–Kutta method. For the static case, Eq. (3.10) collapses to the theorem of minimum potential energy with the pushover horizontal force applied to the center top of the wall (i.e., the connection point of the post-tensioning element and the wall). The force can be solved in terms of θ and x and the results are

discussed later in the benchmark case. The expressions for the $\mathbf{M}$, $\mathbf{G}$, and $\mathbf{F}_{\mathrm{g}}^{u}$ terms for the horizontal degree-of-freedom are:

$$[\mathbf{M}^{u}]_{ij} = \sum_{n=1}^{N} m_n \frac{\partial u_n}{\partial q_j} \frac{\partial u_n}{\partial q_i} \tag{3.11}$$

$$[\mathbf{G}_{i}^{u}]_{jk} = \sum_{n=1}^{N} m_n \frac{\partial^2 u_n}{\partial q_j \partial q_k} \frac{\partial u_n}{\partial q_i} \tag{3.12}$$

$$\{\mathbf{F}_{g}^{u}\}_{i} = \sum_{n=1}^{N} m_n \frac{\partial u_n}{\partial q_i} \tag{3.13}$$

where the component $[\mathbf{M}^{u}]_{ij}$ is the ith row, jth column of the square symmetric mass matrix $\mathbf{M}^{u}$; $[\mathbf{G}_{i}^{u}]_{jk}$ is the jth row, kth column of the square symmetric matrix $\mathbf{G}_{i}^{u}$; and the scaler $\{\mathbf{F}_{g}^{u}\}_{i}$ is the ith component of the ground motion-induced force-pattern vector $\mathbf{F}_{g}^{u}$. The reader is referred to [Wiebe and Harvey, 2019] for further details on the derivation of Eq. (3.10) and its included terms. The significance of the Lagrangian approach specific to systems of lumped masses is that the kinetic energy terms can be explicitly obtained through the partial derivatives of the kinematic equations, see Eqs. (3.1) to (3.6), without the need to explicitly derive the kinetic energy and its spatial and temporal derivatives. The reader is referred to Chapter 2 for the formulation of the governing equation for a rigid PT rocking wall using a classical Lagrangian approach.

3.2.3 Impact damping model

Rocking is generally treated as an inelastic impact (i.e., no bouncing or sliding), and thus the energy loss at each impact is needed to accurately predict the dynamic response of the system. Housner used the conservation of angular momentum to calculate the post-impact angular velocity (and thus the energy dissipated at impact) of a rigid rocking block [Housner, 1963]. Lin et al. extended the equation to a rigid PT rocking wall connected to a gravity frame [Lin et al., 2019]. Generalizing the rocking system to include a flexible wall requires additional degrees-of-freedom, and as such, conservation of angular momentum no longer suffices to

compute the post-impact angular velocity. However, idealization 5 in Section 3.2.1 implies that m_2 can only slide frictionlessly relative to m_1, and consequently with $\theta = 0$ at impact, the following holds true from conservation of linear momentum of the top mass m_2:

$$\dot{u}_2^+ = \dot{u}_2^- \tag{3.14}$$

where the superscripts $-$ and $+$ symbolizes the pre-impact and post-impact state. Acikgoz and DeJong used similar principles for the impact model, however with translational velocity $\dot{x}$ remaining the same — i.e., using Eq. (3.15) in lieu of Eq. (3.14). Equations (3.14) and (3.15) are explored later in the benchmark section.

$$\dot{x}^+ = \dot{x}^- \tag{3.15}$$

Note that the symbols for horizontal/translational velocities in the present chapter and in [Acikgoz and DeJong, 2016] are different. Furthermore, the two different assumptions result in quantitative, but not qualitative differences in the results for the case studies used herein. The equation from conservation of angular momentum is adopted from [Housner, 1963] — capturing the angular momentum of m_1 — with the addition of the angular momentum of m_2, see Eqs. (3.16) and (3.19). Note that this conservation of momentum rule relies on the assumption that the rocking impact occurs only at the exterior corners, and hence curved/tapered/deformable bases affect this.

$$I_1\dot{\theta}^+ + L_2^+ = I_1\dot{\theta}^- - \frac{1}{2}m_1b^2\dot{\theta}^- + L_2^- \tag{3.16}$$

$$L_2^\pm = m_2(r_{2v}^+\dot{u}_2^\pm - r_{2u}^+\dot{v}_2^\pm) \tag{3.17}$$

$$\dot{u}_2^\pm = r_{2v}^\pm\dot{\theta}^\pm + \dot{x}^\pm \tag{3.18}$$

$$\dot{v}_2^\pm = r_{2u}^\pm\dot{\theta}^\pm \tag{3.19}$$

where I_1 is the moment of inertia of m_1 about the center of rotation, L_2 is the angular momentum of m_2, and r_{2v} and r_{2u} are the vertical and horizontal position vector of m_2 with respect to the center of rotation. Using Eqs. (3.14) and (3.16), the post-impact velocities, $\dot{\theta}^+$ and $\dot{x}^+$, can be solved; alternatively, Eq. (3.15) can be used instead of Eq. (3.14).

This modeling approach captures the fact that the impact at the base does not instantaneously travel up the height of the wall. Rather, it travels as a wave up. While this model uses only a single spring to capture the mode-1 response, further discretization would allow for the capture of the wave dynamics of a flexible wall. This is contrasted with the vertical impulse that is applied to both blocks, which are assumed to be vertically rigid. This vertical impulse results in a sudden change of vertical velocity. Likewise using compressive vertical springs would lead to vertical wave propagation phenomenon, but that is assumed to be much faster than the horizontal wave speed and hence assumed rigid (which simplifies the model greatly).

3.2.4 Rocking initiation/cessation

The criteria for initiation and cessation of rocking — important for both unforced dynamic response and forced dynamic response as it captures the time at which the state of second mass and forcing will cause uplift — is discussed here. Prior to the initiation of rocking $\theta = 0$ and m_2 vibrates as a fixed-base cantilever according to the the equation of motion:

$$m_2\ddot{x} + c_x\dot{x} + \left.\frac{\partial \Pi}{\partial x}\right|_{\theta=0} = -m_2\ddot{u}_g \tag{3.20}$$

The potential energy term is nonlinear due to the post-tensioning element, however, is close to linear ($k_x x$) for small deformations (gradually growing, with deformation, hardening spring effect due to the post-tensioning element). Note that θ and its time derivatives remain zero prior to rocking initiation.

The rocking initiation is determined using the dynamic moment and vertical force equilibrium shown in Fig. 3.3. Note the model assumes the base reaction forces, C_L and C_R,

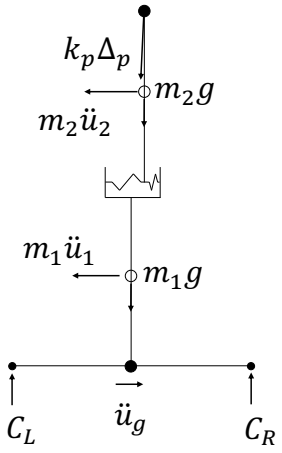

Figure 3.3: Free-body diagram to determine base vertical reaction force.

are concentrated at the left and right corner of the wall (which, as mentioned earlier, is also assumed for rocking). If either force is zero or negative (indicating an impossible tension force), then rocking initiates and the system vibrates according to Eq. (3.10). Due to sensitivity to initial conditions, the time and state at uplift is necessary to accurately simulate the dynamic response, however note, sensitivity may lead to large quantitative differences at time t, but unlikely to lead to differences in the peak or average amplitudes. Time steps are small enough such that if a negative force is found, it will be small, and it is assumed that rocking initiates on the next time step. This could be fine tuned with event finding procedures, but that was not undertaken in the simulation.

The rocking cessation condition is more complicated, and hence, is first illustrated with a rigid wall and a single lumped mass immediately prior to impact in Fig. 3.4 (left). Using conservation of angular moment about the left corner o' and zero tension capacity of rigid rocking walls, it can be seen that the rigid rocking wall cannot stop rocking abruptly (i.e., θ may only approach zero asymptotically), also shown in [Housner, 1963]. The flexible wall is more interesting as rocking cessation does not necessarily contradict the conservation of

angular moment and zero tension capacity. From Fig. 3.4 (right), pre-impact angular moment about o' is:

$$L^- = m_1 \mathbf{r}_1^+ \times (\mathbf{r}_1^- \times \dot{\theta}^-) + m_2(\mathbf{r}_{2u}^+ \times \dot{\mathbf{v}}_2^- + \mathbf{r}_{2v}^+ \times \dot{\mathbf{u}}_2) \tag{3.21}$$

where $\times$ denotes the vector product operation. Assuming rocking stops, $\dot{\theta}^+ = 0$, the post-impact angular moment is thus $m_2 \mathbf{r}_{2v}^+ \times \dot{\mathbf{u}}_2$. Note that $\dot{\mathbf{u}}_2$ right after impact is unchanged as per Eq. (3.14). Thus the conservation of angular momentum and zero tension capacity are satisfied if the following holds true:

$$m_1 \mathbf{r}_1^+ \times (\mathbf{r}_1^- \times \dot{\theta}^-) + m_2 \mathbf{r}_{2u}^+ \times \dot{\mathbf{v}}_2^- \leq 0 \tag{3.22}$$

as it would allow a compressive impulse at point o. However, the previous equations are not sufficient to predict if rocking will stop; it showed, unlike rigid walls, conservation of angular moment and zero tension capacity can be satisfied with $\dot{\theta}^+ = 0$. Further investigation is needed to define the exact conditions for rocking cessation, and thus was not implemented in the model explicitly. The model is, nevertheless, able to predict practical ceasing of rocking, as in some scenarios the rocking angles will be very small with displacement dominated by the cantilever deformations. In the forced case, it is possible for the force and upper block deformation and momentum to 'conspire' such that the rock would identically cease rocking at impact. Additionally, if the forcing ceases, the rocking angle asymptotically rings down to zero. This work focuses on steady-state response and hence the stopping conditions are not essential. However, due to sensitivity of initial conditions, it cannot be ruled out that a subset of simulated responses that could have come to rest during a transient response (and perhaps never returned to rocking) are missed. Actually, a freely rocking block will ultimately cease rocking due to: (1) flexible foundation/base introducing friction, finite impact time, and finite impact surface, and (2) sliding and bouncing.

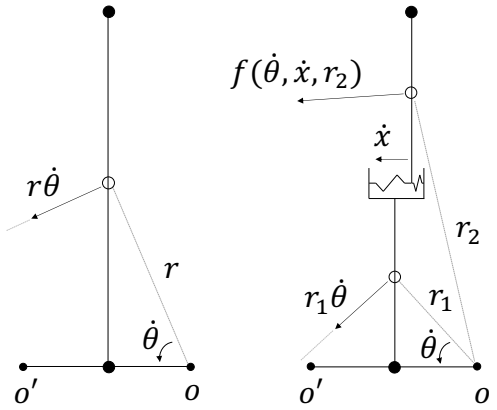

Figure 3.4: Pre-impact velocities for a rigid (left) and flexible rocking wall (right).

3.2.5 Structural damping

As mentioned previously, the equations of motion are formulated for conservative systems (i.e., does not include structural damping ζ_x). Inherent structural damping is incorporated to the equations of motion by inserting a $\mathbf{C}\dot{\mathbf{q}}$ term (which is often identified through modal damping of linearized dynamics, but other methods can also be used), where $\mathbf{C}$ is the two-by-two damping matrix. Structural damping is idealized here to only affect the generalized coordinate x, and therefore:

$$\mathbf{C} = \begin{bmatrix} 0 & 0 \\ 0 & C_d \end{bmatrix} \tag{3.23}$$

where $C_d = 2m_2\omega_x\zeta_x$, and ω_x is the natural frequency (i.e., $\sqrt{k_x/m_2}$). Acikgoz and DeJong similarly modelled structural damping — for a free-standing structure — with Rayleigh damping using the damping factors ζ_{n1} and ζ_{n2}, which denote the prescribed percentage of critical damping for the first and second vibration mode, see [Acikgoz and DeJong, 2016]; note that this is the damping model that would be used if the study here used additional lumped masses to capture higher vibration modes.

3.3 Benchmark cases

This section will explore two benchmark cases to validate the analytical model and provide further insight into the static and dynamic behavior. The two benchmark cases are (i) FE model results, in OpenSees, of a conceptual rocking wall system, and (ii) experimental results from [Acikgoz and DeJong, 2016]. The former is to validate the equations of motion and gain insight into the static and free dynamic behavior of a PT system; the latter is to validate the impact model and compare Eqs. (3.14) and (3.15) in a free-standing system. Note that work done in [Acikgoz and DeJong, 2016] also includes a multi-mass analytical model with different impact models, as mentioned before. The comparisons will be made through pushover curves and nonlinear dynamic time-histories. In order to better quantitatively capture the wall deformation/vibration response, a new non-dimensional generalized coordinate is introduced $d = x/h$. In addition, the roof drift $D = u_p/h$ will be used to look at the total drift demand. For an in-depth discussion on the normalization of the equations of motion, see Appendix C.

3.3.1 Case 1: Pushover and free dynamic response of a PT rocking wall

The benchmark case here focuses on the pushover and free dynamic response of a PT rocking wall. The FE model methodology is mostly identical to that given in Chapter 2 with the primary difference being the use of a lateral spring and an equal rotation constraint (via the *EqualDOF* command in OpenSees) to ensure the top and bottom wall elements have equal rotation, see Fig. 3.2. The reader is referred to Chapter 2 for further details on the FE model. Table 3.1 shows the parameters used in the conceptual rocking system in this subsection, which is roughly based on the test specimen in [Pei et al., 2019]. Furthermore, h_1 and h_2 are one-fourth and three-fourth the height of the wall h, respectively, in order to reflect the tributary wall mass in m_1 and m_2. The rotational inertias, I_1 and I_2, are ignored; the lumped masses approximate the inertia of a real system. In many cases the inertia is dominated by the gravity system and that appears primarily through translation not rotation. A similar

Table 3.1: Relevant parameters used for comparison with the FEM model.

Parameters	Values
h (in)	288
b (in)	60
m_1 (kip/in/s^2)	0.0622
m_2 (kip/in/s^2)	0.0640
k_p (kip/in)	178.0736
k_x (kip/in)	27.9744
L_o (in)	287.7304
E (ksi)	1800
I (in^4)	123750

lumping approach was also used by Moroder et al. [Moroder et al., 2017], however, it should be noted that in this approach the weight of the floors/roof also contribute to the restoring moment. There are many different types of connections — some of which may decouple the inertias from the weights and restoring moments — but complex modeling of the different connections is outside the scope of the chapter, which focuses on qualitative behaviors.

The pushover force P is applied at the top center of the wall where the post-tensioning element is connected. Figure 3.5 shows the plots of the pushover results normalized by the decompression force of the rigid wall denoted by P_O (i.e., the pushover force required for the base to uplift). There is good agreement between the different models, validating the potential energy term in the equations of motion. Moreover, Fig. 3.5 superimposes the pushover response from an equivalent rigid wall (grey). As expected, the pushover with respect to D of the rigid wall is stiffer, however k_x does not significantly impact the response with respect to θ.

Figure 3.6 shows the plots of the free vibration nonlinear time-histories of the analytical and numerical model. Again, there is good agreement between the different models, validating the full (free dynamics) equations of motion. The initial conditions were arbitrarily chosen; note that θ and d do not approach zero at the same time, hence this is not an NNM

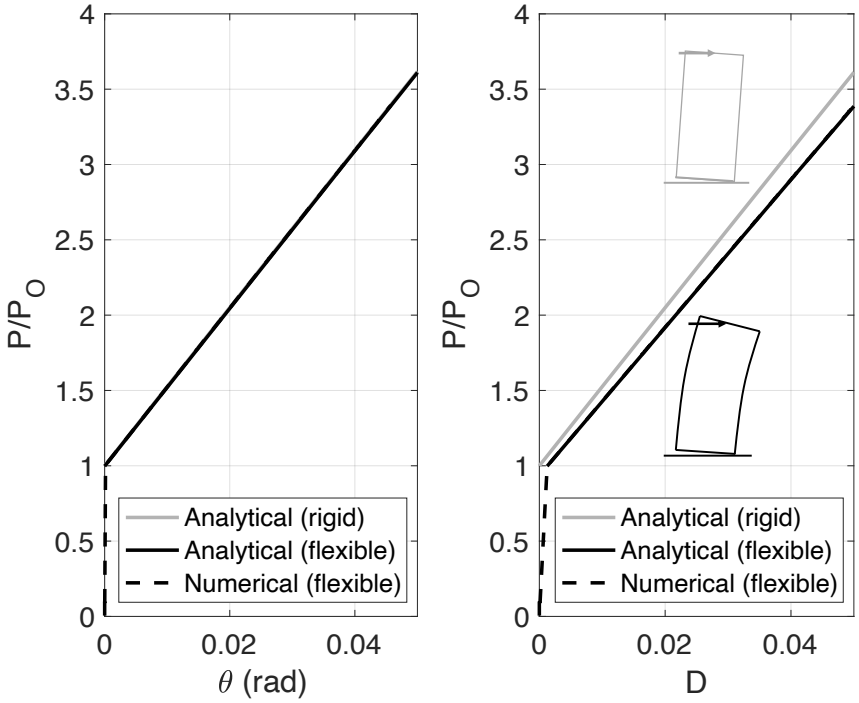

Figure 3.5: Pushover results of the analytical and numerical model. $P_O = 10.0755$ kips

— solving for the NNMs is discussed later. The plots show the highly coupled behavior of the generalized coordinates. For example, d starts to increase due to the large initial value of θ, which effectively puts m_2 at a sharp decline with the lateral spring unable to overcome the weight for the given θ and d. At approximately 0.5 seconds, the increase in spring force and decrease in θ results in d to move back. Furthermore, θ behaves with a much higher nonlinearity than if the system was a rigid wall, again indicating the highly coupled nature of the generalized coordinates.

The simulations stopped at impact because the purpose here is to check the accuracy of the free dynamics equations of motion, not the the impact model. Moreover, the FE model would require calibrated base springs/dampers in order to exactly capture impact damping, which is outside the scope of the study. However, impact damping is evaluated against experimental data in the next subsection.

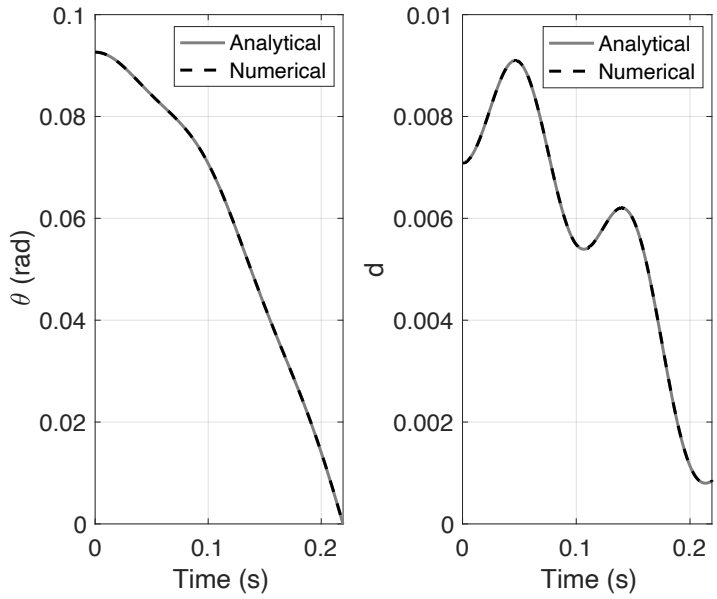

Figure 3.6: Free vibration nonlinear time-history from the analytical and numerical model

3.3.2 Case 2: Dynamic response of a free-standing system

This benchmark case examines the dynamic response with impact and structural damping of a free-standing system by comparing the analytical model — with both Eqs. (3.14) and (3.15) — against test results from [Acikgoz and DeJong, 2016]. The parameters used in this subsection are provided in Table 3.2. The reader is referred to [Acikgoz and DeJong, 2016] for further discussion on the test set up. Due to the model being composed of two masses, the mass of the column (which was small compared to the bottom and top mass) was neglected. Furthermore, the structural damping is not evaluated due to the small ζ_x used in this case.

Figure 3.7 shows a plot comparing the free vibration nonlinear time-histories of the model-s/test with $\theta_o = 0.11$ radians, the subscript o denotes the initial condition. The time-history for d was omitted because it was not available, and thus could not be used to confidently validate the full (free dynamics) equations of motion as shown in the previous case study. As such $d_o = 0$ was chosen for simplicity. The plot shows good agreement between the model with Eq. (3.14) and test result during the first cycle. The model with Eq. (3.15) loses more

Table 3.2: Relevant parameters used for comparison with the experimental data from [Acikgoz and DeJong, 2017].

Parameters	Values
h_1 (m)	0.06
h_2 (m)	1.89
b (m)	0.61
m_1 (kg)	77.3
m_2 (kg)	123.1
I_1 (kg m^2)	10
E (GPa)	200
I (cm^4)	183.3
K_x (kN/m)	162.9
ζ_x (%)	0.0025

rotational velocity after impact, and as such, does not match the test data as close, although this is not a general indication. It is unclear which equation leads to more energy dissipation as it may vary depending on the state (i.e., $\dot{\theta}$, $\dot{d}$, and d) at impact, and the system parameters (e.g., I_1, m_1, h_1, etc.). Furthermore, energy is transferred between rocking and wall vibration during impact. This can be seen after the first impact where it resulted in the small high frequency oscillation of θ; this was also observed in the experimental data (both the small high frequency oscillation of θ, and high frequency acceleration of m_2). The discrepancy between the models and the test results is primarily due to difference in the energy loss at impact. The lower θ amplitude increases frequency and, as a results, the rocking falls out of phase. As mentioned previously, Acikgoz and DeJong matched the experimental results very well by using a multi-mass model with the Eq. (3.15) impact model but similarly found the model to fall out of phase with the experimental data at a later cycle [Acikgoz and DeJong, 2016].

Modelling the experiment using a two-mass system with a single lateral spring was able to reasonably capture the free dynamics but less so the impact damping. The flexible bases

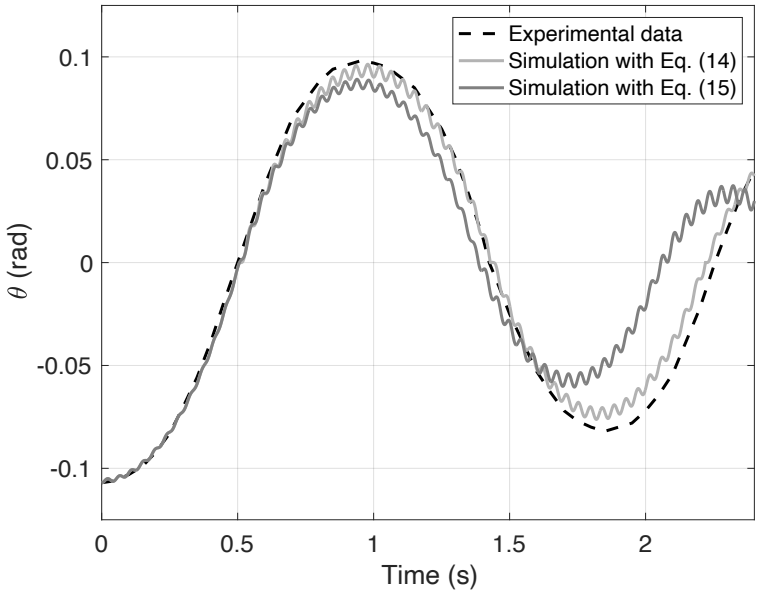

Figure 3.7: Free vibration nonlinear time-history from the analytical models. Solid grey: results from present study; dashed black: results from [Acikgoz and DeJong, 2017].

and foundations from experiments lead to finite impact time, suggesting that the assumption of rigid bases/foundations (i.e., infinitesimal impact time) over-predicts the impact damping of real-life structures. This was shown in [Acikgoz and DeJong, 2016] were the simulation was able to better match test data when they used a impact model with a finite impact time, however with more complex calibration.

3.4 Results of the study of the analytical model

This section discusses the results from the study of the analytical model under unforced and forced vibrations, and important findings. The model in Case 1 is used herein (note that this system is post-tensioned). The unforced vibrations are simulated to obtain the NNMs, discussed in the next subsection. The forced vibration provides insight on the flexible rocking system response to harmonic/pulse-type loading in addition to how the NNMs can qualitatively predict peak demands.

3.4.1 Unforced vibration

The non-smooth and nonlinear nature of rocking problems makes the analytical closed-form solution for the NNMs quite difficult, sometimes with special solutions existing for impulse or periodic forcing, but no closed-form solution for transient responses. Furthermore, the flexible wall increases the complexity. The methodology used instead is to pick varying initial conditions, θ_o and d_o, and run the simulation until an NNM is found. As an example of NNMs, Fig. 3.8 shows a nonlinear spring-mass system and the NNMs shapes, Φ, and respective time-history (unforced vibration); note that the degrees-of-freedom approach zero at the same time. Similarly, an NNM for the flexible rocking wall was found when θ and d exhibited periodic response by simultaneously reaching zero. Due the amplitude-frequency dependence of the rocking system, see [Housner, 1963], both structural and impact damping were omitted. This did not impede the ability of the NNMs to predict damped behavior, discussed later.

Figure 3.9 shows the amplitude-frequency plots of the NNM solutions for the unforced, undamped simulations. The three plots shown are the steady-state peak response for θ, d, and D. Also superimposed on the plot is the NNM (i.e., amplitude-frequency curves) for an equivalent rigid rocking wall obtained analytically, see Chapter 2. Note that the rigid wall is a single degree-of-freedom system, therefore the mode shapes are simply a scale factor of one. The NNM-1 (i.e., first NNM) of the flexible wall (approximately within the 10 to 20 rad/s range) and the rigid wall NNM are similar and converge as amplitude increases. This suggests that the rocking action (i.e., θ) is dominant for NNM-1 at large amplitudes. The NNM-2 of the flexible wall (approximately 60 to 90 rad/s) is also shown in Fig. 3.9. Examples of nonlinear time-history response of NNM-1 and NNM-2 are shown in Fig. 3.10. The left plot (NNM-1) further indicates there is rocking-dominant action at large θ amplitude (approximately 0.01 radians) as d is vibrating at low amplitudes; this is not the case for the right plot (NNM-2) as both show similar large amplitudes of approximately 0.01 radians. Further investigation on the rocking-dominant (i.e., θ dominant) or cantilever-dominant (i.e.,

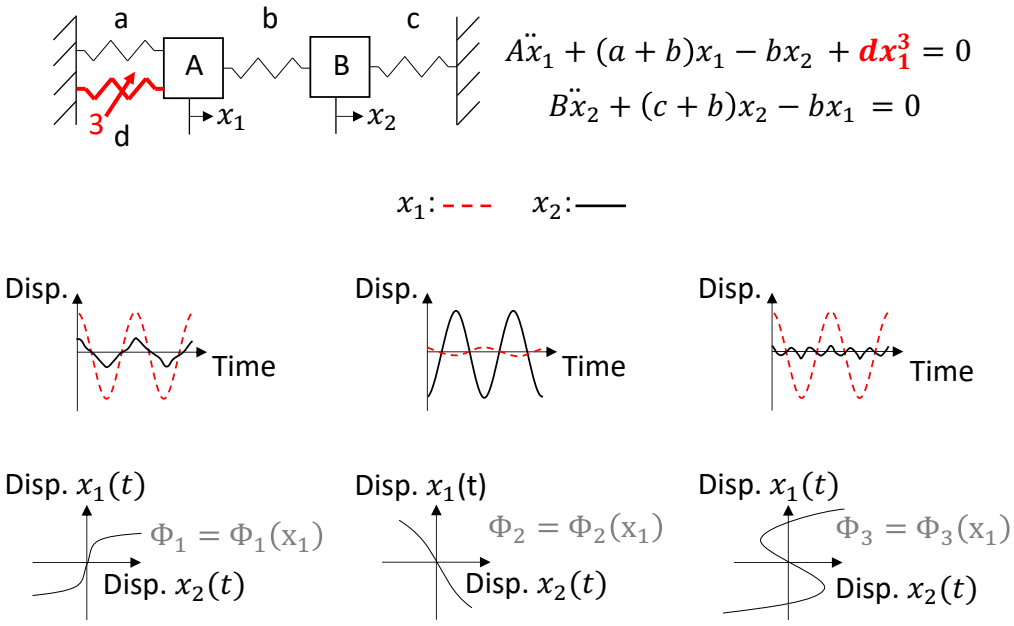

Figure 3.8: Nonlinear normal modes of a spring-mass system

d dominant) action is discussed next. Note that much of NNM research has focused on continuous smooth systems. For nonsmooth systems, it is difficult to be confident that there are not other co-existing responses as well.

The frequency near zero θ amplitude for a rigid rocking wall is widely known to approach infinity, see [Housner, 1963]. Contrarily, the linear natural frequency for a flexible fixed-base structure is finite. For the analytical model introduced, the linear natural frequency is $\omega_x = \sqrt{\frac{K_x}{m_2}}$. In order to bridge the gap, the transition between fixed-base vibration and rocking was investigated by exploring the NNM-1 behavior for both large, and small values of θ, with the former representing rocking and the latter representing the transition. Figure 3.11 shows the nonlinear time-histories of NNM-1 with relatively large amplitude (left) and relatively small amplitude (right), where the latter has a resonant frequency closer to ω_x. As noted before, θ drives the response at large amplitudes. Conversely, d appears to be the primary factor at small amplitudes (i.e., as the resonant frequency approaches ω_x). The plot

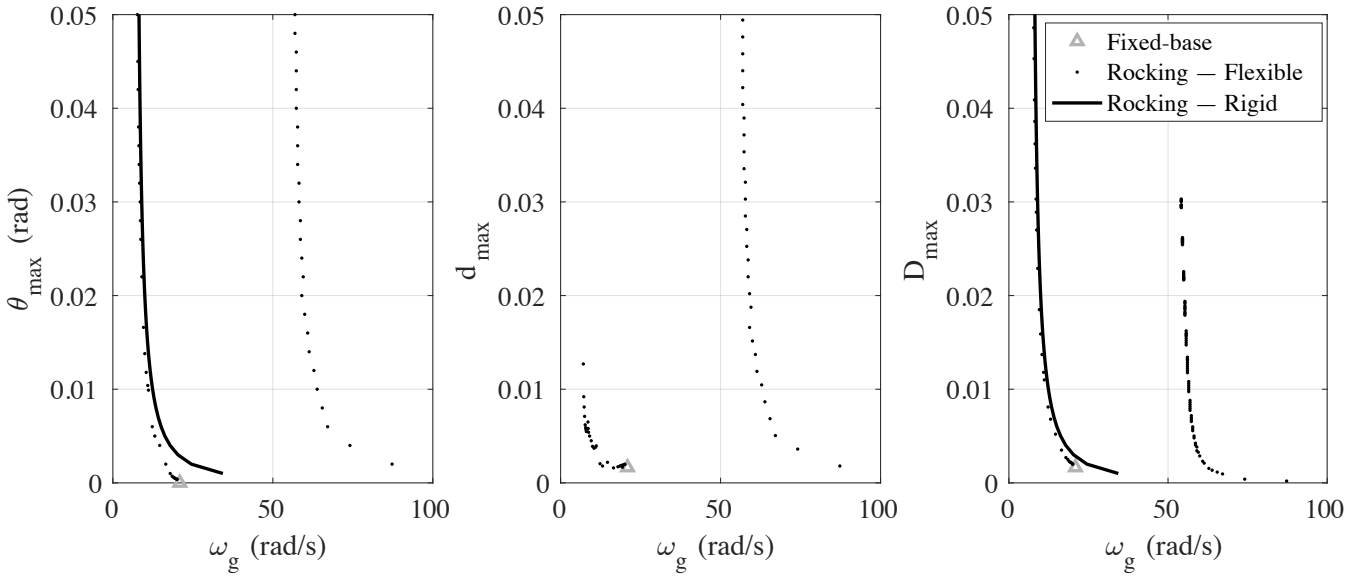

Figure 3.9: Amplitude-frequency plot of the nonlinear normal modes.

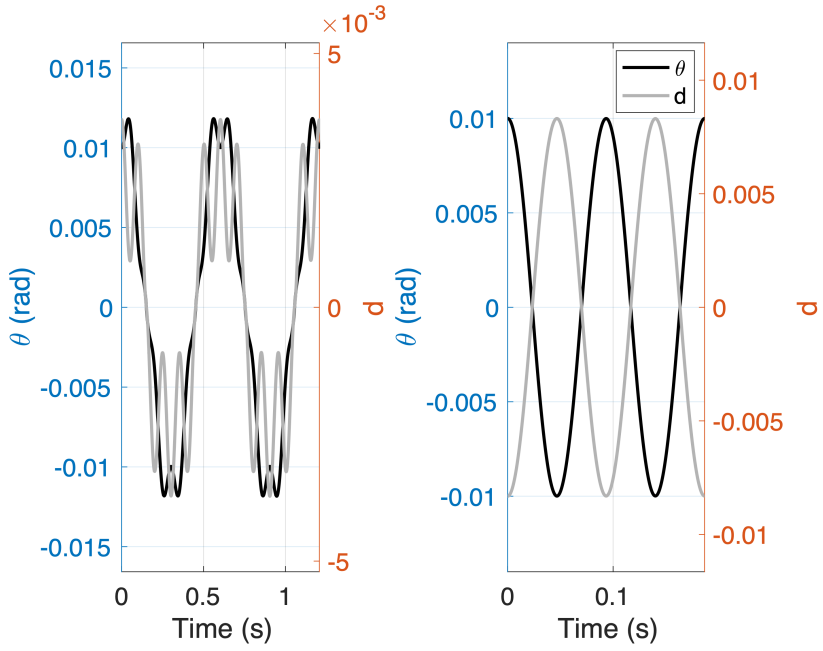

Figure 3.10: Free vibration nonlinear time-history of first (left) and second (right) nonlinear normal modes.

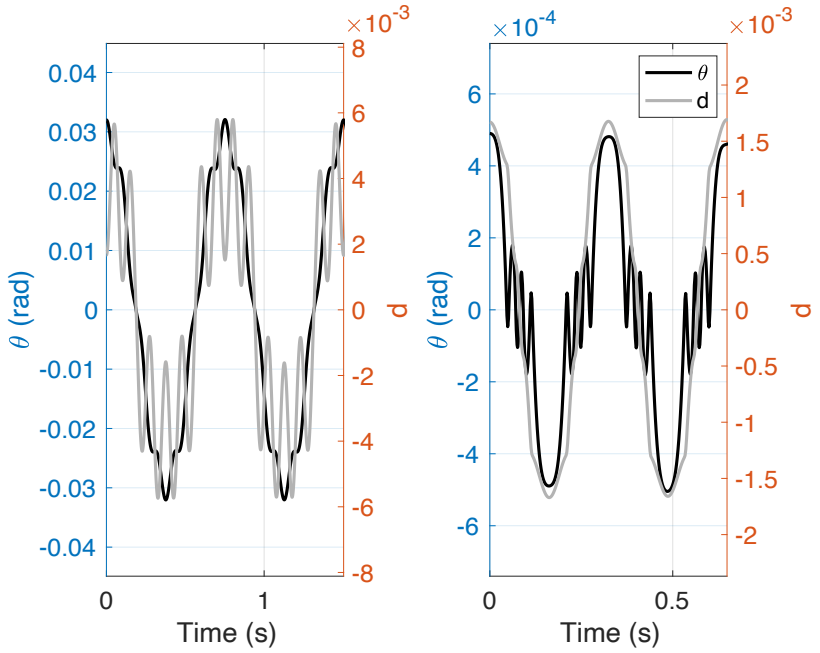

Figure 3.11: Free vibration nonlinear time-history of nonlinear normal modes with small (left) and large (right) θ_o and equal d_o.

of the small amplitude of θ is unintuitive, nonetheless the physical interpretation is that (i) the system is undergoing elastic vibration with small rigid body rotation; (ii) the system exhibits rigid-body 'chattering' behavior as θ approaches zero; and (iii) the system exits the 'chattering' with symmetrical periodic response.

3.4.2 Forced vibration

In linear systems, the natural frequencies provide much information about forced response. To some degree, this is also true for NNMs. This subsection discusses this by looking at the response to harmonic ground motion and how the amplitude-frequency curve compare. The forced vibration in this subsection include both structural (ζ_x at 5 percent) and impact damping, using Eq. 3.14, as discussed previously. In addition, the response to pulse-type loading, co-existing solutions, and phase angle are also discussed.

Harmonic and pulse-type loading

The harmonic loading is varied in both forcing frequency ω_g in rad/s and forcing amplitude (i.e., forcing level) A_g in terms of g. Figure 3.12 shows the forced amplitude-frequency plot of the steady-state response with varying forcing levels. The NNMs are also superimposed on the plot which show good agreement between the NNMs and the peak demands of each forcing level. Similarly, in Fig. 3.12 the steady-state response of an equivalent fixed-base wall, see Eq. (3.20), is compared to that of the rocking wall. This figure illustrates the effects when the wall is allowed to uplift: (i) the resonant frequencies shift left; (ii) the peak demand for each force level changes; and (iii) the skew of the overall shape changes. Note that the convergence of the fixed-base and rocking wall indicates the forcing amplitude and frequency was unable to initiate rocking.

Interestingly, NNM-2 was observed to not coincide with forced-vibration peaks. This is likely because the ground excitation is unable to excite the NNM-2 as the inertial forces are unidirectional (see Fig. 3.10 for a general shape of the second NNM).

The effects observed can help engineers design lateral-force resisting systems that uplift and rock in order to shift the resonant frequency away from the frequency range corresponding to higher energy content from ground motions. The decrease in d when the wall is allowed to uplift also suggests that the bending stress on the wall is reduced; a main objective of the rocking system is to trade earthquake damage from the primary structural components (e.g., wall, frame, and connections) into supplemental energy dissipation devices.

The increase in D peak demand of the rocking system is concerning, however, PT walls are design to soften from uplift to decrease stress demand on the wall so this is as expected. Note that for seismic applications, ground motion spectral accelerations at low frequency (i.e., long period) ranges tend to be less than for mid to high frequencies, which is not incorporated into the forcing shown here, as the amplitude is constant for each sweep. In addition, energy dissipation devices such as U-shape flexural plates, see [Kelly et al., 1972; Baird et al., 2014], can further reduce peak demand. Moreover, the steady-state response of

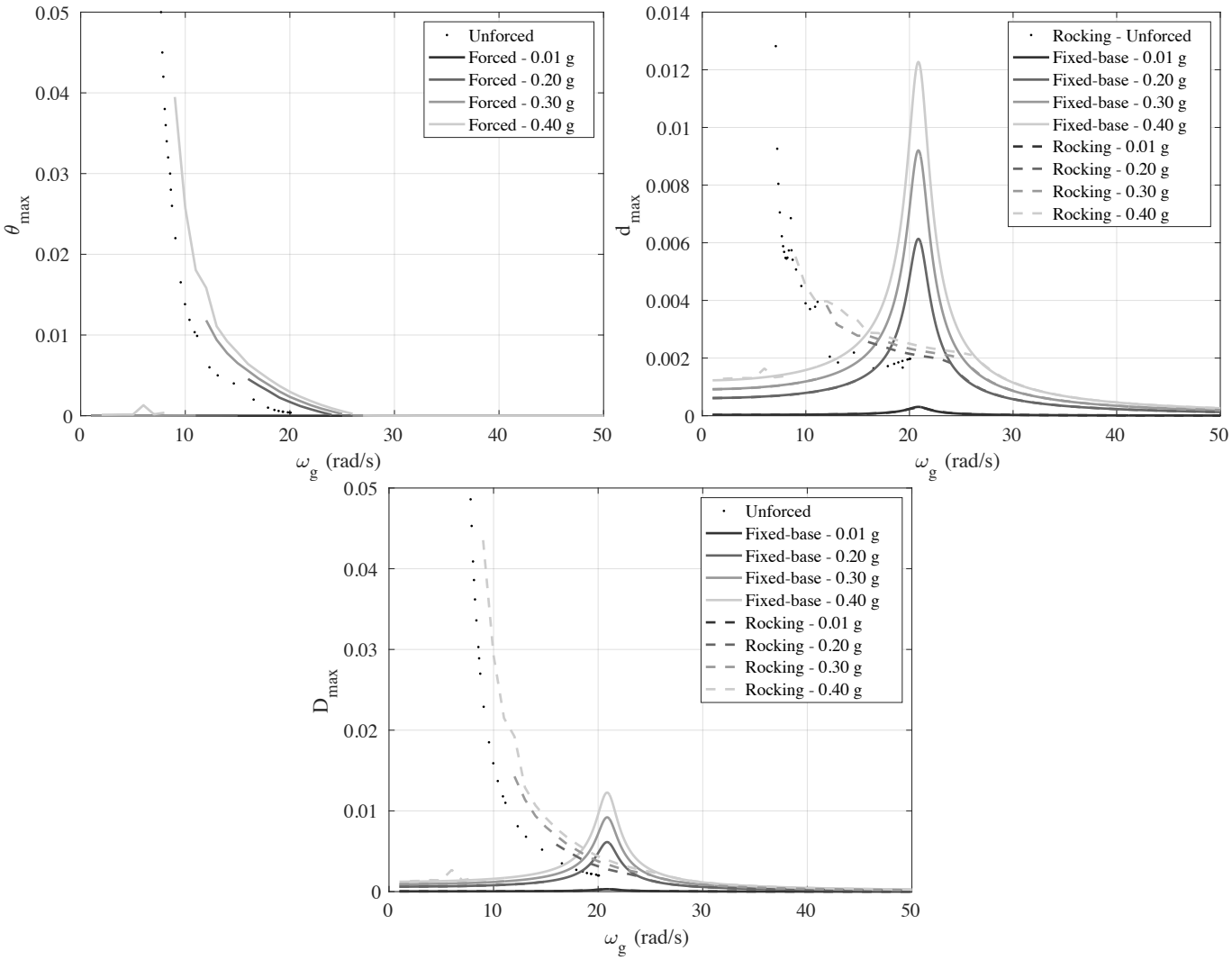

Figure 3.12: Amplitude-frequency plots of forced and unforced vibration of rocking and fixed-base wall.

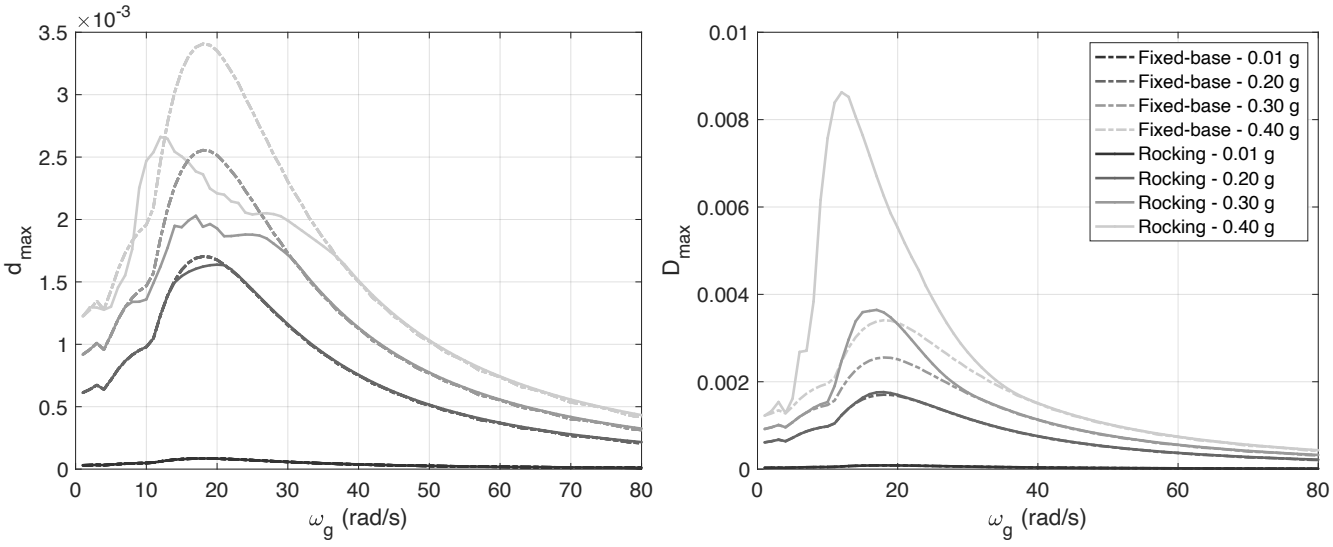

Figure 3.13: Amplitude-frequency response of pulse-excitation.

harmonic loading may represent a more extreme event than earthquakes due to re-occurring high acceleration levels for harmonic loading.

An additional method to observe fundamental characteristics pertinent to ground motions is by using peak demands from pulse-type loading. Figure 3.13 shows the amplitude-frequency plot of a single cycle sinusoidal (i.e., pulse-type) ground motion acceleration. The peak D demands for pulse-type ground motion are more comparable.

Co-existing solutions

Nonlinear systems may exhibit co-existing steady-state solutions. To demonstrate this, a study was performed on forced response ($\omega_g = 53$ rad/s and $A_g = 3$ g) with varying initial conditions. Figure 3.14 shows the resulting 'basin of attraction' plot of θ_{max}; the left plot uses a broader range of initial conditions (-0.05 to 0.05 radians) and illustrates the magnitude of

each steady-state peak response, the right plot is similar except it explores a smaller range at a higher resolution. As seen in other nonlinear systems, the flexible PT rocking wall seems to exhibit a fractal behavior. Note that d_{max} was omitted as the distribution, see Fig. 3.14 (left), is identical. The observation of co-existing solutions signifies that rocking blocks, like many other nonlinear systems, exhibit fractal sensitivity to initial conditions, and system parameters. Thus, it is important to accurately predict the time and state at rocking initiation to accurately predict the forced dynamic response. However, it is also important to perform Monte Carlo simulations to capture the worst co-existing response type. A flexible base/foundation could smooth out the nonlinearity by changing the impact time from infinitesimal to finite, further studies are required here.

Response phase

Another fundamental characteristic of the response is the phase angle ϕ of the generalized coordinates specifying the lag between the response and excitation. The phase angle is often used in linear system to indicate resonance. The efficacy of similarly using ϕ for flexible rocking walls, and additional insight it provides are discussed here. The responses θ or d can be approximated as $f(t) = \sin(\omega_g t + \phi)$. The accuracy of this approximation varies with ω_g, however, it allows for a consistent approach to obtain ϕ. The following equation shows the general process for obtaining ϕ using an arbitrary starting time τ that begins after steady-state is observed:

$$\frac{T}{2}\cos\phi = \int_{\tau}^{\tau+2pi/\omega_g} f(t) * \sin\omega_g t \, dt \tag{3.24}$$

Figure 3.15 shows the plot of ϕ_{mean} versus ω_g, where ϕ_{mean} is the average of the phases obtained using a total of 50 random τ in Eq. (3.24). The standard deviation for θ and d are 0.18 and 0.11 radians, respectively. The phase shift corresponding to vibration-only response (i.e., no rocking) can be seen at the 0.01 g level with nearly linear resonance, see Fig. 3.15 (right). At higher forcing level, rocking is observed and similar phase shift indicating reso-

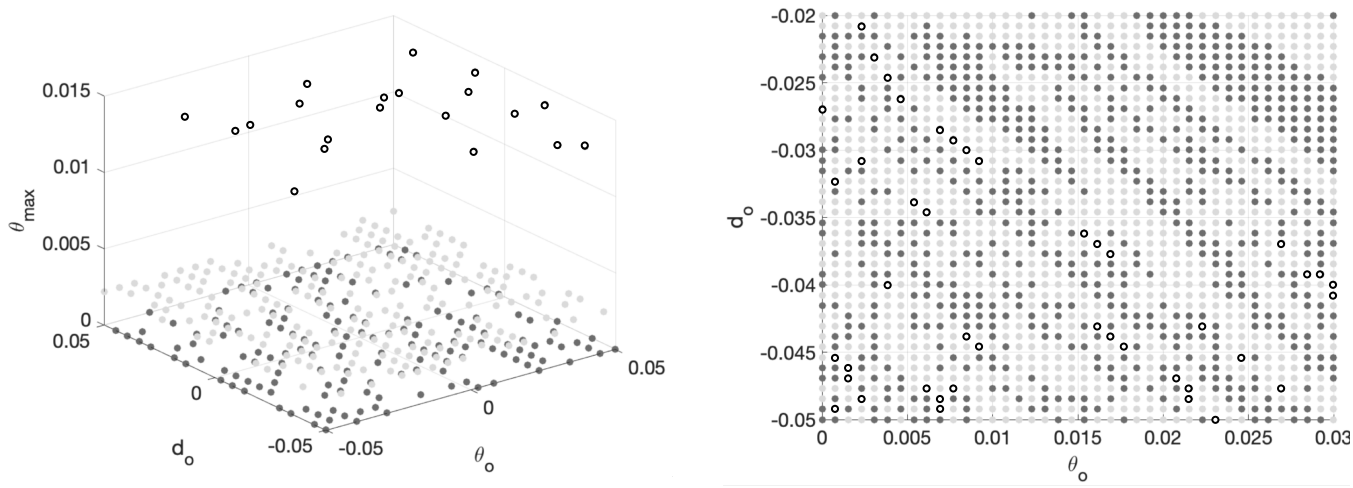

Figure 3.14: Coexisting solutions.

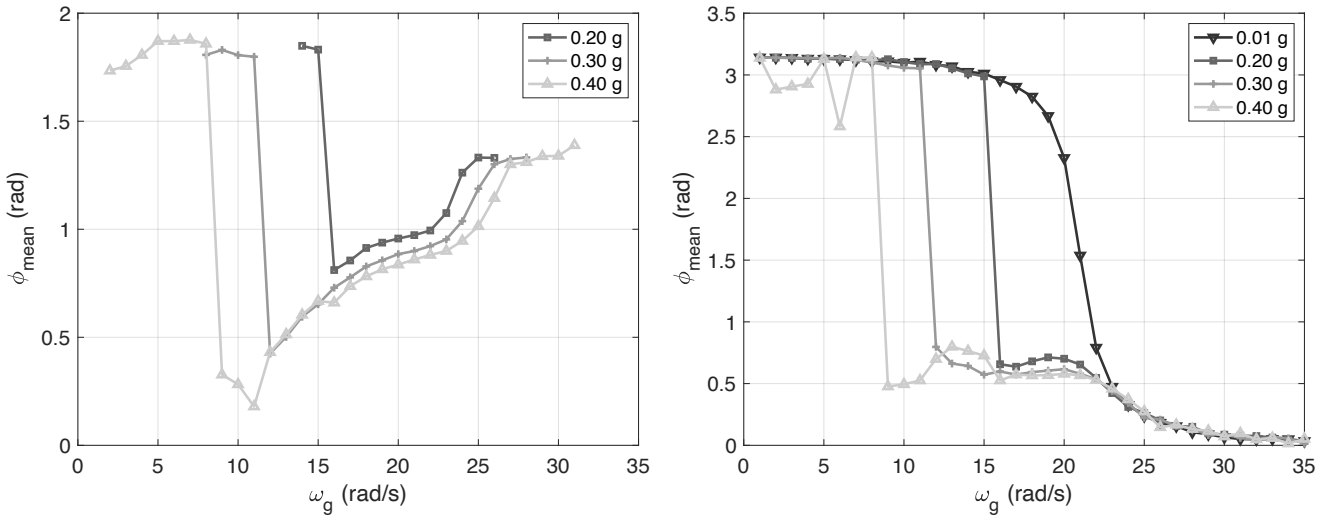

Figure 3.15: Phase response of θ (left) and d (right).

nance occurs although it appears the transition is discontinuous/nonsmooth. Interestingly, it seems the phase angles of both θ and d of the different forcing levels converge before and after resonance. Furthermore, during rocking the phase response of d after resonance approaches a constant value of 0.5 radians; this may allow for approximate harmonic balance solution (approximating the solution as a harmonic function into the equations of motion).

Additional work is needed to better understand how periodically forced response inform seismic response for nonlinear systems; where the periodically forced response is helpful for linear systems, perhaps similar contributions can be made for nonlinear systems.

3.5 Chapter conclusion

This chapter presents a method to analytically study flexible PT rocking walls. The kinematic relationships were provided and a Lagrangian approach specific to lumped masses was

shown to simplify the derivation of the kinetic energy terms of the equations of motion. The initiation of rocking is determined via the dynamic moment and force equilibrium condition. The energy dissipated at impact (i.e., post-impact velocities) were shown to be attainable for the two-degree-of-freedom model introduced here (although the methodology extends to any number of degrees-of-freedom) using the conservation of angular momentum of the system and conservation of linear momentum of the top mass.

The analytical model was validated against two benchmark cases. Furthermore, the pushover results showed the flexibility of the wall changes the stiffness of the system (observed in the roof drift pushover response), as expected, but θ was far less sensitive (as shown in the θ pushover response).

The NNMs were obtained from undamped, unforced response and confirmed to coincide with the peak demands from forced response with varying forcing levels. In addition, the amplitude-frequency relationship of the flexible wall and equivalent rigid wall converges as amplitude increases. At large amplitudes θ drives the response, conversely, at small amplitudes d was the primary factor with the resonant frequency converging to the natural frequency of an equivalent fixed-base wall. The model was able to properly capture the transition from fixed-base vibration to rocking dominant behavior, and qualitatively observe the effects of rocking when compared to the fixed-base wall. Coexisting steady-state peak demands were observed and appear to have fractal characteristics. Lastly, the phase angles were approximated by idealizing the response as a sine wave, and were shown to be able to predict resonance.

The aforementioned findings are important for understanding the rocking phenomenon in the context of earthquake engineering. However, the following work is needed to better simulate real-world structures:

- Further discretization using additional lumped masses and lateral springs along the height of the wall.
- Use ground motions instead of harmonic loading.

- Model energy dissipation devices.
- Model deformable base with damage criteria.

Chapter 4 addresses these points, although via an FE model instead of further extending the analytical model, which would be rather complicated.

Chapter 4

A NUMERICAL STUDY OF TAPERED-BASE POST-TENSIONED ROCKING WALLS

Note: Part of this chapter is a reproduction of [Lin et al., Forthcoming 2023]

Chapter 2 explored the effects of curved bases on the static and dynamic behavior using an analytical model of rigid rocking walls. Chapter 3 looked at the interaction of rocking and wall deformation of rectangular rocking walls. This chapter combines the previous chapters and focuses on the seismic performance and base damage reduction of tapered-base rocking walls using a finite element model. The model includes flexible walls, damage models, energy dissipation devices, and a gravity system. Two case studies are done to evaluate the seismic performance and base damage reduction.

Firstly, this chapter reintroduces the concept of tapered-base rocking walls and gives the preliminary methods for designing the tapered base. Then it presents the case studies followed by the finite element model. Each case study includes the pushover and amplitude-frequency curve of the different designs. Thereafter, the seismic performance are shown with a focus on the base damage reduction.

4.1 Chapter introduction

Rocking has been a topic of earthquake engineering research dating as far back as 1963 when Housner derived the equations of motions of rocking systems to investigate the resilience of a number of tall, slender structures that survived the Chilean 1960 earthquake [Housner, 1963]. More recently, resiliency (in terms of individual structures and complete urban infrastructure systems) has been of great interest due to the substantial costs of building damage

and its cascading impacts on communities. Rocking systems have been studied as a means to limit building damage, reduce direct costs and improve community resilience. For example, Eatherton et al. examined and compared design concepts of rocking of self-centering steel-braced frames with other conventional and self-centering seismic force-resisting systems [Eatherton et al., 2014a]. Moreover, Pei et al. recently conducted a large-scale shake table test of a timber structure with CLT walls to develop and validate a resilience-based seismic design methodology for tall wood buildings [Pei et al., 2019].

As shown in [Pei et al., 2019], one particularly compelling solution to address the seismic resiliency of buildings is the use of Post-Tensioned (PT) rocking walls as the seismic force-resisting system. The next subsection briefly reintroduces previous work on PT rocking walls pertinent to this chapter, followed by areas for improvement. For a more in-depth literature review on PT rocking systems, see Section 1.3.3.

4.1.1 Review of PT rocking walls

During the 1990's the Precast Seismic Structural Systems (PRESSS) project contributed greatly towards PT precast concrete connections and PT rocking walls with a large-scale test of a five-story structure [Priestley, 1991; Kurama et al., 1999] and now have design and detailing requirements in ACI 318-14. The work on PT rocking concrete structures is the basis of the research on PT rocking timber walls, which is the focus of the study in this chapter as timber is more suitable for a tapered base (discussed later). The NHERI Tall Wood project conducted two-story PT rocking wall shake table tests [Pei et al., 2019] with ongoing work for ten-story tests. The two-story tests produced very promising results by passing all the performance objectives. The designs for the two-story and ten-story walls were used as case studies here, discussed later. Several numerical studies followed; Wichman et al. predicted the response of the two-story shake table test with a numerical model by including a flexible foundation to simulated the observation from the test data [Wichman et al., 2022]. The same numerical model methodology, detailed later, is employed in this study. In addition, Pei et al. [Pei et al., 2020] and Hasani et al. [Hasani et al., In press]

also used numerical models to predict the response of the two-story tests. The former used a simplified method that was able to reasonably capture the global response. The latter focused on structure acceleration response for nonstructural elements.

Figure 4.1 shows an archetypal PT rocking wall configuration composed of: a free-standing wall, e.g., a Cross-Laminated Timber (CLT) panel; post-tensioned steel strands/bars; an energy dissipation system, e.g., U-Shaped Flexural Plates (UFPs); and wall-to-diaphragm connections to transfer the inertial forces from the gravity system to the rocking wall. The free-standing wall has a high initial lateral stiffness followed by softening when the base uplifts (i.e., decompresses). Post-tensioning strands increases the post-decompression lateral stiffness and re-centers the wall after the seismic event and the energy dissipation device dampens the system through inelastic deformation [Baird et al., 2014]. The components resolve to a cyclic 'flag-shaped' hysteresis as shown in Fig. 4.2. Flag-shaped hysteretic behavior is found in other seismic designs (e.g., frames with post-tensioned connections) due to the re-centering and energy dissipating properties. Moreover, the uplift (i.e., rocking) mechanism acts as a fuse to limit the internal shear force and bending moment demands on the wall. Ultimately, the objective is that the primary structure remains undamaged and re-centered after an earthquake, and that the energy dissipation devices be easily and quickly replaced after moderate to extreme seismic, vastly increasing the seismic resilience compared to conventional design performance objectives.

While not the only energy dissipation option, UFPs are a suitable for several scenarios. They can be used to connect paired rocking walls as was done in a recent two-story test [Pei et al., 2019]. Alternatively, as shown in Fig. 4.1, they can be placed between a rocking wall and adjacent gravity columns. The mechanics of UFPs are also well-known. Kelly et al. derived the plastic force [Kelly et al., 1972] in Eq. (4.1). Using strain energy methods, the equation for the initial stiffness of the UFP was derived by Baird et al. [Baird et al., 2014] in Eq. (4.2). In these expressions $f_{y,UFP}$, b_u, t_u, D_u, and E_{UFP} are the yield stress, width,

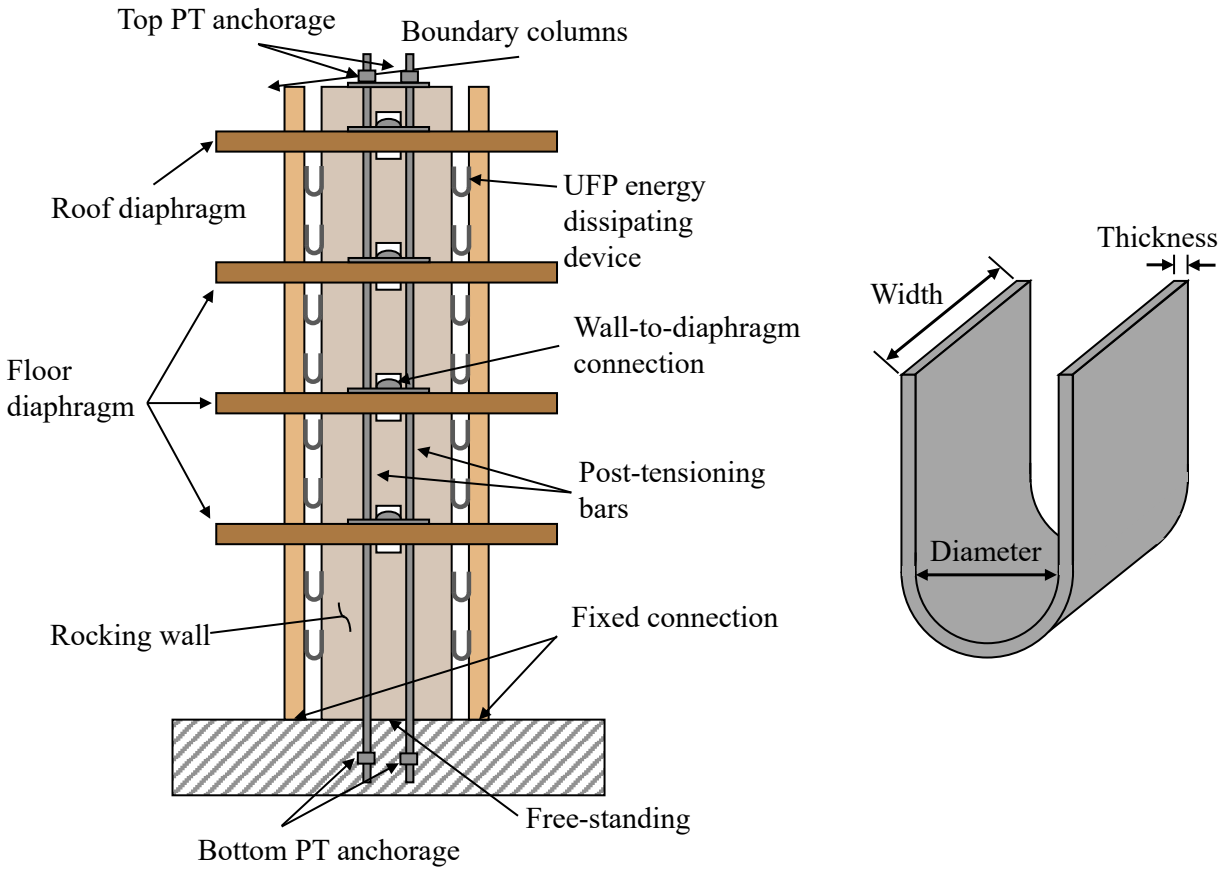

Figure 4.1: Diagram of PT rocking wall (left), UFP (right).

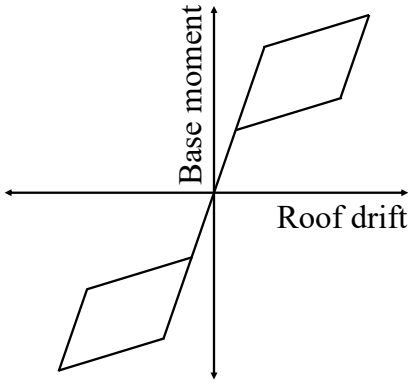

Figure 4.2: Cyclic flag-shaped hysteresis.

plate thickness, diameter, and modulus of elasticity of the UFP.

$$F_{p,UFP} = \frac{f_{y,UFP} b_u {t_u}^2}{2D_u} \tag{4.1}$$

$$k_{o,UFP} = \frac{16 E_{UFP} b_u}{27\pi} \left(\frac{t_u}{D_u} \right)^3 \tag{4.2}$$

The study here used CLT panels, however the geometric modification (which is the focus of this study and will be discussed later) is material agnostic. The cyclic response of CLT PT rocking wall was explored and structural limit states were defined by Akbas et al. [Akbas et al., 2017] and Ganey et al. [Ganey, 2015]. They observed the flag shape hysteresis with the limit states design to occur in the following order: (1) decompression; (2) UFP yielding; (3) base yielding; (4) base splitting; (5) base crushing; and (6) PT yielding. Limit states (3) to (5) are based on the wall material, specifically the compression stress-strain relationship (including damage). After yielding, the CLT stress-strain relationship can be approximated with a zero strain-hardening until it splits, after which the strength degrades down and then crushes. Barbosa et al. tested CLT under compression and found that crushing occurs when strength degrades down to approximately 25 percent of the yield stress [Barbosa et al., 2018].

Pertinent to the work herein, Bachmann et al. looked at (rigid, non-PT) rocking columns with a curved base of constant curvature to improve stability [Bachmann et al., 2016]. Similarly, using analytical models, the study shown in Chapter 2 looked at curved-based rocking PT walls, however, the scope was also on rigid walls to isolate the effects of the curved base on the static and dynamic characteristics. Subsequently, the study shown in Chapter 3 generalized the analytical model to flexible rocking (rectangular) walls with rigid base. The base modification in the first two studies reduces the stress concentration in the corners during rocking, and thus lessen the damage, e.g., CLT splitting/crushing. Ganey performed pushover tests on PT CLT walls and observed damage in the CLT panels led to loss of PT force [Ganey, 2015]. Concrete structures are also at risk of base damage. Henry et al. experimentally and analytically investigated base damage, i.e., toe crushing, on PT concrete

walls and found a strain of 0.005 is recommended for defining the nominal flexural strength of PT concrete walls [Henry et al., 2012].

4.1.2 Impetus for base protection and tailoring pushover curve

Rectangular rocking walls have an inherent issue where the base impact and the stress concentration during rocking could lead to base damage, as mentioned before. Visible damage at the base is both a concern for serviceability and strength degradation. To address this issue, this study looks at a geometric modification of the base to reduce the stress demands during moderate to extreme seismic events, and effectively further expands the scope of Chapters 2 and 3 to flexible rocking walls with a modified base.

By modifying the geometry of the base, PT rocking walls may also be tailored to deliver multiple lateral stiffnesses at different lateral displacements, similar to variable friction pendulum systems. Tailoring the pushover curve may be advantageous when considering different hazard levels, e.g., for smaller earthquakes drifts can be limited with a large initial stiffness preventing damage to nonstructural elements and ensuring serviceability, for medium earthquake demands a reduction in stiffness when rocking occurs will reduce forces in the system , and then an increase in stiffness at large lateral deformations will help to reduce damage and collapse probabilities for extreme events.

4.2 Overview

The research presented here examines the impact of geometric modification to the base of PT rocking walls on their seismic performance to develop recommendations for use of this concept in design. To accomplish this objective the presentation begins with an introduction to the geometric modification and associated design approaches. This is followed by an introduction of the ten-story case studies used to evaluate the efficacy of the geometric modification. After, the modelling methodology and assumptions made are presented. Note, this study primarily focused on the effects of the modification with the ten-story case, and later narrowed the focus to base damage reduction with the two-story case. The last two

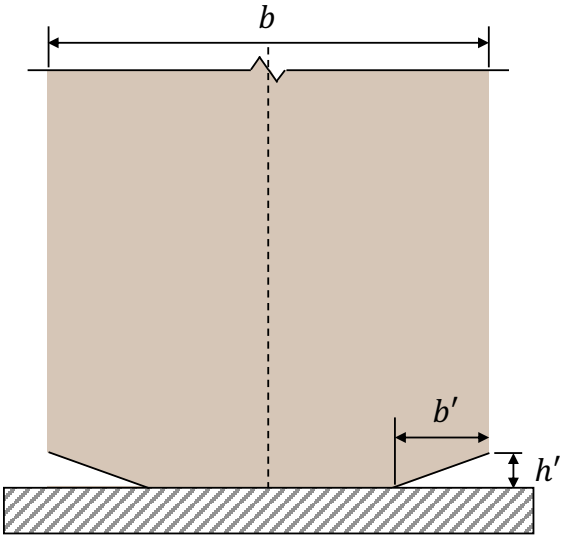

Figure 4.3: Tapered wall (exaggerated); PT bars and other components are omitted for clarity.

sections present the results of the ten-story and two-story case studies, respectively.

4.2.1 Geometric modification to wall base

The study in Chapter 2 showed that curving the corner of the wall introduces additional design parameters to tailor the static and dynamic characteristics — e.g., the pushover and amplitude-frequency response — of a rocking system. The study herein is of similar nature in which the corners of the wall are tapered to reduce the sharpness and mitigate base damage. A tapering cut was used here, see Fig. 4.3, instead of a curved base due to the increased complexity of this study compared to the work in Chapter 2, in which the wall was idealized as rigid with no material models to simulate base damage. Reintroducing the curved base to a deformable wall is outside the scope of this chapter and is left for a future study.

Preliminary design concept

The geometric modification introduces two design parameters, b' and h', denoting the width and height of the tapering cut, respectively, as shown in Fig. 4.3. This subsection will use a rigid base/foundation assumption to illustrate the effects of the geometric modification on the pushover response. Figure 4.4 shows the pushover response (base moment vs. roof drift) of a rectangular wall and three different tapered walls. Note that roof drift is δ_R/h_R, and story drift (explored later) is $(\delta_T - \delta_B)/h_s$, where δ_T, δ_B, δ_R, h_S, and h_R are the top and bottom lateral deflection of a story, lateral deflection of the roof, story height, and building height, respectively.

The tapered walls can rotate about the interior and exterior corner, effectively providing two rocking stages with varying lateral stiffness – referred to herein as stages 1 and 2 (note that there are three stages for curved-base rocking walls as shown in Chapter 2). However, unless other changes are made, the tapering decreases the overturning moment needed to uplift the base — i.e., decompression moment, denoted here as M_{dec} — as a result of the decrease in lever arm. As expected, M_{dec} decreases with larger b', see Fig. 4.4. Under rigid wall/ground assumptions, the rotation at which stage 2 initiates is a function of the arctangent of h' divided by b'. As a result, when b' increases, stage 2 rocking occurs earlier. Conversely, if h' increases, stage 2 rocking occurs later. With deformable walls, stage 1 and 2 are not as pronounced as the compression zone is distributed to a surface area. Thus, stage 2 initiates at smaller rotations if the deformability of the wall base is considered.

The tapered walls were designed with two different approaches using the rectangular wall as a baseline. The ten-story rectangular wall is the baseline case and denoted here as 10B. Note that the different approaches for tapering the wall base are exploratory, i.e., not optimized, where only the parameters b, b', and h' are explored. Additionally, as will shortly be apparent, the two approaches will likely bracket the optimal case.

The first tapering approach, referred herein as 10T, is to have the width, b, equal to the rectangular wall and to use a reasonable b' value based on the following considerations. These

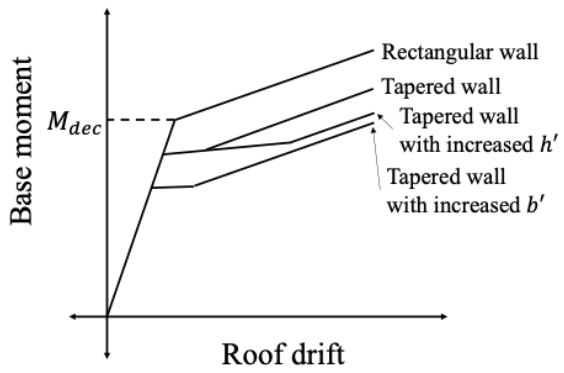

Figure 4.4: Effects of tapering parameters on idealized pushover response.

are that a large b' would lower M_{dec}, however a small b' would (1) require a proportionally small h' for stage 2 rocking to occur at desirable deflection levels; and (2) reduce the effect of the geometric modification. Designing the h' to be too small would be impractical for fabrication, however fabrication feasibility is outside the scope of this paper. Lastly, h' was designed such that the pushover response of 10T and 10B would converge at a desired deflection/drift level (one percent roof drift was targeted in this study).

The second tapering approach is to increase b (taking into account the limitation set forth by the architectural floor plan). By increasing b, the b' value can be chosen such that $b - 2b'$ equals the width of 10B. As a results, the lateral stiffness would be similar to 10B until stage 2 rocking. Then, h' was designed such that the pushover response would produce an increase in lateral stiffness (due to stage 2) at a desired deflection/drift level (again, one percent roof drift was used). This study explores two walls under this approach, denoted as 10WT1 and 10WT2. The latter decreases h' to evaluate the performance when stage 2 occurs at a smaller roof drift. A second rectangular wall, with a b equal to that of the 10WT1 and 10WT2, referred to as 10W is used to investigate the effects of b' and h' of this second approach (and not the increase in b). Table 4.1 provides the different design parameters of the walls discussed.

Table 4.1: Tapered wall design (units in cm).

	10T	10WT1	10WT2
b'	23.11	15.24	15.24
h'	0.38	1.27	0.64

4.2.2 Case studies

Ten-story case study

To evaluate the effects of the tapered wall, discussed in the next subsection, the performance of a rectangular ten-story PT rocking wall was compared against various tapered walls. The design of the rectangular ten-story wall is briefly detailed in this subsection, however as the focus of this study is the effects of the geometric modification, an in-depth discussion on the design methodology is not discussed. For more information on the design methodology, the reader is referred to [Pei, 2022; Wichman, 2022].

The rectangular wall design was developed by the NHERI Tall Wood project for large-scale shake table tests in the University of California, San Diego [Pei, 2022] Note that the design is preliminary and may be subject to change as the experiments are scheduled to take place in the fall of 2022; in addition, there are no test data available for the ten-story wall design, however, similar tests were done on two-story rocking wall system [Pei et al., 2019].

The ten-story rectangular wall is shown in the diagram in Fig. 4.1. The design parameters and values of the rectangular ten-story wall are given in Table 4.2.

4.3 Model

This section discusses the assumptions used herein followed by the method used to model the tapered rocking walls.

Table 4.2: Ten-story wall parameters (units in kN and m).

	Parameter	Value
Gravity Frame	Height of 1st story	3.96
	Height of remaining of stories	3.35
	Weight of 2nd floor	65.39
	Weight of remaining floors	63.61
	Weight of roof	57.03
Wall	Height	34.14
	Width	2.87
	Thickness	0.31
	Weight	127.93
	Modulus of elasticity	7037764
	Shear modulus	459674
	Yield strain	0.003
	Splitting strain	0.008
	Crushing strain	0.038
	Yield stress	18202
	Splitting stress	18202
	Crushing stress	2730
PT	Area of PT (per side)	0.00125
	Modulus of elasticity	$200e^6$
	Eccentricity	0.18
	Yield stress	723950
	Initial PT force	222.41
	Hardening ratio (β_{PT})	0.050
Boundary Columns	Thickness	0.445
	Width	0.302
	Modulus of elasticity	12410568
UFP	Diameter	0.159
	Thickness	0.013
	Width	0.102
	Yield stress	289580
	Modulus elasticity	$200e^6$

4.3.1 Model assumptions

The study here focuses on the rocking wall, and as such, the gravity frame (i.e., leaning columns and diaphragms) is idealized with rigid elements with hinge connections between the wall, diaphragms, and columns. The gravity frame produces both the inertial lateral forces from the mass of the floors/roof, and the second-order geometric non-linear gravity moments (i.e., P-Delta moments). There are multiple diaphragm-to-wall connection types, see [Pei et al., 2019; Wichman, 2018; Moroder et al., 2017], however, the effects of the connection is outside the scope, and as such, a simple hinge connection that allows the wall to move vertically relative to the floors was used as discussed in the numerical model description below. To ensure there were only lateral forces transferred from the gravity frame to the wall, only the horizontal component of the floor masses was modeled.

The foundation is assumed to be perfectly rigid. Studies have observed that the stiffness of the foundation has an impact on the response of rocking structures [Kibriya et al., 2018; Kashani et al., 2018; Bachmann et al., 2017; Alexander et al., 2011]; however, in most practical applications of rocking timber walls the foundation deformation will be negligible relative to the deformation of the wall. Moreover, Wichman et al. found the deformable foundation beam prevented the corner of the base of the panel to be damaged [Wichman et al., 2022]. Interestingly, a foundation beam deformed at the corner of the wall effectively results in the same mechanics as a curved-base rocking wall. It is also assumed that there is no sliding between the wall and base, either through friction, or through steel angled plates fixed adjacent to the corners of the wall. The latter approach has been used to prevent sliding and to transfer the shear force from the wall to the foundation during shake table tests [Wichman, 2018].

As mentioned earlier, boundary columns are used to connect the UFPs to the wall however the columns do not contribute to the lateral resistance. This was achieved by changing the fixity of the columns to pins to allow base rotation and using a slender a cross-section to allow deformation without significant constraint forces on the rocking wall. The lateral

displacements of the boundary column at the height of each UFP are assumed to be equal to the corresponding lateral displacement of the wall.

To model the axial stress-strain behavior of the wall base, a multispring model was used that translates the axial stress-strain material model (obtained from experimental data) to zero-length compression only axial springs. The multispring model is developed with an analogous plastic-hinge theory to calibrate the base spring stiffness and model the rocking mechanics. An in-depth discussion and derivation of the model is given by Ganey [Ganey, 2015] and Wichman [Wichman, 2018]. The plastic-hinge length is assumed to be six percent of the height of the wall, which was validated in [Wichman et al., 2022].

4.3.2 Finite element model

As mentioned earlier, the modeling approach is based on the work in [Ganey, 2015; Wichman, 2018] with some important modifications to handle the tapered base. Wichman et al. used the same techniques to model the two-story wall and was able to reproduce the experimental data [Wichman et al., 2022]. The following will briefly discuss the numerical model but focuses on the modifications needed to handle the tapered base. For more in-depth discussion on the rectangular wall numerical model, the reader is referred to [Ganey, 2015; Wichman, 2018].

The numerical models were developed using OpenSees [McKenna, 1997]. Figure 4.5 shows a model schematic and components of the model. The following list details the structural components; the element and material models from OpenSees are italicized:

- The wall is modeled as a Timoshenko beam to account for both flexural and shear stiffness (*forceBeamColumn* element with *Elastic* section with both the modulus of elasticity and the shear modulus).
- The PT bars were modeled with truss elements (*corotTruss*) with material model steel (*steel02*), see Fig. 4.6.
- Rigid elements were modeled with very stiff beams (*elasticBeamColumn*).
- The boundary columns were modeled with Bernoulli-Euler beams (*elasticBeamCol-*

umn);

- The rocking and contact interaction were modeled with 80 zero-length multispring elements. The location and axial strength of the elements were calculated using the Lobato integration method. The *flatSliderBearing* element was used to model the zero-length spring with friction, compression, and zero-tension strength. The friction was modeled with Coulomb friction (*Coulomb*) with a very large coefficient of friction. The axial behavior was the combination of two material models in series: *Hysteretic* and *ElasticPPGap* (see Fig. 4.6). Note that $\varepsilon_{s,CLT}$, and $\varepsilon_{c,CLT}$ denote the strain of the CLT at splitting and crushing, respectively. The h' parameter is modeled using the gap parameter in the *ElasticPPGap* material model. As shown, the geometric modification is simple to implement in numerical models and to fabricate.
- UFP was modeled using a zero-length spring element (*zeroLength*) in the shear (i.e., vertical) direction with a steel material model (*Steel02*), see Fig. 4.6. As mentioned above, the lateral displacement of the boundary columns are constrained to the lateral displacement of the wall at the UFP heights. This was achieved by using a rigid zero-length spring element in the axial (i.e., horizontal) direction.
- The floor/roof masses were placed on the gravity columns. The mass of the wall was discretized and placed at the height of the floors and roof.
- All elements used the corotational geometric transformation.

4.4 Static and dynamic characterization

This section discusses the static and unforced dynamic response of the rocking wall system — inherent and is the nonlinear equivalent of stiffness and natural frequency — which gives insight to the forced dynamic response (discussed in the next section). The static behavior is characterized with pushover analyses, illustrating the lateral resistance with respect to displacement; the displacement can be quantified either by story/roof drift or base rotation. The former factors in the elasticity of the wall and latter focuses on the rocking response.

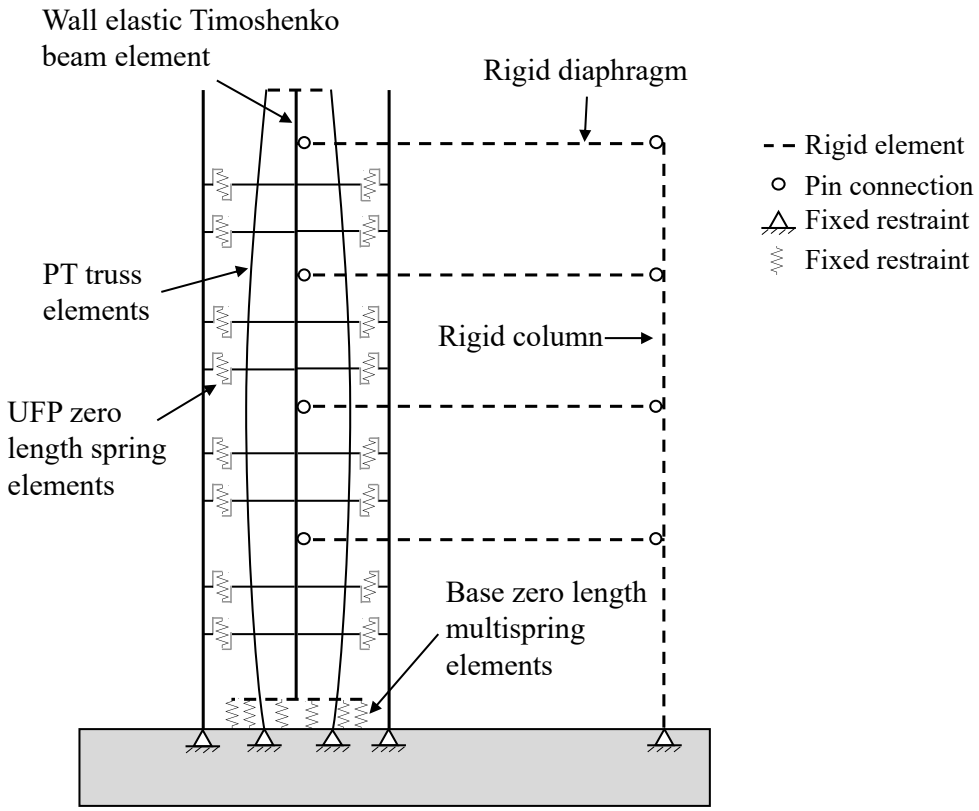

Figure 4.5: Diagram of finite element model (adopted from [Wichman et al., 2022])

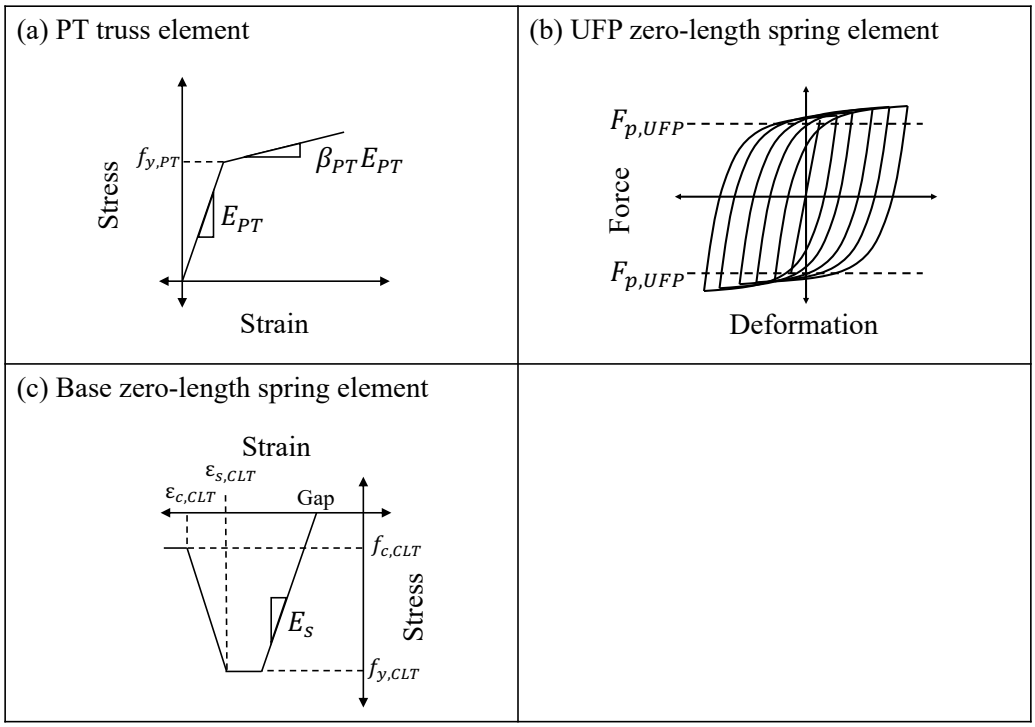

Figure 4.6: Material models for the PT bar, UFP, and multi-springs.

Dynamically, the behavior is characterized by using the (free-vibration) amplitude-frequency relationship. This relationship illustrates the (nonlinear) normal modes of the system. The study shown in Chapter 3 used analytical models to examine nonlinear normal modes of flexible rocking walls and showed the transition of the dynamic response from fixed-base vibration to rocking. Moreover, the (free-vibration) amplitude-frequency relationship characterizes the nonlinear resonance of the system. Note that a linear system would have a constant natural frequency for all amplitudes; conversely the resonant frequency is a function of amplitude for a nonlinear system. For a more in-depth discussion on nonlinear normal modes, the reader is referred to [Kerschen et al., 2009].

4.4.1 Static response

The pushover analyses were conducted with distributed lateral forces at each floor and roof per Equivalent Lateral Force method in ASCE 7. Figure 4.7 shows a plot of the pushover response of the rocking systems. Firstly, M_{dec} of 10T is greatly reduced, however converges again at approximately 1.5 percent roof drift. This is as designed and due to stage 2 where the lever arm of 10T equals that of 10B. The same behavior is observed when comparing 10WT1 and 10WT2 with 10W. Stage 1 and 2 of 10T to not appear to be as distinct which is due to the elasticity of the base, as mentioned previously.

Note, 10WT1 and 10WT2 match 10B prior to 1 percent drift, increasing afterwards in stage 2. From 10WT2, it is shown by decreasing h', the lateral stiffness increases during stage 2. Effectively, 10WT1 and 10WT2 were able to be tailored to replicate the 10B and 10W behaviors at low and high drift levels, respectively.

Table 4.3 provides the capacities of the different walls — e.g., the base shear and roof drift when the PT bar yields or when the wall base yields. Note, (i) base crushing capacity was not included as the base did not crush during the pushover simulation; (ii) for the tapered walls, the value inside the parenthesis pertains to the exterior corner; and (iii) WNO (was not observed) signifies capacity was not exceeded in the pushover simulation.

It is clear that the lateral displacement base capacity of the tapered walls is much greater

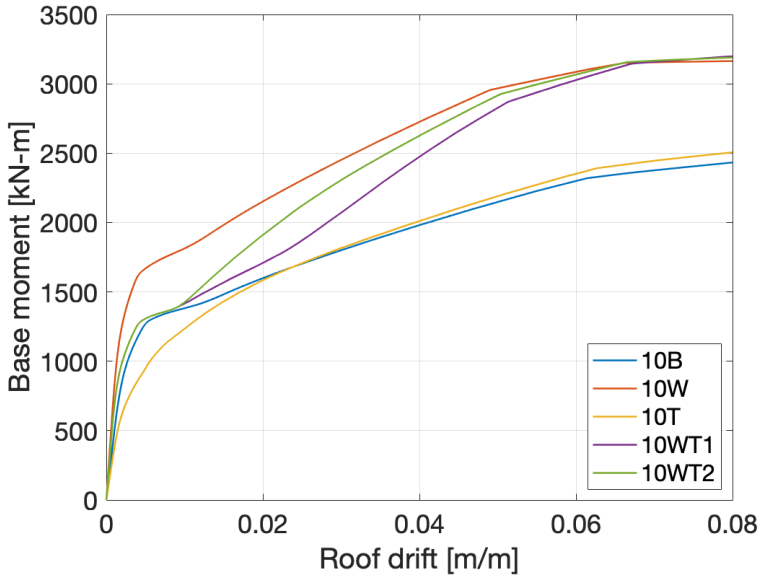

Figure 4.7: Ten-story pushover response.

Table 4.3: Capacity of ten-story walls.

	10B	10W	10T	10WT1	10WT2
Roof Drift [e-2 m/m]; Base Rotation [e-2 radians]					
Base Yield	1.6; 1.4	1.5; 1.3	WNO (2.1); (1.8)	1.9 (3.8); 1.8 (3.6)	WNO (2.5); (2.3)
Base Split	5.1; 4.8	4.7; 4.5	WNO (5.7); (5.4)	WNO (7.6); (7.3)	WNO (5.9); (5.6)
PT Yield	6.1; 5.8	4.9; 4.6	6.3; 5.9	5.1; 4.9	5.0; 4.8
Base Moment [kN-m]; Base Shear [kN]					
Base Yield	1501; 93	1979; 111	WNO (1600); (89)	1692 (2384); 93 (107)	WNO (2100); (107)
Base Split	2171; 89	2911; 125	WNO (2310); (89)	WNO (3183); (111)	WNO (3049); (120)
PT Yield	2320; 89	2957; 125	WNO (2392); (89)	2870; 116	2926; 120

than the rectangular walls. Moreover, from the drift and rotation capacity of 10WT1 and 2, it is shown how h' distributes the base damage over the interior and exterior corners: a deeper h' gap parameter, as expected, results in more damage to the interior corner, and vice versa. Yielding of the PT bars is not the focus of this study, however, it is of concern as it leads to loss of lateral resistance. Thus, it is good that the tapered walls had similar drift/rotation capacity for yielding of the PT bars. Similarly, the strength capacity of the tapered walls did not deviate significantly from the respective rectangular walls. From the capacities of the different walls, it is shown that tapered-base walls would be more resilient to seismic loads as they can be pushed further while resisting the same lateral force before sustaining damage relative to the equivalent rectangular wall.

4.4.2 Dynamic response

The free vibration analysis was done by first displacing the system laterally under displacement control — using the distributed lateral forces — until the base rotation reached the target amplitude and then releasing the lateral forces to allow the system to re-center through free (oscillating) decay. The time it takes for the base to impact the ground is taken as a quarter of the period. Note that this method does not necessarily result in the exact solution for the nonlinear resonant response. This is taken in the sense of Nonlinear Normal Modes (NNMs) as periodic nonlinear response [Kerschen et al., 2009]. The oscillation from the wall's lateral deformation is not necessarily synchronized with the rocking, i.e., the base may impact the ground while the wall is still deformed, therefore does not meet the requirement for a normal mode. This, however, is very difficult to achieve as there is likely only one combination (solved heuristically) of the floors and roof displacements to synchronize the rocking and wall oscillation. Thus, the method used in this study does not solve the exact resonant frequency of synchronized modes however allows for the dynamic behavior of the different rocking systems to be compared based on the dominant rocking frequency.

The amplitude-frequency relationship is shown in Fig. 4.8. The curves focusing on the near-zero rocking amplitude, a co-existing fixed-based wall oscillations also occur. As seen

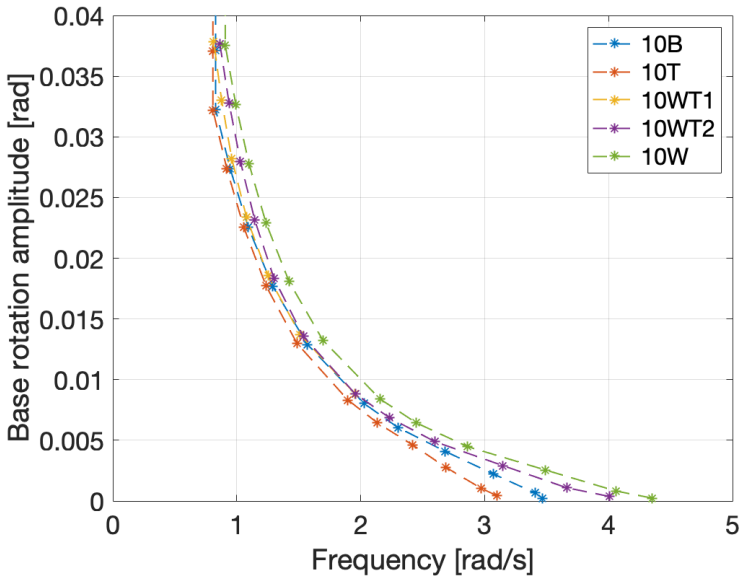

Figure 4.8: Ten-story amplitude-frequency.

in this figure, the 10W has the highest frequency for any given wall response amplitude, followed by 10WT2, 10WT1, 10B, and 10T, as expected. Interestingly, 10B and 10WT1-2 do not have similar frequencies at near-zero amplitudes. Although the rotation point is of equal distance to the centroid of the wall. This is because 10WT1-2 have bigger moment of inertias, and thus higher frequencies, as frequencies at near-zero amplitudes are driven by fixed-base behavior, as shown in Chapter 3. Conversely, frequencies at higher amplitudes are driven by the rocking (i.e., rotational inertia). In effect, the tapered wall systems with similar (stage 2) rotational inertia to the rectangular counterpart start to converge at higher amplitudes, see 10B and 10T in Fig. 4.8. Furthermore, 10WT2 converges to 10W quicker than 10WT1 due to the smaller h'. Lastly, there is a certain range of amplitude where the 10B and 10WT1-2 converge due to similar (stage 1) rotational inertia.

These curves demonstrate the transition from fixed-base behavior for small amplitude response to rocking-dominant behavior for large amplitude response.

4.5 Dynamic response under ground motions

The previous section examined both the static and dynamic properties of the different systems. This section will investigate the rocking response of the rocking systems to a suite of ground motions. The performance is presented in terms of story and roof drifts, accelerations, shear and bending moment, and strain demands at the bottom of the wall (i.e., damage). The maxima that are presented herein are the peak values observed during the nonlinear time-history analysis. Moreover, the plotted data, unless noted otherwise, are the median value of the record-based maxima for each hazard level ground motion set.

4.5.1 Ground motions and response spectra

The ground motions used in this study were selected and scaled such that the average of the ground motions response spectra matches the design, as per ASCE 7-16. The ground motions were scaled to four hazard levels with return periods of 475, 975, 2475, and 4975 years. At each hazard level 11 ground motions were selected and scaled per ASCE 7-16 to match the unified hazard spectrum. As this study is focused on the geometric modification and not the design of the reference wall (i.e., 10B), discussion on the ground motion selection and scaling is omitted; the reader is referred to [Wichman, 2022] for more details. Information on the ground motions are provided in Appendix D. The response spectra are shown in Fig. 4.9 where S_a, g and T_n, s are the spectral acceleration in terms of acceleration of gravity and period in seconds, respectively.

4.5.2 Maximum story/roof drifts

For rocking walls, the most critical challenge is the damage sustained during base impact. Nevertheless, when considering the rest of the building elements, limiting the story drift is important for preventing both structural and non-structural damage, both of which may incur substantial repair and operational cost. Moreover, managing roof drift demand is critical for preventing collision with adjacent buildings and for general serviceability requirements.

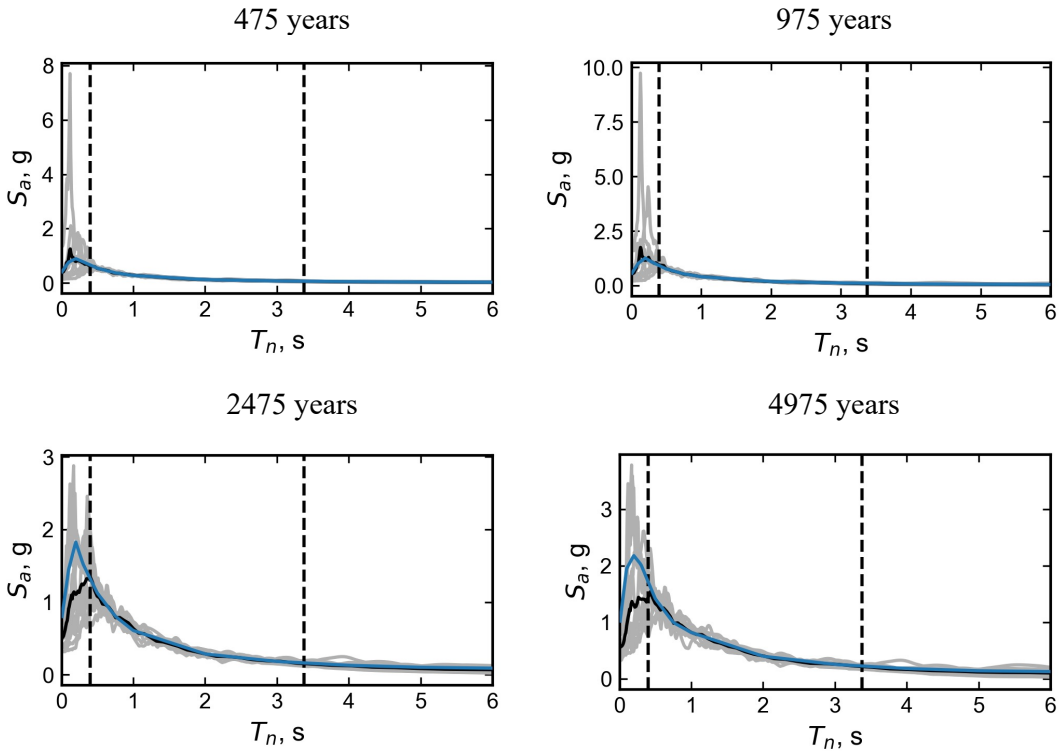

Figure 4.9: Response spectra of ground motions for ten-story design (individual ground motions are in grey, the average is in black, the design is in blue, and the vertical dashed lines are the period range used for selection and scaling).

Figure 4.10 shows the plots of the maximum story (left) and roof (right) drifts; the statistical values are given in Table 4.4. Note that an outlier is defined herein as a value that is more than three scaled median absolute deviations away from the median. The figure shows that the drift is smaller than 10B for 10WT1 and 2 while for 10T it is larger, which is expected given the reduced strength and post-decompression stiffness. Furthermore, the drift at the 2475 year return period hazard level is less than 2 percent for all designs, satisfying the design intent. Interestingly, both 10WT1 and 2 achieved a smaller maximum story drift than 10W at the 975 year return period hazard level. This could be due to the amplitude-frequency relationship where the resonant frequencies of 10W at amplitudes experiences at that hazard level could more closely match the frequencies of the ground motions. Note that the plot is also the median value and thus not necessarily a direct comparison of the same ground motions. In all cases the roof drift is similar to the maximum interstory drift, which indicates a predominantly rocking mode of behavior (i.e., the deformation of the wall itself while non-zero is not large).

Table 4.4: Statistical values of drift demands.

Return Period (years)	Stat. Values	10B	10W	10T	10WT1	10WT 2
Story Drift Ratios [%]						
475	Min	0.59	0.58	0.80	0.73	0.73
	Lower Quartile	0.77	0.66	0.83	0.75	0.75
	Upper Quartile	0.97	0.81	0.96	0.81	0.81
	Max	1.05	0.84	1.02	0.83	0.83
	No. of Outliers	0	0	0	1	1
975	Min	1.05	0.81	0.89	0.86	0.86
	Lower Quartile	1.08	0.92	1.10	0.95	0.95
	Upper Quartile	1.27	1.03	1.27	0.98	0.99

	Max	1.36	1.15	1.51	1.07	1.07
	No. of Outliers	1	1	0	2	2
2475	Min	1.41	1.27	1.37	1.24	1.24
	Lower Quartile	1.51	1.31	1.56	1.34	1.34
	Upper Quartile	1.65	1.48	1.80	1.50	1.50
	Max	1.74	1.72	1.88	1.64	1.64
	No. of Outliers	0	0	0	0	0
4975	Min	1.67	1.58	1.69	1.55	1.55
	Lower Quartile	1.91	1.71	1.90	1.64	1.65
	Upper Quartile	2.53	1.93	2.65	2.22	2.22
	Max	2.82	2.07	3.13	2.50	2.33
	No. of Outliers	1	0	0	0	0
Roof Drift [e-2 in/in]						
475	Min	0.50	0.51	0.67	0.53	0.53
	Lower Quartile	0.60	0.56	0.74	0.57	0.57
	Upper Quartile	0.80	0.63	0.77	0.67	0.67
	Max	0.82	0.70	0.78	0.76	0.76
	No. of Outliers	0	0	3	0	0
975	Min	0.73	0.71	0.77	0.68	0.68
	Lower Quartile	0.87	0.75	0.88	0.75	0.75
	Upper Quartile	0.97	0.88	1.05	0.91	0.91
	Max	1.01	1.02	1.15	0.97	0.97
	No. of Outliers	1	0	0	0	0
2475	Min	1.16	1.00	1.13	0.98	0.98
	Lower Quartile	1.27	1.10	1.31	1.14	1.10
	Upper Quartile	1.37	1.26	1.53	1.32	1.31
	Max	1.50	1.52	1.57	1.50	1.49

	No. of Outliers	0	0	0	0	0
4975	Min	1.41	1.36	1.43	1.42	1.42
	Lower Quartile	1.63	1.50	1.63	1.52	1.48
	Upper Quartile	2.03	1.64	2.34	1.80	1.77
	Max	2.43	1.83	2.79	2.12	2.09
	No. of Outliers	1	0	0	1	1

Similar to the pushover results, 10WT1 and 10WT2 had similar drifts at lower hazard levels (less than 2475 year return period) but diverge at higher levels. Conversely for roof drifts, the two system behaved similarly at all hazard levels. Another observation is that both systems produced smaller story drifts at the lowest hazard level compared to 10B, however, were much closer in roof drift. Moreover, 10WT2 was able to more closely match the drifts of 10WT1 at the highest hazard level. Overall, 10WT1 and 10WT2 were able to limit drift levels similarly to 10B and 10W at low and extreme hazard levels, respectively. The ability to tune the response of a tapered wall — as a narrow wall at low hazard levels to limit stress demands and as a wide wall at high hazard levels to limit drift demands — could be leveraged by structural engineers for seismic or wind design.

10T produced maximum story drifts (at lower hazard levels) that matched 10B even with less lateral stiffness. Furthermore, the roof drifts of the narrower walls (10B and 10T) were more sensitive to increase in hazard level, an observation that is also seen for the acceleration and force demands, see next subsections.

In addition to drift demands, floor/roof accelerations are important when considering damage to sensitive equipment (e.g., servers or medical equipment), as well as general serviceability requirements. The following subsection looks at the acceleration demands.

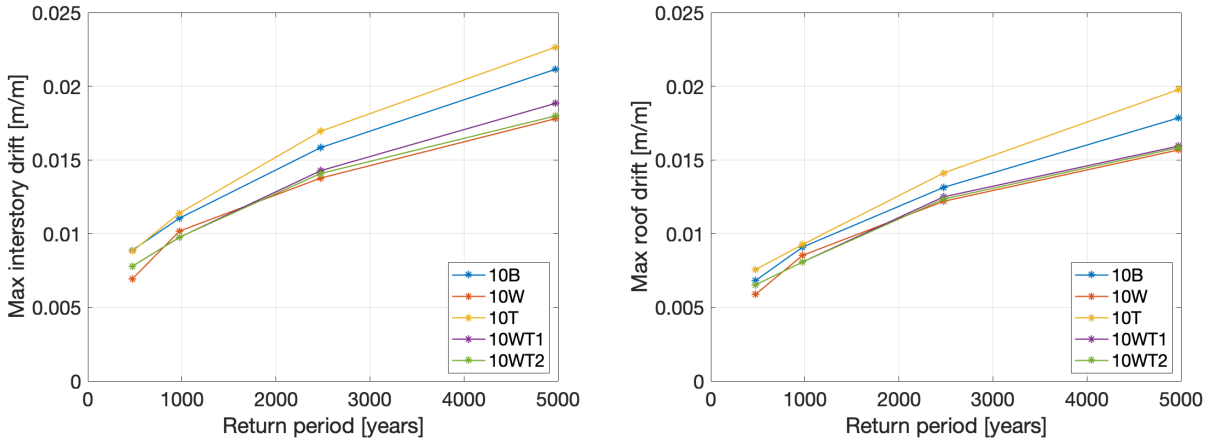

Figure 4.10: Ten-story max drifts; (left), roof (right).

4.5.3 Max story/roof accelerations

Figure 4.11 shows the maximum absolute accelerations at each hazard level (maximum of both floor and roof) and Table 4.5 has the corresponding statistical values. From the comparison between 10B and 10W, it appears that the wider wall of 10W results in higher acceleration demands at lower hazard levels (i.e., drift levels). This is expected as the higher resonant frequencies (i.e., lower period) of the wider wall coincides with higher spectral acceleration. However, at higher hazard level the opposite appears as the floor accelerations of 10B are larger than those of 10W. This could be caused by additional contributions from higher modes in the more intense ground motions when the effective period of the rocking walls is long. When the period of the uplifted system is long (i.e., 2.5 seconds or greater) the response spectra for the ground motions become almost flat. However, the higher mode periods are still affected by the spectral content in the shorter period range. A clearer trend is seen when comparing the 10B and 10W against their corresponding tapered walls. Notably, the softer (tapered) systems resulted in lower acceleration demands at all hazard levels. The consistent difference between the rectangular and tapered walls indicate that the acceleration demand is driven by not only the rocking (i.e., center of rotation), but also the moment of

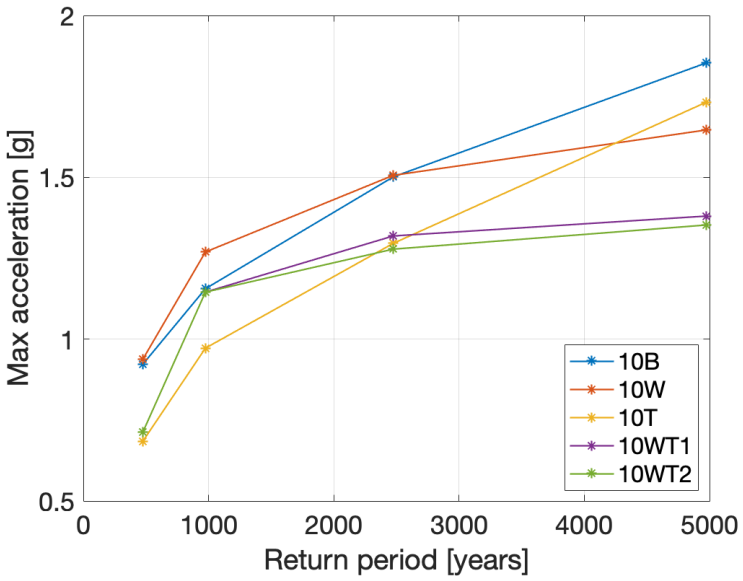

Figure 4.11: Ten-story max absolute acceleration.

inertia of the wall. Similar to roof drift, the accelerations of the narrower walls also seem to be more sensitive to increasing hazard levels.

4.5.4 Max wall/base shear and moments

Shear force and bending moment demands are generally not an issue at the base of the wall due to the base uplift and softening behavior of the rocking system. However, in taller walls such as the 10-story considered here the maximum flexural demand occurs near mid-height and can control the wall design. This subsection will look at the force demands on the wall and base to ensure the tapered walls do not reduce base damage at the risk of shear or flexural damage elsewhere in the walls. Note that there is a difference between the base moment (i.e., bending moment on the foundation), and base damage (damage to the bottom of the wall).

As expected, the maximum shear force on the wall was observed to be located at the base, see Fig. 4.12 (left) for an example of the maximum shear force distribution along the

Table 4.5: Statistical values of acceleration demands (g).

Return Period (years)	Stat. Values	10B	10W	10T	10WT1	10WT2
475	Min	0.60	0.61	0.56	0.41	0.41
	Lower Quartile	0.68	0.72	0.64	0.61	0.61
	Upper Quartile	1.00	1.15	0.70	1.11	1.11
	Max	1.38	1.54	0.82	1.68	1.68
	No. of Outliers	1	1	3	1	1
975	Min	0.94	0.68	0.75	0.55	0.55
	Lower Quartile	0.98	0.90	0.91	1.07	1.04
	Upper Quartile	1.29	1.75	1.23	1.36	1.30
	Max	1.87	3.13	1.58	1.93	1.70
	No. of Outliers	1	0	1	1	2
2475	Min	1.02	0.96	0.92	0.78	0.80
	Lower Quartile	1.24	1.25	1.17	1.17	1.21
	Upper Quartile	1.69	2.19	1.38	1.63	1.63
	Max	1.78	2.50	1.59	2.03	2.10
	No. of Outliers	0	0	0	1	1
4975	Min	1.16	1.28	1.11	0.87	0.88
	Lower Quartile	1.54	1.48	1.25	1.12	1.13
	Upper Quartile	2.26	2.10	1.95	1.93	1.95
	Max	2.55	2.65	2.27	2.10	2.17
	No. of Outliers	0	0	0	0	0

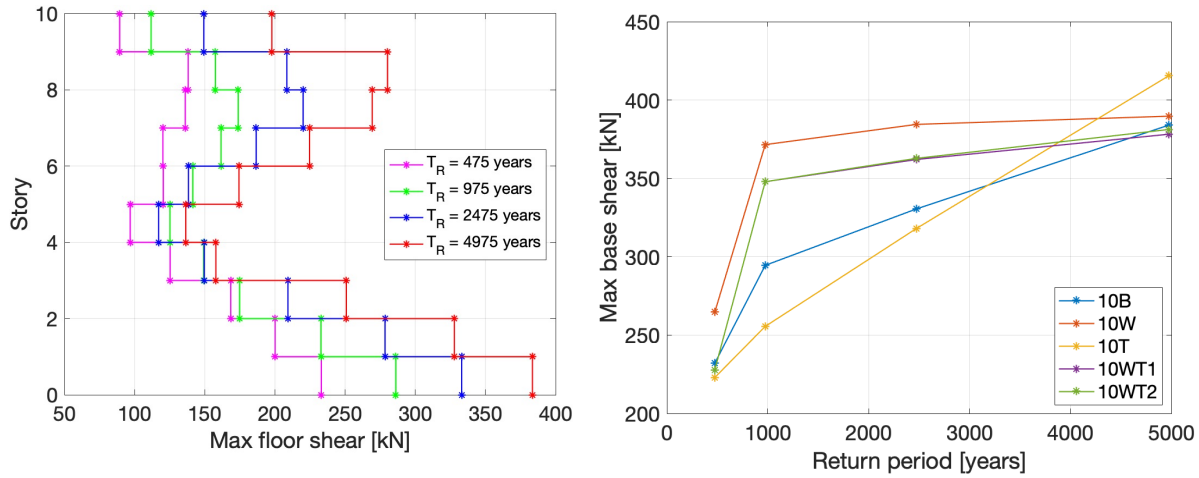

Figure 4.12: Ten-story max shear; wall (left), base (right).

height of a wall. In this plot, only the 10W as it as the pattern (though not the magnitudes) is representative of all of the walls. Figure 4.12 (right) shows the maximum base shear for all of the walls. Generally speaking, the stiffer system results in the highest demands as expected. The two narrower walls, again, showed higher rate of increase in base shear with respect to return period. This could be due to higher mode effect where the higher modes for the initially more flexible walls (i.e., the two narrower walls) may be in a range of larger spectral demands. Note that the tapered walls led to less shear demands than their rectangular counterpart, except 10T at a return period of 4975 years.

Figure 4.13 (top) is a plot of the (10B) internal moment distribution, at the height of each floor, showing the maximum moment does not occur at the bottom of the wall. The non-smooth moment distribution is due to the UFPs applying a moment to the wall from the eccentric vertical shear force. In addition, the maximum bending moment demands on the foundation (i.e., base moment) and the wall are shown in Fig. 4.13 (bottom). The base moment is the sum of the wall moment and the axial force couple from the boundary columns. Due to the internal moment distribution and the inclusion of boundary columns, the base moment is not necessarily greater than the internal moment, see Fig. 4.13 (bottom).

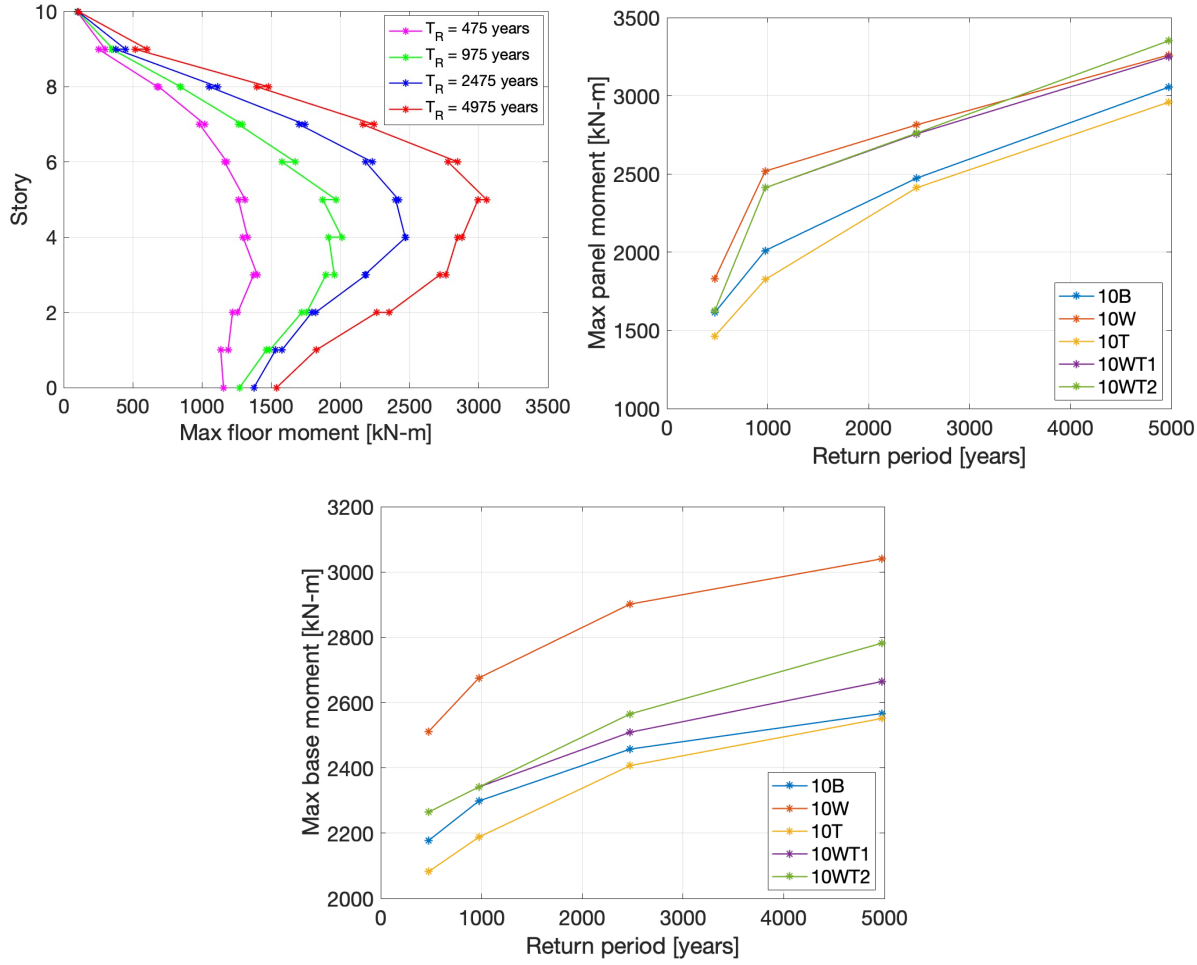

Figure 4.13: Ten-story max moment; story distribution (top left), wall (top right), base (bottom).

Interestingly, the maximum internal moment increases faster than base moment with respect to hazard level. This could be caused by an increase in higher mode contribution. Moreover, contrary to what was observed with drift, acceleration, and shear force, the moment on the narrower walls do not appear to be more sensitive to the increase in ground shaking with hazard level than the wider walls. With regards to moment, the tapered walls continued to show a decrease in demand compared to the corresponding rectangle walls. For completeness, the statistical values for the base shear and base moment results are provided in Table 4.6.

Table 4.6: Statistical values of base reactions.

Return Period (years)	Stat. Values	10B	10W	10T	10WT1	10WT2
Base shear [kN]						
475	Min	160	196	169	156	156
	Lower Quartile	187	209	205	182	182
	Upper Quartile	271	325	245	338	338
	Max	289	418	254	378	378
	No. of Outliers	0	0	1	0	0
975	Min	173	187	173	196	196
	Lower Quartile	254	236	245	267	267
	Upper Quartile	338	387	325	396	396
	Max	360	636	338	587	587
	No. of Outliers	0	0	0	0	0
2475	Min	249	271	245	227	231
	Lower Quartile	280	325	267	294	294
	Upper Quartile	391	467	369	480	494

	Max	445	601	414	556	556
	No. of Outliers	0	0	0	0	0
4975	Min	285	302	271	276	276
	Lower Quartile	334	338	351	298	302
	Upper Quartile	520	458	480	503	489
	Max	565	601	538	538	556
	No. of Outliers	160	196	169	156	156
Base moment [kN-m]						
475	Min	1994	2436	1833	2199	2199
	Lower Quartile	2061	2462	1984	2218	2218
	Upper Quartile	2275	2545	2126	2285	2285
	Max	2323	2609	2191	2301	2316
	No. of Outliers	0	0	0	1	1
975	Min	2199	2580	2114	2237	2237
	Lower Quartile	2233	2629	2156	2289	2289
	Upper Quartile	2352	2708	2245	2400	2351
	Max	2408	2754	2299	2466	2465
	No. of Outliers	0	0	0	0	1
2475	Min	2420	2698	2256	2401	2401
	Lower Quartile	2447	2797	2373	2449	2489
	Upper Quartile	2472	2933	2445	2549	2636
	Max	2512	2958	2466	2592	2703
	No. of Outliers	2	0	0	0	0
4975	Min	2417	2920	2423	2580	2687
	Lower Quartile	2531	2983	2458	2617	2729
	Upper Quartile	2690	3061	2735	2685	2808
	Max	2846	3137	2790	2774	2969

	No. of Outliers	0	0	0	1	1

4.5.5 Base damage

After ensuring the drift, acceleration, and shear/moment demands from the tapered modifications did not exceed critical levels (and actually demonstrated a reduction in some cases), the final performance consideration is the effects of the tapered modification on base damage.

Figure 4.14 is a plot of the maximum base strain, computed from the springs at the wall base, under different hazard levels; see Table 4.7 for the statistical values. The horizontal dashed line is the yield strain. It is again clear that the demand at the base of wall 10T, i.e., the narrowest base, increases faster with increasing hazard level than it does for the other walls. However, the 10T wall has lower strains than all other walls up to the 2475 year hazard. Indeed, the reduction in maximum strain seen with tapering the wall to 10T from the base case, 10B, is significant at all hazard levels and is able to reduce the strains below yield for the 2475 year hazard level.

It is also observed that all the tapered configurations considerably reduced the maximum base strain on the base of the wall. 10WT2 was able to mitigate the base from yielding even at the extreme hazard of 4975 years return period ground motions. Additionally, 10WT2 had consistently lower strain than 10WT1, which was likely due to more optimal selection of the dimension h'. In effect, h' determines how much damage the interior and exterior corner share – this can be seen by comparing the base yield drift/rotation capacity of 10WT1 and 10WT2 in Table 4.3. A large h' would offset the damage to the interior corner and vice-versa for exterior corner, therefore a balance would result in optimal performance. Again, optimization for b' and h' is outside the scope of this study but the considerations for achieving an optimal design are clear.

It is shown that the tapered systems indeed reduced the base strain (and thus the damage seen), even though the base case of a rectangular wall did not result in significant base

Table 4.7: Statistical values of base strain demand [e^{-3} m/m].

Return Period (years)	Stat. Values	10B	10W	10T	10WT1	10WT2
475	Min	1.625	1.451	1.339	1.339	1.339
	Lower Quartile	1.811	1.687	1.389	1.600	1.600
	Upper Quartile	2.629	2.207	1.600	1.773	1.773
	Max	2.790	2.728	1.947	2.195	2.195
	No. of Outliers	0	0	1	2	2
975	Min	2.009	1.711	1.364	1.811	1.811
	Lower Quartile	2.034	2.009	1.451	1.959	1.959
	Upper Quartile	2.765	2.331	1.662	2.021	2.009
	Max	3.051	2.765	1.972	2.232	2.158
	No. of Outliers	0	0	1	3	3
2475	Min	2.629	2.245	1.773	2.083	2.034
	Lower Quartile	2.679	2.592	1.910	2.307	2.121
	Upper Quartile	3.038	2.865	2.294	2.480	2.207
	Max	3.100	2.927	2.530	2.493	2.257
	No. of Outliers	0	0	0	1	0
4975	Min	2.790	2.803	2.183	2.356	2.096
	Lower Quartile	2.964	2.951	2.542	2.468	2.170
	Upper Quartile	4.092	3.423	3.286	3.026	2.319
	Max	4.353	3.757	4.179	3.249	2.356
	No. of Outliers	1	0	0	0	2

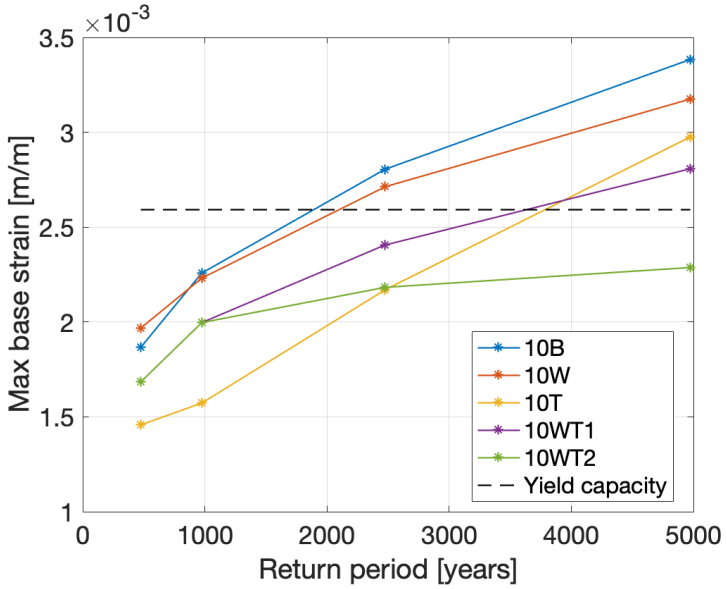

Figure 4.14: Ten-story max base damage.

damage; i.e., the base springs indicated yielding but did not splitting or crushing. The lack of damage was expected from the global behavior (specifically the drift demands). As shown below, the two-story rocking wall was designed closer to the performance limits for base damage and the impact of tapering on reducing base damage will be more evident.

As discussed previously, none of the tapered (or rectangle) systems reached drift demands that above acceptable targets, as was intended in their design. There are two factors that helps limit drift demands even though a rocking system is flexible: (1) from the amplitude-frequency curves in Fig. 4.8, the shortest period is approximately 1.4 second (4.5 rad/s) which corresponds to smaller spectral acceleration in the ground motion response spectra, see Fig. 4.9; (2) also from the amplitude-frequency curves, as the system reaches larger amplitudes, the resonance frequencies decrease (i.e., the resonance periods increase) which again corresponds to lower spectral accelerations. The latter is an inherent characteristic of rocking walls. The former can be further explored by investigating a shorter wall.

The following section discusses the two-story wall, geometric modifications, static and

dynamic characteristics, and dynamic response.

4.6 Tapered two-story wall

The layout of this section is the same as the previous sections; firstly, the static and dynamic characterization of the rocking walls will be discussed, followed by the dynamic response under ground motion. As base damage is the focus of this section, the other response parameters (e.g., base shear) are discussed more briefly than in previous sections.

4.6.1 Case study set up

The design of the rectangular wall is from the two-story shake table test conducted in the University of California, San Diego, by the NHERI Tall Wood project [Pei et al., 2019]. The two and ten-story wall systems are very similar except the former uses coupled panels instead of a single panel and boundary columns. The panels are coupled lightly via the UFPs fixed between the panels. More details on the two-story wall and the shake table test are given in [Pei et al., 2019]. Moreover, Wichman et al. developed finite element models (sharing the same modeling methodology in this study) that were compared against the test results and came out to be in good agreement [Wichman et al., 2022].

The two-story rectangular wall is denoted herein as 2B. Again, this section will focus on the reduction in base damage by tapering the base. Thus, two tapered walls were explored, 2T1 and 2T2, with no additional width in order to simplify the case study. 2T1 was designed with the same approach as 10T (i.e., based on the pushover results), however 2T2 did not use the pushover behavior for the basis of the design. Instead, 2T2 used the same b' as 2T1 but varied the h' such that it minimized the base damage demand from the ground motions at the extreme hazard level. 2T1 and 2T2 used a b' of 13.41 cm and a h' of 0.14 and 0.51 cm, respectively. The h' parameter of 2T1 needed to be very small in order for the pushover to converge with 2B at the approximately 2.5 percent drift (as designed). Although this is impractical for fabrication, it allows for further investigation of the potential of tapering to limit base damage.

Due to the smaller set of ground motions (discussed later) and the quicker computational time for the two-story wall models relative to the ten-story systems, h' of 2T2 was able to be based on the nonlinear time-history results. The design and material parameters of the walls are given in Table 4.8.

A slight modification was needed in the finite element model to capture the lateral displacement constraints of the two panels. As mentioned before, the lateral displacement of the panels are constraint via the diaphragm, however, the finite element model uses a leaning column to model the P-Delta and seismic loads of the gravity frame. Due to the small rotation of the rigid diaphragm, caused by the relative vertical displacement of the wall uplift and the leaning column, the diaphragm is not suitable for constraining the lateral displacement of the panels together. As a result, the panels of the two-story wall were constrained using a stiff truss element connecting the nodes on the panels at the floor and roof. Note that using other constraining methods, e.g., constraining the degrees of freedom, would be inaccurate as the panels experiences different vertical forces from the UFPs, and thus, undergoes different vertical displacements. Using truss elements allows the forces and lateral displacements to be constrained without introducing non-physical effects. Furthermore, the UFPs provide a small amount of coupling and are placed in between the panels similar to the ten-story wall except without the boundary columns.

4.6.2 Static and dynamic characterization

The pushover was simulated with the same method as the ten-story case study except that the lateral loads were distributed evenly between the coupled panels. Figure 4.15 shows a plot of the pushover in terms of base moment of both panels and roof drift. 2T1 is initially softer relative to 2B and converges at approximately 2.5 percent drift (designed as such). Notably, both 2B and 2T1 fail with 2B degrading quicker due to the base damage. The strength degradation is caused by the base crushing, which can be seen by comparing the crushing capacities in Table 4.9 with the onset of strength degradation in Fig. 4.15. Degradation was not observed with the ten-story case study as a taller wall would see more lateral deformation

Table 4.8: Two-story walls; design and material properties (units in kN and m).

	Parameter	Value
Gravity Frame	Height of 1st story	3.66
	Height of 2nd story	3.05
	Weight of 2nd floor	204.2
	Weight of roof	210.4
Panel	Height	7.32
	Width	1.52
	Thickness	0.175
	Weight	9.430
	Modulus of elasticity	7039550
	Shear modulus	459674
	Yield strain	0.0026
	Splitting strain	0.0082
	Crushing strain	0.0379
	Yield stress	18202
	Splitting stress	18202
	Crushing stress	2730
PT	Area of PT (per side)	4.32E-04
	Modulus of elasticity	200e6
	Eccentricity	0.127
	Yield stress	634318
	Initial PT force	106.8
	Hardening ratio	0.05
UFP	Diameter	0.0921
	Thickness	0.0095
	Width	0.1143
	Yield stress	344738
	Modulus elasticity	200e6
2T1	b'	0.1341
	h'	0.00135
2T2	b'	0.1341
	h'	0.00508

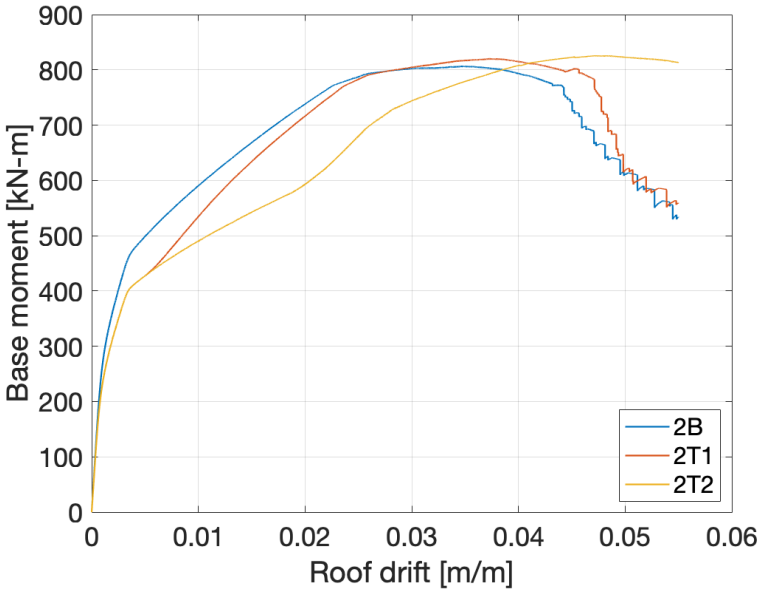

Figure 4.15: Two-story pushover response.

and less base uplift (i.e., rigid-body rotation). 2T2 was able to reach a roof drift of 5.5 percent, the end of the pushover, without deterioration in capacity. The pushover curves for the 2-story designs shows clearly the benefits of tapering the wall base in increasing the lateral drift at which CLT crushing and corresponding strength deterioration occurs. Furthermore, the capacities of the walls in Table 4.9 similarly shows h' helps distribute the base damage between the interior and exterior corners.

The amplitude-frequency plot, see Fig. 4.16, illustrates a similar behavior as the static pushover curve; 2T1 matches 2T2 at lower amplitudes and converges with 2B at higher amplitudes.

4.6.3 Dynamic response under ground motion

This subsection will discuss the ground motions and nonlinear time-history results of the two-story walls. In depth discussion of the performance parameters (e.g., base shear) will be omitted for brevity and to focus on the base damage, however the results are tabulated

Table 4.9: Capacities of two-story walls.

	2B	2T1	2T2
Roof Drift [e-2 m/m]; Base Rotation [e-2 rad]			
Base Yield	0.43; 0.48	0.46 (0.81); 0.53 (0.96)	0.44 (1.73); 0.51 (2.13)
Base Split	1.34; 1.6	2.67 (1.74); 3.27 (2.1)	1.44 (2.51); 1.75 (3.1)
Base Crush	3.38; 4.2	3.79 (3.52); 4.72 (4.37)	WNO[1](WNO)
PT Yield	2.27; 2.08	2.36; 2.17	2.57; 2.41
Base Moment [kN-m]; Base Shear [kN]			
Base Yield	512; 89	445 (548); 80 (98)	439 (635); 76 (111)
Base Split	706; 125	816 (758); 142 (133)	578 (765); 102 (133)
Base Crush	770; 138	644 (792); 116 (138)	WNO (WNO)
PT Yield	771; 138	770; 138	694; 125

[1] WNO denotes Was Not Observed.

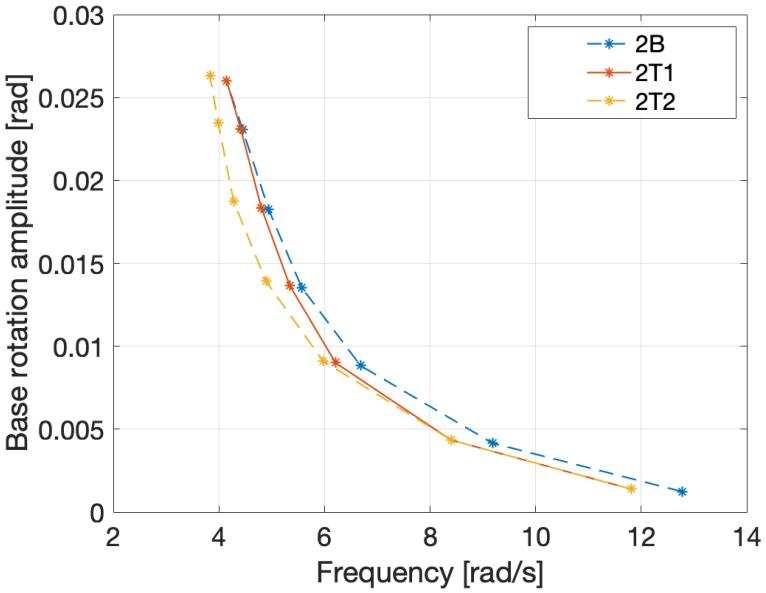

Figure 4.16: Two-story amplitude-frequency.

later and did not control.

Ground motion response spectra

The ground motions used in this subsection are directly from accelerometer data from the shake table tests. The tests used four ground motions scaled to three hazard levels: Service-Level Earthquake (SLE, 50% probability of exceedance in 50 years), Design-Basis Earthquake (DBE, 10% probability of exceedance in 50 years), and Maximum Considered Earthquake (MCE, 2% probability of exceedance in 50 years) that were used in the design of the test specimen. In addition, one ground motion was further scaled to 1.2 times MCE. Pertinent data for each ground motion are provided in Appendix D. Again, details on the selection and scaling of the ground motions can be found in [Pei et al., 2019; Wichman, 2018]. Figure 4.17 provides the ground motion response spectra (grey: ground motions, black: average of all ground motions). The smallest resonant period for the two-story wall is approximately 0.5 seconds (12 rad/s), see Fig. 4.16, which is within the region of large spectral acceleration.

Recall that the ten-story rectangular walls did not show significant base damage partially because the resonant periods were within the region of low spectral acceleration but also because the baseline wall was designed to be stronger relative to the design demands. Conversely, from the pushover, amplitude-frequency, and response spectra plots, the two-story case appears to be more suitable for tapering the base. The following will briefly discuss the drift, acceleration, and drift demands to ensure the base damage reductions obtained at the risk of other performance parameters.

Demands from nonlinear-time history response

The drift, acceleration, and force demands of the nonlinear-time history response (of each ground motion and hazard levels) are shown in Table 4.10. Generally, tapering the walls leads to a decrease in demands, including drift demands. Similar to the ten-story case study, the demands from the tapered walls did not exceed the rectangular walls by a significant amount.

The maximum strain at the two of the wall (from all ground-motions) and the strain capacity of the walls are shown in Fig. 4.18 with the solid line connecting the median values. As expected, 2B resulted in the most damage. Interestingly, 2T1 showed less base damage at all hazard levels except 1.2 times MCE. The difference in demand between 2T1 and 2B — in addition to the small h' — demonstrates (1) the significant performance benefits of distributing the damage to different sections of the wall, and (2) the sensitivity of rocking systems to the wall-foundation interface. The tapered walls were able to reduce base damage with 2T1 able to mitigate splitting at the three hazard levels.

4.7 Chapter conclusion

Rocking walls have been shown to be promising resilient lateral force resisting systems. The uplifting mechanism reduces the force demands on the wall, the PT bars increases M_{dec} and post-uplift stiffness, and the supplemental energy dissipation devices further dampens the system.

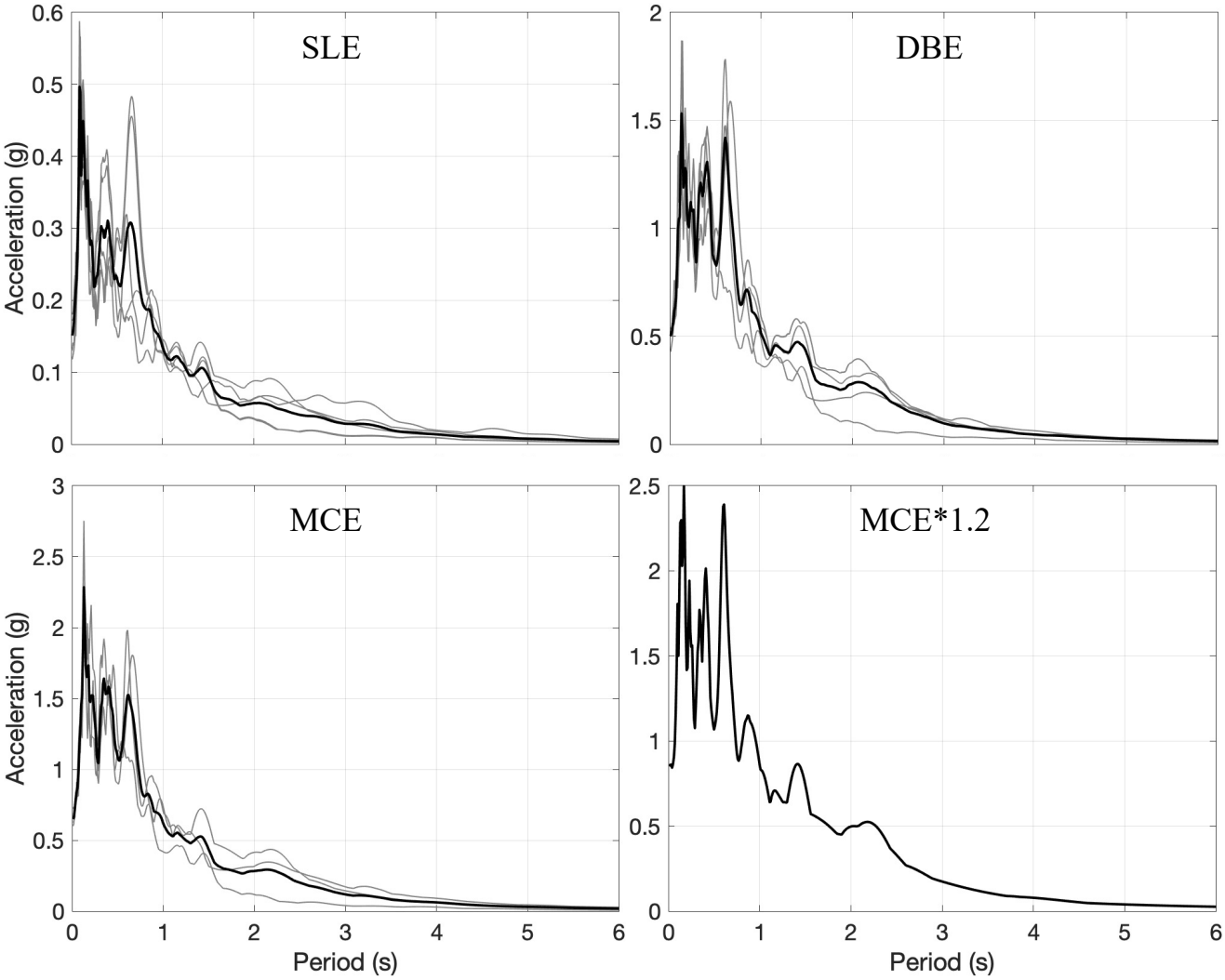

Figure 4.17: Response spectra of ground motion for two-story design (grey: ground motions, black: average of all ground motions)

Table 4.10: Two-story wall demands.

Demand	2B	2T1	2T2
Drift [m/m]; Acceleration [g]			
SLE	0.43; 0.54	0.64; 0.48	0.64; 0.48
	0.55; 0.56	0.53; 0.50	0.53; 0.50
	0.41; 0.51	0.49; 0.42	0.49; 0.41
	0.37; 0.51	0.31; 0.48	0.31; 0.48
	0.37; 0.54	0.37; 0.44	0.37; 0.44
DBE	2.02; 1.11	2.21; 1.25	1.79; 1.01
	2.16; 1.00	2.04; 0.94	2.25; 0.89
	2.16; 0.98	2.04; 0.90	2.25; 0.87
	1.46; 1.05	1.56; 1.07	1.46; 1.06
	1.15; 1.14	1.24; 0.92	1.25; 0.96
MCE	1.86; 1.32	1.69; 1.20	1.76; 1.18
	2.63; 1.29	2.65; 1.17	3.42; 1.22
	2.41; 1.14	1.97; 1.26	2.4; 1.18
MCE x 1.2	4.11; 2.35	4.14; 1.84	4.27; 2.58
Base Shear [kN]; Base Moment [kN-m]			
SLE	125; 473	107; 464	125; 456
	125; 503	107; 437	125; 437
	107; 469	89; 433	107; 433
	111; 438	89; 359	111; 359
	102; 454	89; 403	102; 403
DBE	182; 777	209; 776	182; 609
	182; 803	173; 763	182; 694
	187; 803	178; 763	187; 691
	178; 685	169; 672	178; 569
	165; 622	156; 594	165; 537
MCE	173; 757	169; 701	173; 607

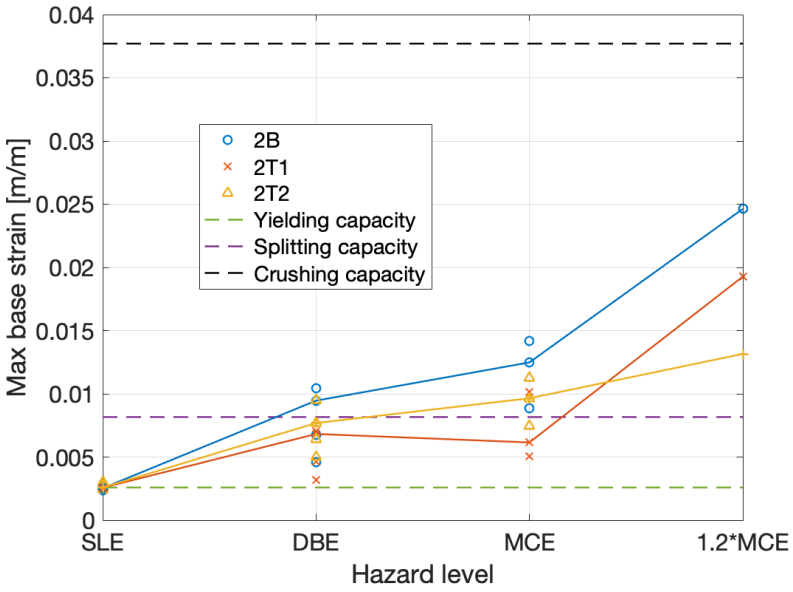

Figure 4.18: Two-story max base damage.

A few difficulties remain to be addressed; one notable issue, and the focus of this study, is base damage due to stress concentration from impact during rocking. This chapter introduced the concept of a tapered wall (a simplification of the curved-base rocking wall), and how to incorporate the modification into a finite element model.

Tapered walls leverage the base geometry to produce two stages of rocking (and two post-uplift lateral stiffnesses), in addition to distributing the base damage to two regions of the base. Optimizing the distribution of base damage can be done via h' which maximizes the drift capacity at base yield, splitting, and crushing. In addition, the isolated effects of the tapered base parameters (for an idealized rigid wall) on the static characteristics were explored.

Two case studies were looked at to evaluate the seismic performance of the tapered walls as compared with rectangular rocking walls. The ten-story case study used two design approaches: (1) equal width tapered walls with pushover response converging to the rectangular wall at a design drift level, and (2) widened tapered walls with increase stiffness after

a desired drift level. The latter approach resulted in the most reduction in base damage. The two-story case study focused on the base damage demands, and therefore only used the former design approach to simplify the case study with a more comparable design. Unless noted otherwise, the following findings pertain to both case studies.

The static and dynamic characteristics of the tapered walls were able to be tailored to behave as a narrower wall at low hazard levels (to limit force demands) and wider wall at higher levels (to limit drift demands). Furthermore, the non-rigid base smooths out the lateral resistance of stage 1 and 2. The amplitude-frequency relationship was shown to be highly nonlinear and matched the observations from the pushover, as expected. The amplitude-frequency also gave insight into the reason why, unlike the two-story walls, the ten-story walls did not experience much base damage under even the most extreme hazard levels. The following are the findings from the nonlinear time-history analyses:

- 10WT systems were able to limit drift levels similarly to 10B and 10W at low and extreme hazard levels, respectively.
- Drift, acceleration, force, and base damage demands of the narrower walls were more sensitive to increase in hazard level.
- Tapered walls resulted in lower acceleration demands at all hazard levels. Acceleration demand is sensitive to the wall (i.e., panel) stiffness.
- Maximum shear force on the wall is located at the base, conversely, maximum internal moment does not occur at the bottom of the wall.
- Maximum internal moment is more sensitive to increasing ground motions acceleration than base moment.
- Tapered walls can reduce base damage as well as other demands, e.g., base shear.
- Long period buildings are resilient to base damage due to: (1) low spectral acceleration at resonant frequencies; and (2) further decrease in resonance frequencies with increasing lateral displacement. Again, note that the ten-story baseline wall was designed to be stronger relative to the design demands.

- As such, tapered walls are more suitable for short period buildings.
- From the small h' and discrepancy between the rectangular and tapered walls, the rocking phenomenon is shown to be very sensitive to the wall-ground contact interaction.

For future work, the study can be revisited with the more generalized base modification (i.e., curved-base rocking walls). Additionally, an optimization/design methodology and equations can be formulated to facilitate the adoption of base modified PT rocking walls. Lastly, static pushover and shake-table tests are required for further validation of the base modification solution with regards to the finite element models and the performance benefits.

Chapter 5

CONCLUSIONS

Since the work of Housner on rocking and its seismic resilience/isolation properties, numerous studies have followed, which have: (i) provided further insight into the fundamental mechanics and behavior; (ii) advanced the concept of rocking systems as seismic isolators; and (iii) implemented Post-Tensioned (PT) rocking structures as Lateral Force-Resisting Systems (LFRSs) in seismically active regions. This dissertation hopes to do the same with the Nonlinear Normal Mode (NNM) framework to study the interaction of rocking and wall deformation and the novel concept of Base-Modified Rocking Walls (BMRWs).

Three objectives were set to pursue the this overarching goal, see Fig. 5.1: (1) understand the effects of the curved-base modification on the static and dynamic behavior of a PT rocking wall; (2) investigate the interaction of rocking and wall deformation, and (3) evaluate the seismic performance and damage reduction of Tapered-Base Rocking Walls (TBRWs).

5.1 Isolated effects of the curved-base modification on a PT rocking wall

The concept of a Curved-Base Rocking Wall (CBRW) was explored semi-analytically in Chapter 2. The equations of motion were formulated using the Lagrangian equation and solved numerically. The formulated equations provide a way to explore each driving factor/-parameter. It was shown that for CBRWs, a gyroscopic term capturing rotation-translation coupling is present in the equation of motion that is otherwise absent in rectangular walls. The effect of the gyroscopic term was found to be negligible for typical structures for drifts within 5 percent (see Appendix B).

The model showed that CBRWs are highly customizable, such that the pushover response can be tailored to better suit the different seismic hazard levels: softer for moderate seismic

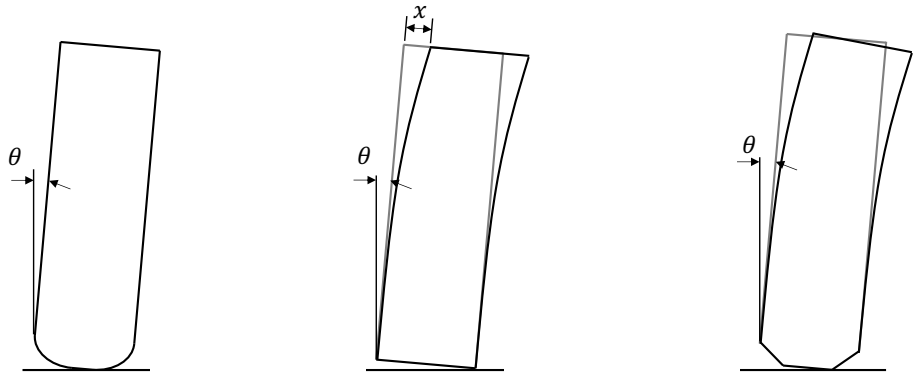

Figure 5.1: Curved-base rocking wall (left), rocking and wall deformation (middle), tapered-base rocking wall.

events to reduce internal shear and bending stress demand, and stiffer for extreme events to control drift. Furthermore, the static response showed that CBRWs can improve the drift at PT yield, which extends to drift at PT rupture.

The semi-analytical model served to validate the finite element model with curved bases that was later used in Chapter 4. In addition to modelling CBRWs, the analytical methodology introduced could be used to evaluate the strength/stiffness degradation in damaged rectangular rocking walls.

5.2 Interaction of rocking and wall deformation

A method to analytically study flexible rocking PT structures was presented in Chapter 3. The method used a two degrees-of-freedom model consisting of one degree-of-freedom for the base rotation angle, θ, and a second degree-of-freedom for the wall deformation, x. Note that this model was for a rectangular rocking wall. The kinematic relationships were provided and a Lagrangian approach specific to lumped masses [Wiebe and Harvey, 2019] was shown to streamline the derivation of kinetic energy term of the equations of motion. Furthermore, it was shown the initiation of rocking can be easily determined through the dynamic moment and force equilibrium condition. It is important to accurately predict rocking initiation to

better simulate the dynamic response as it was observed that rocking systems are extremely sensitive to initial conditions and system parameters [Aslam et al., 1980; Hogan, 1989; Plaut et al., 1996; Ageno and Sinopoli, 2005; Lenci and Rega, 2006].

Equations to calculate impact damping were given for the two-degree-of-freedom model (although the methodology extends to any number of degrees-of-freedom), which were derived using the conservation of angular momentum of the system and conservation of linear momentum of the top mass.

The semi-analytical model developed was validated against two benchmark cases. The pushover results showed the flexibility of the wall changes the stiffness of the system, as expected, but θ was far less sensitive — the gradient of the flexible wall pushover with respect to θ was very similar to the rigid wall. Overall, the results from the semi-analytical model showed good agreement with all benchmark cases.

The unforced dynamic response was characterized with NNMs; the resulting frequency-amplitude curve was confirmed to coincide with the peak demands from the forced response. In addition, the amplitude-frequency relationship of the flexible wall and equivalent rigid wall converges as amplitude increases. At large amplitudes θ drives the response, conversely, at small amplitudes x was the driving factor with the resonant frequency converging to the natural frequency of an equivalent fixed-base wall.

Interestingly, coexisting steady-state peak demands were observed and appeared to have fractal characteristics. Lastly, the phase angles were approximated by idealizing the response as a sine wave, and were shown to be able to predict resonance.

5.3 Base damage reduction and seismic performance of tapered-base walls

The concept of a TBRW, its seismic performance and reduction to damage were explored in Chapter 4. Similar to CBRWs, TBRWs can leverage the base geometry to tailor the pushover response with two post-uplift lateral stiffness. Moreover, it was observed that the tapered base reduces and distributes the damage between the interior and exterior corners. Optimizing the damage distribution can be done through the depth of the taper, h', which

maximizes the drift capacity at base yield, splitting, and crushing. In addition, observations showed the base elasticity smooths out the transition between rocking on the interior and exterior corners.

Two case studies (a two-story and a ten-story wall) were done to evaluate the seismic performance of the tapered walls against equivalent rectangular walls. It was shown that the static and dynamic characteristics of the tapered walls could be tailored to behave as a narrower wall at low hazard levels (to limit force demands) and wider wall at higher levels (to limit drift demands). The following are the pertinent findings from the nonlinear time-history analysis:

- Tapered walls resulted in lower acceleration demands at all hazard levels. Acceleration demand is sensitive to the wall (i.e., panel) stiffness.
- Maximum shear force on the wall is located at the base, conversely, maximum internal moment does not occur at the bottom of the wall.
- Maximum internal moment is more sensitive to increasing ground motions acceleration than base moment.
- Tapered walls can reduce base damage as well as other demands, e.g., base shear.
- From the ten-story amplitude-frequency curve, it was shown why long period buildings are inherently more resilient to base damage: (1) low spectral acceleration at resonant frequencies; and (2) further decrease in resonance frequencies with increasing lateral displacement.
- As such, tapered walls are more suitable for short period buildings.
- From the small h' and discrepancy between the rectangular and tapered walls, the rocking phenomenon is shown to be very sensitive to the wall-ground contact interaction.

5.4 Future work

The study in Chapter 4 can be revisited with the more generalized base modification (i.e., CBRWs). Additionally, an optimization/design methodology and equations can be formulated to facilitate the adoption of BMRWs. A comprehensive study on the stress concentration — perhaps using a finite element model with shell, or solid elements — of base-modified (and rectangular) rocking walls can be done to illustrate the stress reductions with more nuanced data. Lastly, pushover and shake-table tests can further explore the benefits and challenges of BMRWs and validate the finite element models.

Appendix A

EQUATION OF MOTION FOR RECTANGULAR WALL

Considering only a rectangular wall (without the gravity frame), the rigid body translation is removed from the kinetic energy and all that remains is rigid body rotation. The terms in Eq. (2.20) can be derived:

$$\dot{u} = \dot{u}_g + R\dot{\theta}\sin(\theta + \phi) \tag{A.1}$$

$$\dot{v} = R\dot{\theta}\cos(\theta + \phi) \tag{A.2}$$

The kinetic energy of the wall is then:

$$T = \frac{1}{2}m[R^2\dot{\theta}^2 + \dot{u}_g^2 + 2R\dot{u}_g\dot{\theta}\sin(\theta + \phi)] \tag{A.3}$$

By using Eq. (A.3) in Eq. (2.18), Eq. (2.20a) reduces to the commonly seen expression $I_{dyn} = mR^2$, G will be zero, and $M_g(t, \theta) = mR\sin(\theta + \phi)\dot{u}_g$.

Appendix B

GYROSCOPIC EFFECTS

The governing equation for Curved-Base Rocking Walls (CBRWs) contains a gyroscopic term which was seen in the comparison of the nonlinear time-history analyses to not be significant for the considered wall geometry and maximum rotations, see Chapter 2. It is important to know when this term can be neglected. Adopting the design of the seven CBRWs (CBRW 1 to CBRW 7), undamped free vibration simulations were performed using Eqs. (2.21) and (2.19) with varying initial conditions. The ratio of the inertial forces ($G\dot{\theta}^2/I\ddot{\theta}$) of the varying amplitudes were plotted (see Fig. B.1). For small θ (within the relevant range of 0.05 rad or approximately five percent drift), the dynamic force from the gyroscopic term is not significant, as expected from previous results. However, the curved base could be designed in order to increase the gyroscopic effects as seen in CBRW 1 to 5. Furthermore, if CBRWs are leveraged for other applications, e.g. tuned mass dampers, that are less constrained by drift levels, the gyroscopic effects may become more significant.

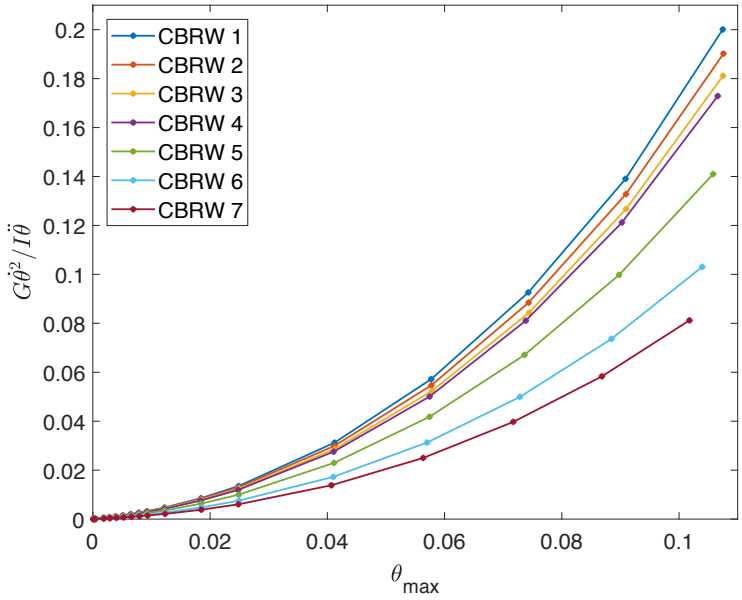

Figure B.1: Gyroscopic effects

Appendix C

NORMALIZATION OF EQUATIONS OF MOTION

The normalization/nondimensionalizion of the equations of motion from Chapter 3 are shown here. The normalized equations of motion may help generalize the equations to be used in future parametric studies with more ease. Because the generalized coordinates θ and x (tilt angle and lateral displacement, respectively) are not rectangular, several geometrically dependent scaling factors appear. The following are the terms in Eq. (3.10) shown in a condensed form:

$$\mathbf{M}^u + \mathbf{M}^v + \mathbf{M}^\theta = \begin{bmatrix} C_{M1} * m_1 + C_{M2} * m_2 & C_{M3} * m_2 \\ C_{M3} * m_2 & C_{M4} * m_2 \end{bmatrix} \tag{C.1}$$

$$\mathbf{G}_1^u + \mathbf{G}_1^v + \mathbf{G}_1^\theta = \begin{bmatrix} 0 & C_G * m_2 \\ C_G * m_2 & 0 \end{bmatrix} \tag{C.2}$$

$$\mathbf{G}_2^u + \mathbf{G}_2^v + \mathbf{G}_2^\theta = \begin{bmatrix} -C_G * m_2 & 0 \\ 0 & 0 \end{bmatrix} \tag{C.3}$$

$$\mathbf{F}_{\mathrm{g}}^u = \begin{Bmatrix} C_{F1} * m_1 + C_{F2} * m_2 \\ C_{F3} * m_2 \end{Bmatrix} \tag{C.4}$$

$$\nabla \Pi = \begin{Bmatrix} C_{V1} * m_1 + C_{V2} * m_2 \\ C_{V4} * m_2 \end{Bmatrix} + \begin{Bmatrix} C_{V3} * k_p \\ C_{V5} * k_p + C_{V6} * k_x \end{Bmatrix} \tag{C.5}$$

where the scaling factors (e.g., C_{M1}) are functions of θ, x, b, and h. The scaling factors are given in the following equations:

$$C_{M1} = \left(\frac{3}{4}\,h\,\sin\theta - \frac{b}{2}\,\cos\theta + x\,\cos\theta\right)^2 + \left(\frac{3}{4}\,h\,\cos\theta + \frac{1}{2}b\,\sin\theta - x\,\sin\theta\right)^2 \tag{C.6}$$

$$C_{M2} = \left(\frac{b}{2}\,\cos\theta - \frac{1}{4}\,h\,\sin\theta\right)^2 + \left(\frac{1}{4}\,h\,\cos\theta + \frac{1}{2}b\,\sin\theta\right)^2 \tag{C.7}$$

$$C_{M3} = \sin\theta\,\left(\frac{3}{4}\,h\,\sin\theta - \frac{1}{2}b\,\cos\theta + x\,\cos\theta\right) + \cos\theta\,\left(\frac{3}{4}\,h\,\cos\theta + \frac{1}{2}b\,\sin\theta - x\,\sin\theta\right) \tag{C.8}$$

$$C_{M4} = \cos^2\theta + \sin^2\theta \tag{C.9}$$

$$C_{G1} = \cos\theta\,\left(\frac{3}{4}\,h\,\sin\theta - \frac{1}{2}b\,\cos\theta + x\,\cos\theta\right) - \sin\theta\,\left(\frac{3}{4}\,h\,\cos\theta + \frac{1}{2}b\,\sin\theta - x\,\sin\theta\right) \tag{C.10}$$

$$C_{F1} = \frac{1}{4}h\cos\theta + \frac{1}{2}b\sin\theta \tag{C.11}$$

$$C_{F2} = \frac{3}{4}h\cos\theta + \frac{1}{2}b\sin\theta - x\sin\theta \tag{C.12}$$

$$C_{F3} = \cos\theta \tag{C.13}$$

$$C_{V1} = \frac{1}{2}bg\cos\theta - \frac{1}{4}hg\sin\theta \tag{C.14}$$

$$C_{V2} = \frac{1}{2}bg\cos\theta - \frac{3}{4}hg\sin\theta - xg\cos\theta \tag{C.15}$$

$$C_{V3} = \Delta\frac{\partial\Delta}{\partial\theta} \tag{C.16}$$

$$C_{V4} = g\sin\theta \tag{C.17}$$

$$C_{V5} = \Delta\frac{d\Delta}{dx} \tag{C.18}$$

$$C_{V6} = x \tag{C.19}$$

From Eqs. (C.1) to (C.5), the terms are conveniently normalized by dividing by m_2; m_1/m_2 is redefined as the mass ratio γ_m. Note m_n denotes the mass of the nth lumped mass. The vectors in Eq. (C.5) are the gravitational and strain potential energies. Dividing k_x (wall lateral stiffness) and k_p (PT element axial stiffness) by m_2, as mentioned above, results in

$\gamma_p = k_p/m_2$ and $\gamma_x = k_x/m_2$. Similar to the mass ratio, γ_p and γ_x are the stiffness-to-mass ratios for the axial and lateral springs, respectively, with units of inverse of time squared. Moreover, b (wall width) and x are normalized by h (wall height) — note this is achieved by dividing the top and bottom equations by h^2 and h, respectively — resulting in the aspect ratio $a = b/h$ and new generalized coordinate $d = x/h$.

Appendix D

GROUND MOTIONS USED IN TWO-STORY AND TEN-STORY WALL CASE STUDIES

Information on the ground motions used in the ten-story and two-story wall case studies are provided in Tables D.1 and D.2, respectively.

Table D.1: Ground motions for ten-story walls.

Return period (years)	GM ID	Name	Station	Date	Comp.	SF	Database
475	1612	Imperial Valley-06	Brawley Airport	1979	2	1.013	PEER NGA WEST2
	39321	Tottori. Japan	OKYH14	2000	1	4.968	PEER NGA WEST2
	42281	Niigata. Japan	NIGH11	2004	1	0.796	PEER NGA WEST2
	7942	Loma Prieta	SF - Diamond Heights	1989	2	2.114	PEER NGA WEST2
			AKT016	2011	NS	1.293	Kik-net

			CHB001	2011	EW	2.054	Kik-net
			HKD084	2003	NS	0.502	Kik-net
			IWTH07	2011	NS1	4.957	Kik-net
			TCGH12	2011	EW2	0.855	Kik-net
	20000811	Nisqually	2130	2001	1	2.847	PEER Subduction Earthquakes
	70064751	Pingtung. Doublet2	KAU005	2006	1	3.833	PEER Subduction Earthquakes
975	1612	Imperial Valley-06	Brawley Airport	1979	2	1.479	PEER NGA WEST2
	39322	Tottori. Japan	OKYH14	2000	2	3.501	PEER NGA WEST2
	42281	Niigata. Japan	NIGH11	2004	1	1.16	PEER NGA WEST2
	7942	Loma Prieta	SF - Diamond Heights	1989	2	3.08	PEER NGA WEST2
			AKT016	2011	NS	1.887	Kik-net
			FKSH05	2011	EW2	4.7	Kik-net
			GNM008	2011	NS	2.129	Kik-net
			GNM010	2011	NS	2.479	Kik-net
			HKD084	2003	NS	0.73	Kik-net

			TCGH12	2011	EW2	1.248	Kik-net
	20000811	Nisqually	2130	2001	1	4.151	PEER Subduction Earthquakes
2475	15211	Chi-Chi. Taiwan	TCU089	1999	1	1.669	PEER NGA WEST2
	1612	Imperial Valley-06	Brawley Airport	1979	2	2.239	PEER NGA WEST2
	42281	Niigata. Japan	NIGH11	2004	1	1.752	PEER NGA WEST2
	7942	Loma Prieta	SF - Diamond Heights	1989	2	4.654	PEER NGA WEST2
			AKT016	2011	NS	2.854	Kik-net
			CHB017	2011	NS	3.517	Kik-net
			FKSH03	2011	NS2	2.991	Kik-net
			GNM010	2011	NS	3.749	Kik-net
			TCGH12	2011	EW2	1.889	Kik-net
			TKY024	2011	NS	2.327	Kik-net
	70064921	Pingtung. Doublet2	KAU030	2006	1	2.675	PEER Subduction Earthquakes

4975	15211	Chi-Chi. Taiwan	TCU089	1999	1	2.196	PEER NGA WEST2
	1612	Imperial Valley-06	Brawley Airport	1979	2	2.949	PEER NGA WEST2
	32731	Chi-Chi. Taiwan-06	CHY034	1999	1	3.823	PEER NGA WEST2
	37481	Cape Mendocino	Ferndale Fire Station	1992	1	1.168	PEER NGA WEST2
			AKT016	2011	NS	3.751	Kik-net
			CHB009	2011	NS	4.683	Kik-net
			CHB017	2011	NS	4.63	Kik-net
			HKD068	2003	EW	2.821	Kik-net
			TCGH12	2011	EW2	2.485	Kik-net
			TKY024	2011	NS	3.064	Kik-net
	70064921	Pingtung. Doublet2	KAU030	2006	1	3.523	PEER Subduction Earthquakes

Table D.2: Ground motions for two-story walls.

Hazard level	Event Name	Station Name	RSN-Component	SF
SLE	Loma Pierta	Capitola	752-2	0.36
	Loma Pierta	Capitola	752-2	0.38
	Northridge	Canoga Park	959-2	0.25
	Superstition Hills	Poe Road	725-2	0.37
	Imperial Valley	Delta	160-1	0.42
DBE	Northridge	Canoga Park	959-2	0.99
	Northridge	Canoga Park	959-2	1.13
	Northridge	Canoga Park	959-2	1.13
	Loma Pierta	Capitola	752-2	1.16
	Superstition Hills	Poe Road	725-2	1.42
MCE	Loma Pierta	Capitola	752-2	1.32
	Northridge	Canoga Park	959-2	1.31
	Superstition Hills	Poe Road	725-2	2.06
MCE x 1.2	Northridge	Canoga Park	959-2	1.57

REFERENCES

318, A. C. (2014). *Building Code Requirements for Structural Concrete - ACI 318-14*. American Concrete Institute.

Acikgoz, S. and DeJong, M. J. (2013). "The rocking response of large flexible structures to earthquakes." *Bulletin of Earthquake Engineering*, 12(2), 875–908.

Acikgoz, S. and DeJong, M. J. (2016). "Analytical modelling of multi-mass flexible rocking structures." *Earthquake Engineering & Structural Dynamics*, 45(13), 2103–2122.

Acikgoz, S. and DeJong, M. J. (2017). "Vibration modes and equivalent models for flexible rocking structures." *Bulletin of Earthquake Engineering*, 15(10), 4427–4452.

Ageno, A. and Sinopoli, A. (2005). "Lyapunov's exponents for nonsmooth dynamics with impacts: Stability analysis of the rocking block." *Int J Bifurc and Chaos*, 15(06), 2015–2039.

Akbas, T., Sause, R., Ricles, J. M., Ganey, R., Berman, J., Loftus, S., Dolan, J. D., Pei, S., van de Lindt, J. W., and Blomgren, H.-E. (2017). "Analytical and experimental lateral-load response of self-centering posttensioned CLT walls." *Journal of Structural Engineering*, 143(6), 04017019.

Alexander, N., Oddbjornsson, O., Taylor, C., Osinga, H., and Kelly, D. (2011). "Exploring the dynamics of a class of post-tensioned, moment resisting frames." *Journal of Sound and Vibration*, 330(15), 3710–3728.

Aragaw, L. F. (2017). "Floor response spectra in hybrid base-rocking and reinforced concrete wall buildings." M.S. thesis, University of Washington,

Aslam, M., Scalise, D. T., and Godden, W. G. (1980). "Earthquake rocking response of rigid bodies." *J Struct Division*, 106(2), 377–392.

Avgenakis, E. and Psycharis, I. N. (2017). "Modeling of rocking elastic flexible bodies under static loading considering the nonlinear stress distribution at their base." *Journal of Structural Engineering*, 143(7), 04017051.

Avgenakis, E. and Psycharis, I. N. (2020). "Modeling of inelastic rocking bodies under cyclic loading." *Journal of Engineering Mechanics*, 146(4), 04020020.

Avramov, K. V. and Mikhlin, Y. V. (2013). "Review of Applications of Nonlinear Normal Modes for Vibrating Mechanical Systems." *Applied Mechanics Reviews*, 65(2) 020801.

Bachmann, J. A., Blöchlinger, P., Wellauer, M., Vassiliou, M. F., and Stojadinovic, B. (2016). "Experimental investigation of the seismic response of a column rocking and rolling on a concave base." *Proceedings of the VII European Congress on Computational Methods in Applied Sciences and Engineering (ECCOMAS Congress 2016)*, Institute Struct Analysis and Antiseismic Research, School of Civil Engineering, National Technical University of Athens (NTUA) Greece.

Bachmann, J. A., Strand, M., Vassiliou, M. F., Broccardo, M., and Stojadinović, B. (2017). "Is rocking motion predictable?." *Earthquake Engineering & Structural Dynamics*, 47(2), 535–552.

Bahmani, P., van de Lindt, J. W., Gershfeld, M., Mochizuki, G. L., Pryor, S. E., and Rammer, D. (2016). "Experimental seismic behavior of a full-scale four-story soft-story wood-frame building with retrofits. I: Building design, retrofit methodology, and numerical validation." *J Struct Eng*, 142(4), E4014003.

Baird, A., Smith, T., Palermo, A., and Pampanin, S. (2014). "Experimental and numerical study of U-shape flexural plate (UFP) dissipators." *2014 NZSEE Conference; 2014*.

Barbosa, A. R., Sinha, A., Higgins, C., and Soti, R. (2018). "Structural testing for the dr johnson's clt panels." *Report no.*, Oregon State University.

Caughey, T., Vakakis, A., and Sivo, J. (1990). "Analytical study of similar normal modes and their bifurcations in a class of strongly non-linear systems." *International Journal of Non-Linear Mechanics*, 25(5), 521–533.

Chen, Z., Popovski, M., and Iqbal, A. (2020). "Structural performance of post-tensioned CLT shear walls with energy dissipators." *Journal of Structural Engineering*, 146(4), 04020035.

Chopra, A. K. and Yim, S. C.-S. (1985). "Simplified earthquake analysis of structures with foundation uplift." *Journal of Structural Engineering*, 111(4), 906–930.

Christopoulos, C., Filiatrault, A., and Folz, B. (2002a). "Seismic response of self-centring hysteretic SDOF systems." *Earthq Eng & Struct Dyn*, 31(5), 1131–1150.

Christopoulos, C., Filiatrault, A., and Folz, B. (2002b). "Seismic response of self-centring hysteretic SDOF systems." *Earthq Eng & Struct Dyn*, 31(5), 1131–1150.

Christopoulos, C., Filiatrault, A., Uang, C.-M., and Folz, B. (2002c). "Posttensioned energy dissipating connections for moment-resisting steel frames." *J Struct Eng*, 128(9), 1111–1120.

Christopoulos, C., Filiatrault, A., Uang, C.-M., and Folz, B. (2002d). "Posttensioned energy dissipating connections for moment-resisting steel frames." *J Struct Eng*, 128(9), 1111–1120.

DeJong, M. J. and Dimitrakopoulos, E. G. (2014). "Dynamically equivalent rocking structures." *Earthq Eng & Struct Dyn*, 43(10), 1543–1563.

Dimitrakopoulos, E. G. and DeJong, M. J. (2012). "Overturning of retrofitted rocking structures under pulse-type excitations." *Journal of Engineering Mechanics*, 138(8), 963–972.

Dimitrakopoulos, E. G. and Giouvanidis, A. I. (2015). "Seismic response analysis of the planar rocking frame." *J Eng Mech*, 141(7), 04015003.

Eatherton, M. R., Ma, X., Krawinkler, H., Mar, D., Billington, S., Hajjar, J. F., and Deierlein, G. G. (2014a). "Design concepts for controlled rocking of self-centering steel-braced frames." *J Struct Eng*, 140(11), 04014082.

Eatherton, M. R., Ma, X., Krawinkler, H., Mar, D., Billington, S., Hajjar, J. F., and Deierlein, G. G. (2014b). "Design concepts for controlled rocking of self-centering steel-braced frames." *J Struct Eng*, 140(11), 04014082.

Ferner, H., Wemyss, M., Baird, A., Beer, A., and Hunter, D. (2014). "Seismic performance of non-structural elements within buildings." *2014 NZSEE Conference; 2014*.

Filiatrault, A., Uang, C.-M., Folz, B., Chrstopoulos, C., and Gatto, K. (2001). "Reconnaissance report of the february 28, 2001 nisqually (seattle-olympia) earthquake." *SSRP*, 2.

Flaccus, G. (2017). "Oregon city approves permit for us' 1st all-wood high-rise." *The Seattle Times*.

Ganey, R., Berman, J., Akbas, T., Loftus, S., Dolan, J. D., Sause, R., Ricles, J., Pei, S., van de Lindt, J., and Blomgren, H.-E. (2017). "Experimental investigation of self-centering cross-laminated timber walls." *Journal of Structural Engineering*, 143(10), 04017135.

Ganey, R. S. (2015). "Seismic design and testing of rocking CLT walls." M.S. thesis, University of Washington,

Greenwood, D. T. (1997). *Classical Dynamics*. DOVER PUBN INC.

Hasani, H., Ryan, K. L., Wichman, S., and Berman, J. (In press). "Dynamic behavior of mass timber building with cross-laminated timber rocking walls." *Earthquake Engineering and Structural Dynamic*.

Hassanli, R., ElGawady, M. A., and Mills, J. E. (2016). "Force–displacement behavior of unbonded post-tensioned concrete walls." *Engineering Structures*, 106, 495–505.

Henry, R. S., Brooke, N. J., Sritharan, S., and Ingham, J. M. (2012). "Defining concrete compressive strain in unbonded post-tensioned walls." *ACI Struct J 2012*.

Hill, T. L., Cammarano, A., Neild, S. A., and Barton, D. A. W. (2017). "Identifying the significance of nonlinear normal modes." *Proceedings of the Royal Society A: Mathematical, Physical and Engineering Sciences*, 473(2199), 20160789.

Hogan, S. J. (1989). "On the dynamics of rigid-block motion under harmonic forcing." *Proceedings of the Royal Society A: Mathematical, Physical and Eng Sciences*, 425(1869), 441–476.

Holden, T., Restrepo, J., and Mander, J. B. (2003). "Seismic performance of precast reinforced and prestressed concrete walls." *J Struct Eng*, 129(3), 286–296.

Housner, G. W. (1963). "The behavior of inverted pendulum structures during earthquakes. Bull Seismol Soc Am 1963;53:403–417.." *BSSA*.

Ishiyama, Y. (1982). "Motions of rigid bodies and criteria for overturning by earthquake excitations." *Earthq Eng & Struct Dyn*, 10(5), 635–650.

Kashani, M. M., Gonzalez-Buelga, A., Thayalan, R. P., Thomas, A. R., and Alexander, N. A. (2018). "Experimental investigation of a novel class of self-centring spinal rocking column." *Journal of Sound and Vibration*, 437, 308–324.

Kelly, J. M., Skinner, R. I., and Heine, A. J. (1972). "Mechanics of energy absorption in special devices for use in earthquake resistant structures." *Bulletin of the New Zealand Society for Earthquake Engineering; 1972*.

Kerschen, G., Peeters, M., Golinval, J., and Vakakis, A. (2009). "Nonlinear normal modes,

part i: A useful framework for the structural dynamicist." *Mechanical Systems and Signal Processing*, 23(1), 170–194.

Kibriya, L., Málaga-Chuquitaype, C., Kashani, M., and Alexander, N. (2018). "Nonlinear dynamics of self-centring rocking steel frames using finite element models." *Soil Dynamics and Earthquake Engineering*, 115, 826–837.

King, M. E. and Vakakis, A. F. (1994). "An energy-based formulation for computing nonlinear normal modes in undamped continuous systems." *Journal of Vibration and Acoustics*, 116(3), 332–340.

Koh, A.-S. and Hsiung, C.-M. (1991). "Base isolation benefits of 3-D rocking and uplift. I: Theory." *J Eng Mech*, 117(1), 1–18.

Koh, A.-S., Spanos, P. D., and Roesset, J. M. (1986). "Harmonic rocking of rigid block on flexible foundation." *J Eng Mech*, 112(11), 1165–1180.

Kramer, A., Barbosa, A. R., and Sinha, A. (2016). "Performance of steel energy dissipators connected to cross-laminated timber wall panels subjected to tension and cyclic loading." *J Struct Eng*, 142(4), E4015013.

Kurama, Y., Pessiki, S., Sause, R., and Lu, L. W. (1999). "Seismic behavior and design of unbonded post-tensioned precast concrete walls." *PCI J 1999*.

Kurama, Y. C. (2002). "Hybrid post-tensioned precast concrete walls for use in seismic regions." *PCI J*, 47(5), 36–59.

Laursen, P. T. and Ingham, J. M. (2004). "Structural testing of large-scale posttensioned concrete masonry walls." *J Struct Eng*, 130(10), 1497–1505.

Lenci, S. and Rega, G. (2006). "A dynamical systems approach to the overturning of rocking blocks." *Chaos, Solitons & Fractals*, 28(2), 527–542.

Li, S. and Yang, Y. (2021). "Data-driven identification of nonlinear normal modes via physics-integrated deep learning." *Nonlinear Dynamics*, 106(4), 3231–3246.

Li, T., Berman, J. W., and Wiebe, R. (2017). "Parametric study of seismic performance of structures with multiple rocking joints." *Eng Struct*, 146, 75–92.

Li, X., Kurama, Y. C., and Wu, G. (2020). "Experimental and numerical study of precast posttensioned walls with yielding-based and friction-based energy dissipation." *Engineering Structures*, 212, 110391.

Lin, C.-P., Wiebe, R., and Berman, J. W. (2019). "Analytical and numerical study of curved-base rocking walls." *Engineering Structures*, 197, 109397.

Lin, C.-P., Wiebe, R., and Berman, J. W. (Forthcoming 2022). "Nonlinear dynamic response of flexible post-tensioned rocking walls." *Engineering Mechanics*.

Lin, C.-P., Wiebe, R., and Berman, J. W. (Forthcoming 2023). "Nonlinear dynamic response of flexible post-tensioned rocking walls." *Journal of Strcutural Engineering*.

Lin, Y.-C., Sause, R., and Ricles, J. (2013). "Seismic performance of a large-scale steel self-centering moment-resisting frame: MCE hybrid simulations and quasi-static pushover tests." *J Struct Eng*, 139(7), 1227–1236.

Lu, L.-Y., Lee, T.-Y., Juang, S.-Y., and Yeh, S.-W. (2013). "Polynomial friction pendulum isolators (PFPIs) for building floor isolation: An experimental and theoretical study." *Eng Struct*, 56, 970–982.

Makris, N. and Zhang, J. (2001). "Rocking response of anchored blocks under pulse-type motions." *J Eng Mech*, 127(5), 484–493.

Manevich, L. and Mikhlin, I. (1972). "On periodic solutions close to rectilinear normal vibration modes." *Journal of Applied Mathematics and Mechanics*, 36(6), 988–994.

Manzo, N. R. and Vassiliou, M. F. (2020). "Simplified analysis of bilinear elastic systems exhibiting negative stiffness behavior." *Earthquake Engineering & Structural Dynamics*, 50(2), 580–600.

MATLAB (2017). *version 7.10.0 (R2010a)*. The MathWorks Inc., Natick, Massachusetts.

McKenna, F. (1997). "Object-oriented finite element programming: Frameworks for analysis, algorithms and parallel computing." Ph.D. thesis, University of California, Berkeley,

Mikhlin, Y. V. and Avramov, K. V. (2011). "Nonlinears Normal Modes for Vibrating Mechanical Systems. Review of Theoretical Developments." *Applied Mechanics Reviews*, 63(6) 060802.

Moroder, D., Pampanin, S., Palermo, A., Smith, T., Sarti, F., and Buchanan, A. (2017). "Diaphragm connections in structures with rocking timber walls." *Struct Eng Int*, 27(2), 165–174.

Moroder, D., Smith, T., Dunbar, A., Pampanin, S., and Buchanan, A. (2018). "Seismic testing of post-tensioned pres-lam core walls using cross laminated timber." *Engineering Structures*, 167, 639–654.

Palermo, A., Pampanin, S., and Buchanan, A. H. (2006). "Experimental investigations on LVL seismic resistant wall and frame subassemblies." *First European Conference on Earthquake Engineering and Seismology* (01).

Pampanin, S., Priestley, M. J. N., and Sritharan, S. (2001). "Analytical modelling of the seismic behaviour of precast concrete frames designed with ductile connections." *J Earthq Eng*, 5(3), 329–367.

Pei, S. (2022). "Development and validation of a resilience-based seismic design methodology for tall wood buildings." *In Proceedings of the 12th National Conference on Earthquake Engineering*, 12NCEE.

Pei, S., Huang, D., Berman, J., and Wichman, S. (2020). "Simplified dynamic model for post-tensioned cross-laminated timber rocking walls." *Earthquake Engineering & Structural Dynamics*, 50.

Pei, S., van de Lindt, J. W., Barbosa, A. R., Berman, J. W., McDonnell, E., Dolan, J. D., Blomgren, H.-E., Zimmerman, R. B., Huang, D., and Wichman, S. (2019). "Experimental seismic response of a resilient 2-story mass-timber building with post-tensioned rocking walls." *Journal of Structural Engineering*, 145(11), 04019120.

Perez, F. J., Pessiki, S., Sause, R., and Lu, L. W. (2003). "Lateral load tests of unbonded post-tensioned precast concrete walls." *ACI Special Publication 2003*.

Pierre, C., Jiang, D., and Shaw, S. (2006). "Nonlinear normal modes and their application in structural dynamics." *Mathematical Problems in Engineering*, 2006, 1–15.

Plaut, R., Fielder, W., and Virgin, L. (1996). "Fractal behavior of an asymmetric rigid block overturning due to harmonic motion of a tilted foundation." *Chaos, Solitons & Fractals*, 7(2), 177–196.

Priestley, M. J. N. (1991). "Overview of PRESSS research program." *PCI J 1991*.

Rand, R. H. (1971a). "A higher order approximation for non-linear normal modes in two degree of freedom systems." *International Journal of Non-Linear Mechanics*, 6(4), 545–547.

Rand, R. H. (1971b). "Nonlinear normal modes in two-degree-of-freedom systems." *Journal of Applied Mechanics*, 38(2), 561–561.

Rand, R. H. (1974). "A direct method for non-linear normal modes." *International Journal of Non-Linear Mechanics*, 9(5), 363–368.

Restrepo, J. I. and Rahman, A. (2007). "Seismic performance of self-centering structural walls incorporating energy dissipators." *J Struct Eng*, 133(11), 1560–1570.

Rosenberg, R. (1966). "On nonlinear vibrations of systems with many degrees of freedom." *Advances in Applied Mechanics*, Elsevier, 155–242.

Rosenberg, R. M. (1960). "Normal modes of nonlinear dual-mode systems." *Journal of Applied Mechanics*, 27(2), 263–268.

Rosenberg, R. M. (1962). "The normal modes of nonlinear n-degree-of-freedom systems." *Journal of Applied Mechanics*, 29(1), 7–14.

Rosenboom, O. A. and Kowalsky, M. J. (2004). "Reversed in-plane cyclic behavior of post-tensioned clay brick masonry walls." *J Struct Eng*, 130(5), 787–798.

Sarti, F., Palermo, A., and Pampanin, S. (2016). "Quasi-static cyclic testing of two-thirds scale unbonded posttensioned rocking dissipative timber walls." *J Struct Eng*, 142(4), E4015005.

Shaw, S. and Pierre, C. (1991). "Non-linear normal modes and invariant manifolds." *Journal of Sound and Vibration*, 150(1), 170–173.

Shaw, S. and Pierre, C. (1993). "Normal modes for non-linear vibratory systems." *Journal of Sound and Vibration*, 164(1), 85–124.

Shaw, S. and Pierre, C. (1994). "Normal modes of vibration for non-linear continuous systems." *Journal of Sound and Vibration*, 169(3), 319–347.

Sorrentino, L., Masiani, R., and D. Decanini, L. (2006). "Overturning of rocking rigid bodies under transient ground motions." *Struct Eng Mech*, 22.

Spanos, P. D. and Koh, A.-S. (1984). "Rocking of rigid blocks due to harmonic shaking." *J Eng Mech*, 110(11), 1627–1642.

Spanos, P. D. and Koh, A.-S. (1986). "Analysis of block random rocking." *Soil Dyn and Earthq Eng*, 5(3), 178–183.

Taniguchi, T. (2002). "Non-linear response analyses of rectangular rigid bodies subjected to horizontal and vertical ground motion." *Earthq Eng & Struct Dyn*, 31(8), 1481–1500.

Thiers-Moggia, R. and Málaga-Chuquitaype, C. (2020). "Seismic control of flexible rocking structures using inerters." *Earthquake Engineering & Structural Dynamics*, 49(14), 1519–1538.

Thonstad, T., Kennedy, B. J., Schaefer, J. A., Eberhard, M. O., and Stanton, J. F. (2017). "Cyclic tests of precast pretensioned rocking bridge-column subassemblies." *J Struct Eng*, 143(9), 04017094.

Todd, D., Carino, N., Chung, R., Lew, H., Taylor, A., and Walton, W. (1994). "1994 northridge earthquake: Performance of structures, lifelines and fire protection systems." . (1994-03-01).

Truniger, R., Vassiliou, M. F., and Stojadinović, B. (2015). "An analytical model of a deformable cantilever structure rocking on a rigid surface: experimental validation." *Earthquake Engineering & Structural Dynamics*, 44(15), 2795–2815.

Tso, W. K. and Wong, C. M. (1989a). "Steady state rocking response of rigid blocks part 1: Analysis." *Earthq Eng & Struct Dyn*, 18(1), 89–106.

Tso, W. K. and Wong, C. M. (1989b). "Steady state rocking response of rigid blocks part 1: Analysis." *Earthq Eng & Struct Dyn*, 18(1), 89–106.

Twigden, K. M., Henry, R. S., and Ma, Q. T. (2012). "Dynamic testing of post-tensioned rocking walls." *Proceedings of the 15th World Conference on Earthquake Struct*, Department of Civil and Environmental Engineering, University of Auckland, New Zealand.

Vakakis, A. (1992). "Non-similar normal oscillations in a strongly non-linear discrete system." *Journal of Sound and Vibration*, 158(2), 341–361.

Vakakis, A. (1997). "Non-linear normal modes (NNMs) and their applications in vibration theory: An overview." *Mechanical Systems and Signal Processing*, 11(1), 3–22.

van de Lindt, J. W., Bahmani, P., Mochizuki, G., Pryor, S. E., Gershfeld, M., Tian, J., Symans, M. D., and Rammer, D. (2016). "Experimental seismic behavior of a full-scale four-story soft-story wood-frame building with retrofits. II: Shake table test results." *J Struct Eng*, 142(4), E4014004.

Vassiliou, M. F., Mackie, K. R., and Stojadinović, B. (2014). "Dynamic response analysis of solitary flexible rocking bodies: modeling and behavior under pulse-like ground excitation." *Earthquake Engineering & Structural Dynamics*, 43(10), 1463–1481.

Vassiliou, M. F., Truniger, R., and Stojadinović, B. (2015). "An analytical model of a deformable cantilever structure rocking on a rigid surface: development and verification." *Earthquake Engineering & Structural Dynamics*, 44(15), 2775–2794.

Villaverde, R. (1997). "Seismic design of secondary structures: State of the art." *J Struct Eng*, 123(8), 1011–1019.

Welch, D. P. (2016). "Non-structural element considerations for contemporary performance-based earthquake engineering." Ph.D. thesis, University of Pavia,

Wichman, S. (2018). "Large-scale dynamic testing of rocking cross laminated timber walls." M.S. thesis, University of Washington, Seattle, WA,

Wichman, S. (2022). "Lateral design of a 10-story building specimen with mass timber rocking walls." *In Proceedings of the 12th National Conference on Earthquake Engineering*, 12NCEE.

Wichman, S., Berman, J. W., and Pei, S. (2022). "Experimental investigation and numerical modeling of rocking cross laminated timber walls on a flexible foundation." *Earthquake Engineering & Structural Dynamics*, 51(7), 1697–1717.

Wiebe, L. and Christopoulos, C. (2009). "Mitigation of higher mode effects in base-rocking systems by using multiple rocking sections." *J Earthq Eng*, 13(sup1), 83–108.

Wiebe, R. and Harvey, P. S., J. (2019). "On the Euler–Lagrange Equation for Planar Systems of Rigid Bodies or Lumped Masses." *Journal of Computational and Nonlinear Dynamics*, 14(9) 094502.

Wilson, A. W., Motter, C. J., Phillips, A. R., and Dolan, J. D. (2019). "Modeling techniques for post-tensioned cross-laminated timber rocking walls." *Engineering Structures*, 195, 299–308.

Wong, C. M. and Tso, W. K. (1989). "Steady state rocking response of rigid blocks part 2: Experiment." *Earthq Eng & Struct Dyn*, 18(1), 107–120.

Yim, C.-S., Chopra, A. K., and Penzien, J. (1980). "Rocking response of rigid blocks to earthquakes." *Earthq Eng & Struct Dyn*, 8(6), 565–587.

Zhang, J. and Makris, N. (2001). "Rocking response of free-standing blocks under cycloidal pulses." *J Eng Mech*, 127(5), 473–483.